



THESIS

2

2009

**LIBRARY**  
**Michigan State**  
**University**

This is to certify that the  
dissertation entitled

SCANNING-PROBE STUDY OF DOPANT CHARGING IN A  
SEMICONDUCTOR HETEROSTRUCTURE

presented by

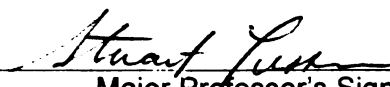
CEMIL KAYIS

has been accepted towards fulfillment  
of the requirements for the

Ph.D.

degree in

PHYSICS



Major Professor's Signature

12/5/2008

Date

**PLACE IN RETURN BOX** to remove this checkout from your record.  
**TO AVOID FINES** return on or before date due.  
**MAY BE RECALLED** with earlier due date if requested.

DATE DUE	DATE DUE	DATE DUE

SCANNING-PROBE STUDY OF DOPANT CHARGING  
IN A SEMICONDUCTOR HETEROSTRUCTURE

by

CEMIL KAYIS

A DISSERTATION

Submitted to  
Michigan State University  
in partial fulfillment of the requirements  
for the degree of

DOCTOR OF PHILOSOPHY

PHYSICS

2008

ABSTRACT  
SCANNING-PROBE STUDY OF DOPANT CHARGING  
IN A SEMICONDUCTOR HETEROSTRUCTURE  
BY  
CEMIL KAYIS

Although dopant properties are well understood with respect to the bulk, the study of configurations of dopants in small numbers is an emerging field[1, 2]. Moreover, shallow donors and acceptors are analogous to hydrogen atom. Experiments on small numbers of dopants have the potential to be a testing ground for fundamental questions of atomic and molecular physics[3, 4].

Here I present local capacitance measurements of electrons entering silicon donors in a gallium arsenide heterostructure, conducted at liquid helium temperatures. The precise position with respect to tip voltage of the observed single-electron peaks varies with the probe location, reflecting a random distribution of silicon within the donor plane. In addition, three broad capacitance peaks are observed independent of the probe location, indicating clusters of electrons entering the system at approximately the same voltages. These broad peaks are consistent with the addition energy spectrum of donor molecules, effectively formed by nearest-neighbor pairs of silicon donors.

We also introduce the local-probe measurements near a lithographically defined gate electrode and at an elevated temperature. Missing and reduced amplitude peaks are observed in the addition spectrum of donor molecules. The missing peaks arise from thermal activation of weakly bound states, enabling them to escape over the potential barrier. The reduction in the amplitude of the donor charging peaks is consistent with a field emission effect. To the best of our knowledge, this is the first scanning probe study of donor atom energy levels near a surface gate.

To my parents

## Acknowledgements

Throughout the time I spent at MSU, there have been many people who helped me in this adventure.

My thesis adviser, Stuart, is not only an excellent mentor but a very good scientist whose enthusiasm inspired me a lot. During several years of my graduate career, he has been a very supporting and encouraging teacher, and an optimistic and directing supervisor. His humbleness and taking everything from the bottom line made me feel comfortable even if we were dealing with complicated issues. I am very fortunate to have an opportunity to work with him.

I am very grateful Irma Kuljanishvili who is a former graduate student in our group for her great personality, insightful lab discussions, and as being my bench-top neighbor during most of my graduate study. I also can not forget to mention Subhashish Chakraborty's name even though we overlapped very little. I always appreciated his help on teaching me the basics of the microscope and clean room experience. I am also very thankful for my other lab partners Alexandra Tomic, Morewell Gasseller, Josh Veazey, and Chris Lawrence for making our lab as warm as home. I wish them all great success in their future careers. I should attribute my special thanks to our graduate secretary Debbie Barratt for being always there and clear about all administrative advices. Dr. Reza Loloee deserves gracious thanks for his precious help with sputtering equipment as well as his personality and friendship. I am also very thankful to Dr. Baokang Bi for his tutoring and supervision on using scanning electron microscope and instructions about e-beam lithography. Machine shop staff, particularly Tom Palazzolo also deserves a huge thanks for not saying no to my project orders and making the machine shop a friendly environment.

I would like to attribute my humble thanks to my professors, particularly Carlo Piermarocchi and Tom Kaplan for their theoretical contribution to our work, James Harrison, who is a professor of chemistry for his numerical calculations. I am also

grateful to Prof. Bill Pratt and Prof Chong-Yu Ruan for discussions on many topics during the advance lab teaching, which contributed to improve my perception in physics.

I would like to thank all of my friends for their valuable friendship and encouragement. Finally, I would like to thank my family and my parents, whose love and support I feel every day from overseas.

This work was supported by the Michigan State Institute for Quantum Sciences and the National Science Foundation, grant Nos DMR-0305461 and DMR-0075230. The W. M. Keck Microfabrication Facility provided valuable resources for fabrication and scanning electron microscopy.



# Table of Contents

Abstract . . . . .	ii
List of Tables . . . . .	viii
List of Figures . . . . .	ix
1 Introduction . . . . .	1
1.1 Motivation . . . . .	1
1.2 Thesis Overview . . . . .	2
1.3 Semiconductor Heterostructures . . . . .	3
1.4 Dopant Systems . . . . .	5
2 Sample . . . . .	10
2.1 Molecular Beam Epitaxy . . . . .	10
2.1.1 Effusion Cells . . . . .	15
2.2 Formation of Two-dimensional Electron System and $\delta$ -Doping . . . . .	16
2.2.1 2D Electron System Formation . . . . .	16
2.2.2 Delta ( $\delta$ ) Doping . . . . .	20
3 Experimental Setup and Technique . . . . .	25
3.1 Introduction . . . . .	25
3.2 Charge Accumulation Imaging . . . . .	26
3.3 Scanning Probe Microscope Design . . . . .	35
3.4 The Cryogenic Charge Circuit . . . . .	42
3.4.1 The Capacitance Bridge . . . . .	42
3.4.2 HEMTs and the Sensor Circuit . . . . .	46
3.4.3 Tip . . . . .	52
3.5 The Cryostat . . . . .	52
4 Donor Molecules and Experiment . . . . .	57
4.1 Introduction . . . . .	57
4.2 Spectroscopy of Donor Molecules . . . . .	58
4.3 Measurements . . . . .	60
4.3.1 Gated-Capacitance Measurement . . . . .	60
4.3.2 Scanning-probe Spectroscopy Measurements . . . . .	63
4.4 Donor Molecule Formation-Results of CI Method . . . . .	74
4.4.1 Introduction . . . . .	74
4.4.2 Analysis of Broad Peaks . . . . .	74
4.4.3 Effective Mass Approximation . . . . .	75
4.4.4 Configuration-Interaction Results . . . . .	82
4.4.5 Influence of non-nearest neighbors . . . . .	84
4.4.6 Comparing the calculation and measurement . . . . .	92

5	Donor Layer Spectroscopy of a Gated Sample . . . . .	96
5.1	Thermal and Field Emission Theory . . . . .	96
5.2	Measurement and Analysis of Donor Molecules at 77 K . . . . .	101
5.3	Measurement and Analysis of Field Emission of Donor Molecules . . . . .	105
6	Conclusions and Future Directions . . . . .	116
6.1	Summary . . . . .	116
6.2	Future Directions . . . . .	117
A	Configuration Interaction Theory . . . . .	121
A.1	Introduction . . . . .	121
A.2	Variation Method . . . . .	122
A.3	Strong Correlation (The Heitler-London Picture) . . . . .	126
A.4	Hartree-Fock Approximation . . . . .	128
A.4.1	Molecular Orbital Theory . . . . .	128
A.4.2	Self Consistent Field . . . . .	132
A.4.3	Hartree-Fock Theory . . . . .	133
A.4.4	The Energy Expression . . . . .	135
A.5	Configuration Interaction Calculations . . . . .	136
A.5.1	Basis Sets . . . . .	136
A.6	Donor molecule picture . . . . .	141
B	Gate Fabrication . . . . .	146
B.1	Sample cleaning . . . . .	146
B.2	Bilayer resist covering . . . . .	147
B.3	E-beam writing — JEOL JSM 840A Scanning Electron Microscope . . . . .	148
B.3.1	Key parameters . . . . .	148
B.3.2	Alignment and pattern writing . . . . .	149
B.4	Developing, TiAu deposition, and lift-off . . . . .	150
B.5	Four-pattern procedure . . . . .	151
	Bibliography . . . . .	153

Images in this dissertation are presented in color.

# List of Tables

5.1	Characteristic Ionization Temperatures for 2DM Bound States . . . .	102
-----	---	-----

# List of Figures

1.1	Schematic illustration of the zincblende lattice consisting of group-III and group-V elements. The lattice is doped with the donors (Si, Te) and acceptors (Be, C) which have an excess electron and deficit of electrons respectively[5]. . . . .	8
1.2	Schematic illustration of a hydrogen-like wave function of a donor. The effective bohr radius is much larger than the lattice constant of the crystal.[5]. . . . .	9
2.1	Mean free path for nitrogen molecules at 300K. . . . .	13
2.2	Simplified schematic diagram of an MBE apparatus showing Knudsen cells or effusion cells for different source materials with shutters. The sample sits on a heated holder, which is rotated during the growth of the sample. . . . .	14
2.3	The energy-level diagram of AlGaAs and GaAs without energy band bending. . . . .	18
2.4	The 2DES in GaAs. (a) Using molecular beam epitaxy, layers of semiconductors with different chemical composition can be grown on top of each other, a single crystalline layer at a time. This is used to create structure that has a GaAs layer below an AlGaAs layer. The AlGaAs layer has a larger band gap, leading to a step in the effective potential electrons see. (b) Electrons from dopants in the AlGaAs layer fall into the more energetically favorable undoped GaAs layer, where they form a 2DES at the interface [6]. . . . .	19
2.5	Schematic illustration of a semiconductor substrate and an epitaxial film containing $\delta$ -doped layer. it is also shown that the impurity atoms are confined in a single schematic atomic layer[7]. . . . .	23
2.6	Doping profile of a doping spike located at $z = z_d$ with 2D density of $N^{2D}$ , maximum concentration $N^{max}$ , and full-width at half-maximum of $\Delta z_d$ [7]. . . . .	24
3.1	Schematic of the CAI technique. CAI is a capacitive technique in which the tip and the quantum system residing below can be thought of as the two plates of a capacitor, with a voltage being applied to the system below that charges up the tip. . . . .	31

3.2	The circuit equivalent to the tip sample arrangement in the CAI technique. . . . .	32
3.3	The in-phase and the out-of-phase charging as a function of logarithmic frequency and tunneling resistance, as obtained from the model circuit. As the frequency is increased, the capacitor does not have time to charge and discharge during the cycle of the excitation. As we pass through $\omega = 1/RC_{total}$ , the in-phase signal rolls off while the lagging-phase signal exhibits a peak. . . . .	33
3.4	Schematic of the vertical tunneling geometry. (a) In the 3D-to-2D case we probe the charging of the 2DES. (b) In the 2D-to-donor layer case we probe the charging of the donor layer. In both cases an ac excitation is applied to the 3D metallic substrate which resides below the tunneling barrier. The charge tunneling into the 2DES or to the donor layer induces an image charge on the tip, which is measured by a cryogenic charge sensor circuit. . . . .	34
3.5	Schematic of the Besocke type scanning head. Three carrier piezo-tubes are supporting the sample holder ramps. The sample sits upside-down rigidly mounted on the sample support disk. The outside carrier tubes and the middle scanning tube are all attached to a bottom plate.	39
3.6	(a) Schematic of our scanning head. Both the tip and the sample are supported by identical piezoelectric tubes (dimensions: 7.6 cm-long x 4.8 mm-diam x 0.8 mm-wall thickness). As a result the unit is nearly perfectly thermally compensated. The displacer, outlined in dashes, screens the tip from the electric fields of the piezo-tubes. All the metal parts are made of brass, shown hatched. (b) Sketch of support leg showing the rotating foot assembly. (c) Bottom view of the microscope. The clamping screws fix the ramps to allow the positioning screw to be turned-the sample is attached to the other side of this screw. In this way, we can adjust the vertical position of the sample by as much as 1 cm. The diameter of the unit is 3.8 cm. . . . .	40
3.7	Photograph of the actual microscope. The shiny ruby balls at the end of each foot help reduce friction during fine approach of the sample. .	41
3.8	Schematic of a simple capacitance bridge. Balancing the bridge involves adjusting the amplitude and phase of $V_r$ so that the voltage $V$ at the center of the bridge is zero[6]. . . . .	45

3.9	A picture of our commercially available device, Fujitsu model FHX35X HEMT, made of GaAs/AlGaAs modulation doped heterostructure. Their low temperature compatibility is excellent with a very low input capacitance. . . . .	48
3.10	Schematic picture of the top-down cross section of a HEMT[8]. . . . .	49
3.11	Source-drain I-V characteristics, at different gate voltages $V_{GS}$ , of a typical HEMT. We are operating the circuit at the ohmic regime at which it is shown inside a rectangular box. . . . .	50
3.12	Schematic of the cryogenic charge sensor circuit. $V_{null}$ is applied to the standard capacitor and $V_{exc}$ is the applied a.c. excitation to the sample. The a.c. excitation applied to the standard capacitor, is of the same amplitude but $180^\circ$ degree out of phase with the excitation voltage that is applied to the sample. The charge sensitivity of the circuit is 0.01 electrons/ $\sqrt{Hz}$ . . . . .	51
3.13	SEM micrograph of a regular (top) and a crushed (bottom) Pt/Ir tip is shown. The radius of apex of the tip is approximately 50 nm. Tip must be cut very close to its apex to reduce the input capacitance of the circuit. . . . .	53
3.14	(Left) A simplified schematic diagram of the Oxford built top-loader cryostat is shown. The unconventional bungee-cord technique is used to provide the vibration isolation which is not shown in the figure. (Right) Top-loading probe depicted with a picture of our microscope attached from the bottom is depicted. The probe must be inserted slowly inside the cryostat and must be kept there during the experiment. It is surrounded by a superconducting magnet, which is shown in the figure. . . . .	56
4.1	The gated capacitance measurement taken by the TiAu planar gate on the surface of the sample with an area of $5.7 \times 10^{-7} \text{ m}^2$ . The capacitance increases with the ramping voltage forming the three plateaux. The gated measurement provides the background plateau for measurements with the localized probe. . . . .	62

- 4.2 A schematic diagram of the key layers in the gallium arsenide [001] heterostructure sample and the measurement technique. An excitation voltage can cause charge to resonate between the Si donor layer and a two-dimensional (2D) layer, which represents an ideal base electrode. This results in image charge appearing on a sharp conducting PtIr tip. A cryogenic transistor attached directly to the tip is used to measure the charging. The donor layer consists of silicon atoms confined to a plane with respect to the z direction, but randomly positioned with respect to the xy direction with an average density of  $1.25 \cdot 10^{16} \text{ m}^{-2}$ . At zero applied voltage, at least 90% of the Si atoms are ionized (that is, have donated an electron). Magnetocapacitance measurements conducted in the kilohertz frequency range indicate negligible donor-layer conductivity for identical samples cut from the same wafer. . . . . 67
- 4.3 A schematic diagram of the bottom-up layers in the gallium arsenide [001] heterostructure sample. The sample is fabricated by molecular beam epitaxy (MBE), which is an exceptional sample growing technique described in Chapter 2. The degenerately n-doped 3D substrate has the tunnel barrier grown upon it. The GaAs/AlGaAs heterojunction is shown on top of it, where the 2DEG forms. The delta-doped layer is shown with the plus signs, which represents the ionized Si donors. At the very top there is a GaAs cap layer. . . . . 68
- 4.4 A more detailed conduction-band diagram of the sample. The excitation voltage is applied to a degenerately doped substrate that acts as a metallic electrode. Above this is the 2D electron layer. It is separated from the metallic substrate by a superlattice tunneling barrier; the tunneling rate into the 2D layer is an order of magnitude greater than the 20 kHz excitation frequency we used. Hence for this experiment, the 2D layer can be regarded as being in ohmic contact with the substrate. . . . . 69
- 4.5 A schematic diagram of the area probed by the technique, with Si donors represented as hydrogen-like potentials. For our experimental geometry, the radius of the area over which we are probing is set mostly by the separation between the tip and the donor layer, which is approximately 60 nm [9][10]. Within this area, on average we expect 140 donors. A schematic diagram of the probe is also represented in the figure. . . . . 70

4.6	Capacitance measured with our local probe superposed with the gated measurement. The local measurement is the average of measurements acquired at three locations. Three broad peaks labeled A,B, and C were consistently observed. For both the local and gated curves, the voltage scales are plotted relative to the effective zero voltage, compensating for the contact potentials between the materials. The excitation voltage amplitude was $V_{exc}=15$ mV(rms) for both curves. The vertical scale of the probe measurement is exaggerated greatly relative to the gated measurement. . . . .	71
4.7	Capacitance variation DC versus tip voltage curve over the voltage range shown in the red circle in Figure 4.6. These data were acquired at a single location but with two different excitation voltage amplitudes: “coarse”, 15.0 mV rms and “fine”, 3.8 mV rms. The inset shows two $V_{exc} = 3.8$ mV measurements acquired under identical conditions but with a time delay of 9 hours. . . . .	72
4.8	(top) Three curves acquired at the voltage marked by the arrow in Figure 4.7 (same location) with an excitation voltage of 3.8 mV. The vertical scale has been converted to charge units and labeled as $\Delta q_{tip}$ to indicate that we have subtracted away the background charge. Below we plot the average of the three curves. The measurement is compared to a model curve that shows the semielliptical peak shape expected for single-electron tunneling [13,16]. The width of the model curve is set by the 3.8mV excitation amplitude; the asymmetry is caused by the lock-in amplifiers output filter, which is included in the model. (bottom) Comparison of the peak shapes for isolated peaks for both the coarse and fine excitation amplitudes. The average data of (top) is re-plotted (black) along with an especially well-isolated peak observed at a different location and with the coarse excitation voltage of 15.0mV (gray). The data are compared to two model curves that show the expected peak shapes for single-electron tunneling for the coarse and fine measurement parameters. . . . .	73
4.9	A representative picture of the hydrogen-like dopant atom is shown. Ground state wave function and the potential energy are shown. Energy level of the ground state is represented in Rydberg energy, $R^*$ . The effective Bohr radius, $a_0^*$ for the ionized donor in the crystal is also depicted in the figure [11]. . . . .	79
4.10	Simple representation of effective mass wave function or envelope function $F_C(\mathbf{r})$ and the impurity wave function $\psi_i(\mathbf{r})$ , where $a$ is the lattice constant. . . . .	80
4.11	Hydrogen-like energy spectrum of a shallow donor impurity. . . . .	81



4.12	A comparison between a rigorous calculation of the binding energy of the first electron (solid) and a simple Coulomb-shift approximation (dashed). The black curves correspond to two donors and the gray curves correspond to three. The solid gray curve is reproduced from Ref [12]. . . . .	86
4.13	Configuration-interaction calculation of the electronic energies of two donors separated by a distance $d$ , but otherwise isolated, as shown in the inset. At small separations, the model predicts two bound electrons for each donor molecule. . . . .	87
4.14	Statistical nearest-neighbor distances for donors in our system, calculated using the nominal growth density of donors in our sample. For comparison to theory, the distances are given with respect to the effective Bohr radius. . . . .	88
4.15	(Top)(Solid) calculated tip confinement potential in the donor layer [11,16]. (Dashed) image-charge approximation incorporated into the configuration-interaction calculations. A point charge of $1.7e$ was employed at a distance of $4a_0$ , as indicated in the inset. (Bottom) Revised configuration-interaction calculations including the rough approximation for the tip potential. This revised model predicts four bound electrons for each donor molecule—even for separations less than $a_0$ . . . . .	89
4.16	Configuration-interaction calculations of the 2DM addition energies for all bound electrons as a function of separation of the two ions $d$ . (Inset) The calculations include an image charge to approximate the potential applied by the tip. . . . .	90
4.17	Schematic representation of the full modeling procedure. We start from a random ensemble of donors and group them into nearest-neighbor pairs to form molecules $k$ . The addition energies shown on the left are used to assign the isolated addition energy of each molecule, $\epsilon_1^k, \epsilon_2^k$ , and so on. Last, the model includes the Coulomb energy shift from all non-nearest neighbors; we account for the fact that this shift will be different for successive electrons owing to changes in the screening charge of non-nearest-neighbor donors. . . . .	91

4.18	Comparison between representative measured data acquired at a single tip position (black) and representative modeled data (red); the modeled curves were calculated based on two different random configurations of donors, labeled config. (i) and config. (ii). To enable a direct comparison, we subtract the background capacitance from the measurements and plot the voltage in units of effective Rydbergs (scale factor $\alpha_{tip}/8.1 \times 10^{-3} V/Ry^*$ ). The effective voltage increment for both the measured and modeled curves is approximately $0.2 Ry^*$ . We see that the model predicts distinct broad peaks corresponding to the average electron addition spectra of the 2DMs; these peaks are reasonably qualitatively consistent with the observed peaks A, B and C. In contrast, the smaller fine-structure peaks, which correspond to individual charges entering the system, are different for different random configurations of the donors. . . . .	94
4.19	Comparison between the model and the measured data. The background capacitance (Figure 4.6 solid curve) has been subtracted from the local measurement (Figure 4.6 dots) to isolate the peaks. We display both the measured and modeled curves with the same horizontal scale of $Ry^*$ and vertical scale of electrons per $Ry^*$ . Although the match between experiment and theory is not exact, the overall agreement suggests that the donor-molecule model captures the correct physics. The gray curve addresses the discrepancy with regard to peak A, for which the predicted peak is significantly broader than the measurement; here we have reduced the broadening in the calculation by positioning the 2D layer 8 nm closer to the donor layer, which tends to sharpen the resonances. . . . .	95
5.1	(a) Schematic diagram of the thermal emission of electrons from a continuum. An electron in potential well must overcome the work function barrier $\phi = E_{vac} - E_F$ in order to reach the energy level of the vacuum and escape from the well. If an external field is applied, then $\phi$ is reduced by an amount of $\Delta\phi$ [13]. (b) A potential-energy diagram for a 1s electron of a H atom in a field of $2V/\text{\AA}$ . Broken lines show the Coulomb potential in the absence of an external field [14]. . . . .	100
5.2	Capacitance curve acquired at 77 K with a probe at a fixed position 1nm above the surface of the wafer. The encircled region shows the donor layer resonance, which is consistent with the previous measurements. . . . .	103

5.3	Capacitance curves for data acquired at 0.27 K and 77 K superposed with the gated capacitance curve (Ref. Figure 4.1) The third and fourth bound electrons, peak C, are missing for the data acquired at liquid N <sub>2</sub> temperature, which can be attributed to the thermal emission of electrons from 2DMs. The excitation voltage, $V_{exc}$ applied to the curve taken at 77 K is also larger than the $V_{exc}$ applied to the curve taken at 0.27 K, which are 16 mV and 3.8 mV. The excitation amplitude present at the donor layer is diminished by the lever arm factor $\alpha \cong 10$ . Hence, excitation voltage does not significantly contribute to the broadening of these unresolved peaks. . . . .	104
5.4	(a) A scanning electron microscope (SEM) micrograph of the gates fabricated on the surface of the wafer by electron beam lithography is shown. The separation between the line shapes is 12.5 $\mu\text{m}$ . The planar dimension of the mesh is approximately 1 mm x 1 mm.(b) Scanning-probe image of a circular gate in capacitance mode. This image is an average of 32 capacitance scans. (c) Enlarged SEM image of circular gate with a diameter of 0.5 $\mu\text{m}$ . (d) Scanning tunneling image of the gate is depicted with the labels showing the locations of the data acquired for localized probe measurement. A schematic diagram of tip is also shown. . . . .	110
5.5	The evolution of the capacitance curves acquired at different tip locations are shown . The deformation of 2DES plateau and suppression of the donor layer charging is observed due to the proximity of the probe to the gate electrode. . . . .	111
5.6	Localized-probe data acquired at 77 K corresponding to the locations in the presence (A1) and absence (A2) of a gate potential are shown in red and black, respectively. The black curve represents the data at the tip position where the gate potential does not influence the donor layer, which is the same data as the black curve in Figure 5.3. The blue curve is the gated capacitance measurement which is used as a background curve for the localized-probe measurements. The adjustments are done in order to superimpose the data on top of each other. The lever arm factor difference between tip-sample and gate-sample are adjusted to scale the capacitance acquired by both methods. The shifts with regard to probe voltage were also required to correct for perturbations of trapped charges. . . . .	112
5.7	Comparison of curves acquired at A1 and A2 with the background curve is subtracted from each. The clear suppression of resonance in the vicinity of the gate electrode is observed. This corresponds to a decrease of more than 50% in the amplitude of the enhanced capacitance peak due to charging into the donor layer. . . . .	113

5.8	(a) (b) The schematic potential landscape of the two-atom donor molecules (2DMs) in the absence and the presence of the electric field are shown. These are also representing the potential landscapes at the locations A2 and A1 shown in Figure 5.9. The four bound state energy levels are also represented with the orange lines, schematically. . . . .	114
5.9	A simplified schematic representation of the localized-probe measurement in the vicinity of the gate electrodes is shown. The delta-doped donor layer resides 60 nm below the surface and 2DES is formed 20 nm below the donor layer. The region labeled as A1 represents the probed area of the donor layer near gate in the $x$ - $y$ plane, whereas A2 shows the area away from the gate. The corresponding potential landscapes of the two-donor molecules (2DM) for A1 and A2 are also shown. The schematic diagram of fringing electric field ( $\mathbf{F}$ ) created in the GaAs sample by gate potential is depicted with green arrows. . . . .	115
6.1	CAI image with the tip voltage set at 0.05 V. The density of the bright high-capacitance features is consistent with the delta-doped B concentration in Si crystal. [Courtesy M. Gasseller]. . . . .	119
6.2	(a) Schematic of isolated donor molecule CAI measurement. The sample will be grown by the Simmons research group at the Atomic Fabrication Facility at the University of New South Wales [Perera]. (b) Conduction band profile. . . . .	120
A.1	Two 1s orbitals combine to form a bonding and an anti-bonding molecular orbitals. . . . .	130
A.2	An orbital correlation diagram for hydrogen. Notice that the orbitals of the separated atoms are written on either side of the diagram as horizontal lines at heights denoting their relative energies. The electrons in each atomic orbital are represented by arrows. In the middle of the diagram, the molecular orbitals of the molecule of interest are written. Dashed lines connect the parent atomic orbitals with the daughter molecular orbitals. . . . .	131
A.3	Plot of the STO against the distance of the electron from the nucleus [15]. . . . .	139
A.4	Comparison of the quality of the least-squares fit of a 1s Slater function obtained at the STO-1G, STO-2G, and STO-3G levels[16]. . . . .	140

A.5	(Left) The summarized ingredients of configuration interaction method. Calculations start with correct choice of basis functions and determining the relevant Hamiltonian for the system. Self consistent field (SCF) Hartree-Fock molecular orbitals must be generated to solve for the energy of the system for CI wave functions. (Right) The schematic diagram representing donor atoms constituting donor molecule and tip approximated as a point charge. . . . .	145
B.1	An image of the “4pattern” fabricated on the surface of the sample taken by an optical microscope. The overlap of the edges is seen in the figure. . . . .	152

# Chapter 1: Introduction

## 1.1 Motivation

Dopants are impurities deliberately added in low concentrations to a semiconductor to alter its electrical or optical properties. Semiconductor devices continue to shrink down to the nano-scale regime, and new applications have been proposed for which a single dopant atom acts as the functional part of the device. Moreover, experiments on small numbers of dopants have the potential to be a testing ground for fundamental questions of atomic and molecular physics. As conventional state-of-the-art transistors scale down to below the 50 nm level, understanding the role of individual dopants and the interactions with neighbors is becoming increasingly important [17, 18, 1].

With regard to the future technology, one of the ultimate challenges of nanoelectronics is the construction of devices that harness the electron wave function at the atomic level. The ultimate goal is to control the charge or spin states of individual dopants, which have been proposed as potential basis of a solid-state quantum computer [19, 20]. The ability to probe the quantum levels of single dopant atoms and dopant-dopant interactions at the atomic level will likely pave the way for the development of new experiments and theories of few-body quantum mechanical systems

Resonant-tunneling spectroscopy through isolated semiconductor donors has been observed in transport studies [21, 17]. In addition, ground breaking work by Geim and coworkers and Andresen and coworkers have probed resonances due to two closely spaced donors, effectively forming donor molecules [12, 2]. In this work, we focus on probing randomly distributed Si dopants forming donor molecules, which are confined approximately in a single monolayer gallium-arsenide semiconductor sample.

## 1.2 Thesis Overview

I present a capacitance-based scanning-probe method called charge accumulation imaging (CAI) to study the charging spectrum of single silicon donors and donor clusters in the same semiconductor heterostructure. Moreover, localized-probe experiments have been performed to explore the donor layer charging below and nearby a gate electrode. I also introduce the charging of sample measured from a top gate, where the top gate and sample can be considered as a parallel plate capacitor. To the best of our knowledge, this is the first scanning probe study of donor molecule energy levels in the vicinity of a surface gate potential.

The thesis overview will be as following: In the rest of this chapter I will briefly introduce the heterostructures from a general point of view. Dopant systems, which are created by deliberately added impurities into these crystal structures will be also explained. Chapter 2 discusses the details of how our  $\text{Al}_{0.3}\text{Ga}_{0.7}\text{As}/\text{GaAs}$  heterostructure sample is grown by molecular beam epitaxy (MBE) technique. In Chapters 4 and 5 the study of donor layer charging will be presented: First, the capacitance data acquired from the bare surface will be analyzed. Data showing addition spectrum of donor molecules will be compared to our model. Then, in Chapter 5, I will explain the capacitance data showing donor layer charging at 77 K in the presence of a potential gradient applied to the sample through the gate electrodes fabricated on top of the sample. Finally, Chapter 6 will summarize the experiment and conclude with possible future research directions.

The theoretical addition spectrum of the two-donor molecules is calculated numerically using configuration interaction method. Appendix A summarizes the basic theory of the method and the general picture of how the two-donor molecule calculations were done.

## 1.3 Semiconductor Heterostructures

The spatial dimensions of semiconductor device structures have been shrinking smaller and smaller, down to the atomic level. The reduction of the device dimension yields higher operation speeds as well as lower power consumption. Small device structures require that the spatial distribution of the dopants is well controlled. Redistribution processes such as diffusion, segregation, and drift in an electric field must be understood at near the atomic level. Delta-doping, which will be elaborated in the following chapters is one of the extremely narrow but well-defined doping profiles[7].

Semiconductor heterostructures are semiconductor crystalline materials that are made of layers with different compositions. The study of heterostructure type semiconductors started more than forty years ago. In the 1980s this area of research moved to the cutting edge of semiconductor physics, mostly due to progress in growth technologies, which are now capable of producing layers of different semiconductor materials as thin as a single atomic monolayer. The availability of structures with nearly ideal, well-controlled properties has made semiconductor heterostructures a testing ground of solid-state physics[22]. These structures include two-dimensional electron systems (2DES), quantum wires, and quantum dots. The investigation of the atomic and electronic properties of these systems are still the examples of ongoing research topics. Semiconductor heterostructures have also many practical applications: they provide a material source for a variety of novel devices such as double heterostructure (DHS) laser-based telecommunication systems, heterostructure light-emitting diodes, heterostructure bipolar transistors, and low-noise high electron mobility transistor (HEMT) for high frequency applications including, for example, satellite television.

Variations in compositions are used to control the motion of electrons and holes through the band engineering[23]. Semiconductor electronics had evolved from the possibility of controlling the conductivity of the semiconductor material by addition of impurities selectively. Heterostructures made it possible to solve a much more general



problem of controlling the fundamental parameters of a semiconductor crystal such as electronic and optical properties of the bulk crystal [24]. Modern growth technologies can make heterojunctions just one monolayer thick. In such abrupt heterojunctions, the parameters of the crystal such as chemical composition and band structure experience an abrupt change over a distance of the order of the lattice constant. A heterojunction is qualitatively different than p-n junction which is modulation doped region of the same material. An abrupt heterojunction mediates electronic states from two different materials with different positions and band extrema (i.e., potential energy), different effective masses, different g-factors, etc[22]. There are many interesting physical phenomena that are hidden in these abrupt differential regions that are key to many breakthroughs in last couple of decades. Although there are some other factors affecting electronic states in heterostructures such as external fields and impurities, the interesting properties of a heterojunction are determined by the abrupt potential change at the interface.

For convenience, we assume a few simple approximations throughout the thesis. First, we shall use the standard simplification that conduction electrons are free particles with an effective mass. It means that an electron at the interface of the heterostructure can be treated using an elementary problem of a particle in a potential well. Secondly, the random nature of alloys is usually neglected which allows treating them as crystals.

Many compounds of group III and group V (III-V) elements have been studied for their properties but only a few are commonly used in a heterostructure design. Since the active regions of heterostructure are usually at or very close to the interfaces, they must have nearly perfect interfaces; hence, interface properties are critical in forming a heterostructure. For example, it is essential for materials in adjacent layers to have a similar crystal structure and their lattice constants to be as close as possible. Moreover, surface roughness scattering will compromise the mobility of the electrons.

These conditions are met in gallium arsenide, GaAs, and aluminum gallium arsenide AlGaAs. The sample that was used in the studies described in this thesis belongs to this type of heterostructure.

AlGaAs has a wider band gap than the GaAs, and a slight doping of the AlGaAs layer produces an electric field, essential to bend the bands, forming a quantum well at the interface; the electrons that are given up by the dopant atoms form the two-dimensional electron system (2DES). Heterostructures should have nearly atomically sharp interface if they are to perform well. Additionally, the layers are usually very thin and require changing of composition rapidly during growth. Also, the interface must be contamination free. Hence, it is a challenge to grow such structures. The most common growth technique is molecular-beam epitaxy[23], with which it is possible to grow highly abrupt junctions between different materials. It also allows atomic-scale control over the thickness of each layer.

## 1.4 Dopant Systems

In this section I will discuss impurities and intentional dopant systems in semiconductors from a general point of view. It can be beneficial to get rid of the impurities from a semiconductor crystal. During the course of past several decades knowledge of the significant consequences of impurities motivated researchers to purify semiconductor materials, and subsequently to add intentionally foreign atoms, i.e. dopants, to tune the materials for high performance and low noise electronic devices. The term dopant was coined by Seidman and Marshall in 1963 to emphasize the deliberately added impurities.

Semiconductors have a completely filled valence band and an empty valence band in their intrinsic state. For silicon and gallium-arsenide, valence band states typically have the atomic states of p-orbital symmetry and conduction band states have the

atomic states of s-orbital symmetry. In the case of an impurity with an excess electron in the outermost shell (compared to the host), if the impurity is ionized inside a pure semiconductor crystal the empty continuum of the lowest state is the conduction band minimum where the excited electron of the impurity atom is donated; such kind of impurities are called “donors”. Likewise if we consider an impurity with a deficit of electron (hole state) in a pure semiconductor, the hole state of such an impurity can be filled from an occupied band, namely the valence band. Since such impurities can accept electrons from the occupied band, they are called “acceptors”.

The energy needed to ionize the donor or acceptor is called the activation energy. This energy is relatively weak due to the screening and reduced mass of the charge carriers. The consequence of this weak interaction between the impurity nucleus and the charge carrier is the following: First, the wave function of the bound state of the impurity is much larger than the lattice constant of the crystal, Figure 1.2. Second, the activation energy of such shallow impurities is smaller than the thermal energy at room temperature, which is approximately 25 meV, thus it is considered that all shallow impurities are activated at room temperature.

There are many experimental techniques developed to produce clean state-of-the-art samples such as molecular beam epitaxy and chemical vapor deposition (CVD). Over the past decade the material growth technology basically improved by having more clean systems and by decreasing the troublesome impurity density due to the vacuum quality of the growth chamber. These impurities can be classified as unintentional shallow and deep impurities. The analysis of shallow and deep levels in a semiconductor layered system is a complex task. Nonetheless it is necessary to identify them and characterize their electrical activity in order to control the effect they have on the electronic properties of the grown materials[25]. A well-known example for a shallow impurity in GaAs is the carbon acceptors. GaAs structures grown in state-of-the-art MBE machines typically show residual p-type conductivity that can

be attributed to substitutional carbon, which has a binding energy of 25 meV. The source of carbon contamination is usually outgassing from the growth chamber walls. Hence the partial pressure of external particles should be reduced to a minimum[26]. There are also other elements that could be seen as residual shallow donors such as silicon, manganese, sulphur and lead. On the other hand, the role of deep-lying impurity levels in semiconductors became important with the discovery of semi-insulating GaAs (SI GaAs)[27]. The origin of deep levels are impurities such as chromium, copper, and iron[28].

Doping is an essential element to make an active device from a semiconductor and much effort has been spent on intentional doping studies. Clever and controlled manipulation of doping can enhance the device properties and open gates for fundamentally new implementation areas [26].

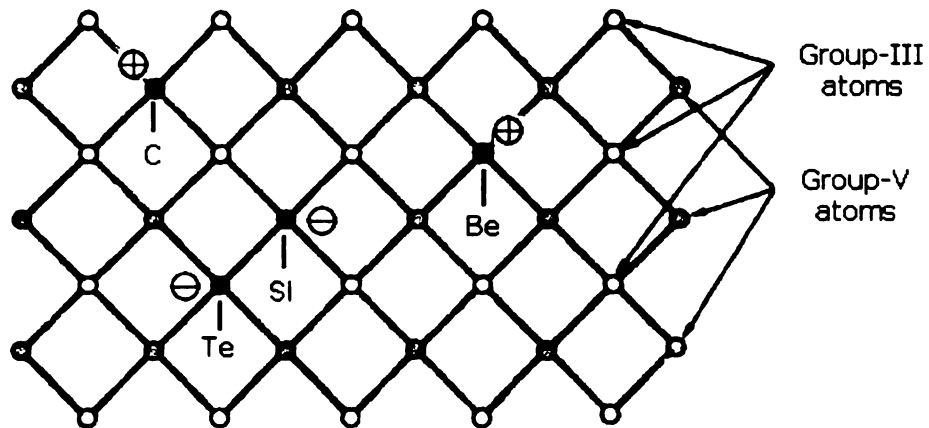


Figure 1.1: Schematic illustration of the zincblende lattice consisting of group-III and group-V elements. The lattice is doped with the donors (Si, Te) and acceptors (Be, C) which have an excess electron and deficit of electrons respectively[5].

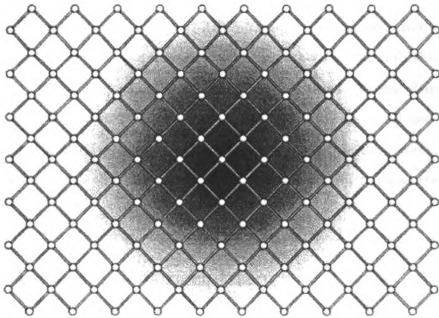


Figure 1.2: Schematic illustration of a hydrogen-like wave function of a donor. The effective bohr radius is much larger than the lattice constant of the crystal.[5].

# Chapter 2: Sample

My work in this thesis is focused on GaAs/AlGaAs, which is a III-V type semiconductor heterostructure. I studied electrons tunneling into the quantum states of donors residing in a doped region. The electrons tunnel from a two-dimensional electron system (2DES). Essentially we utilize the 2DES as an effective base electrode from which the electrons fill the available dopant quantum states.

Our exceptionally high quality sample was grown by Loren Pfeiffer from Bell Labs by the molecular beam epitaxy (MBE) technique. Delta doped layer is the most important ingredient of the sample for the experiments presented in this thesis, since we measure the direct tunneling of electrons into this region. In this chapter, I will introduce the basic techniques such as MBE and delta-doping. I will also introduce the formation of 2DES at the heterojunction. More detailed information about the sample such as key layers, relevant conduction band, and other parameters will be given in chapter 4.

## 2.1 Molecular Beam Epitaxy

Samples used in these studies were grown by the molecular-beam epitaxy technique by Loren Pfeiffer and Ken West at Bell Labs, Lucent Technologies. The molecular-beam epitaxy, or MBE, technique is very simple in its essentials. Here we briefly describe the principles of this method.

Molecular beam epitaxy is a technique for material growth via the interaction of one or several molecular or atomic beams occurs on a surface of a heated crystalline substrate. The molecular beam condition is that the mean free path  $\lambda$  of the particles should be larger than the geometrical size of the chamber. This condition can be achieved by decreasing the total pressure below  $10^{-5}$  torr range (Fig. 2.1). Also, the

condition for growing a sufficiently clean epilayer must be satisfied, e.g. requiring the monolayer deposition times of the beams  $t_b$  and the background residual vapor  $t_{res}$  the relation  $t_{res} < 10^{-5}t_b$ . For a typical gallium flux  $\Gamma$  of  $10^{19}$  atoms/(m<sup>2</sup>s) and for a growth rate in the order of  $1 \mu$  m/hour, the conclusion is that  $p_{res} \leq 10^{-11}$  torr, where  $p_{res}$  denotes the partial pressure of the residual vapor in the MBE chamber. Considering that the sticking coefficient of gallium on GaAs atoms in normal operating conditions is approximately unity and that the sticking coefficient of most of the typical residual gas species is much less than one, the condition above is not so strict; nevertheless ultra high vacuum (UHV) pressures of less than  $10^{-10}$  torr are required.

UHV is the essential environment for MBE. Therefore, the rate of outgassing from the materials in the chamber has to be as low as possible. Pyrolytic boron nitride (PBN) is chosen for the crucibles which gives low rate of gas evolution and chemical stability up to 1400 C; molybdenum and tantalum are widely used for the shutters, the heaters and other components; and only ultra-pure materials are used as sources. To reach UHV, a bakeout of the whole chamber at approximately 200 C for 24 h is required any time after having vented the system for maintenance. A cryogenic screening around the substrate minimizes spurious fluxes of atoms and molecules from the walls of the chamber. In this way despite the technological challenges, MBE systems permit the control of composition and doping of the growing structure at the monolayer level by changing the elements of the incoming beam just by opening and closing mechanical shutters. The operation time of a shutter of approximately 0.1 s is normally much shorter than the time needed to grow one monolayer (typically 1-5 s). Careful variation of the temperatures of the cells via feedback-stabilized controllers permits the precise control of the intensity of the flux to better than 1%. The UHV environment of the system is also ideal for many in situ characterization tools, like the reflection high energy electron diffraction (RHEED). The oscillation of the RHEED signal exactly corresponds to the time needed to grow a monolayer and the diffraction



pattern on the RHEED window gives direct indication over the quality of the surface.

In Figure 2.2 a schematic diagram of a typical MBE system is shown. The solid source materials are placed in evaporation cells to provide an angular distribution of atoms or molecules in a beam. The substrate is heated on a holder to the necessary temperature, which is inside a UHV chamber, and when needed, continuously rotated to improve the growth homogeneity.

The molecules that emerge from the effusion cells do not diffuse as in a gas at higher pressure, but form a molecular beam traveling straight without collisions to impinge on the substrate. Growth starts once the shutters of the K-cells are opened and the temperature of the cells controls the flux of each element. If dopants need to be added, additional cells are used. A common dopant for III-V systems, such as GaAs is Si. Atoms of Si are group IV in periodic table and could act in principle as donor or acceptor. In practice, when grown on (100) surface, Si atoms act as donors, giving up electrons. Our sample is grown with Si by modulation doping, also called remote doping described in the following section. Moreover, the dopants in our sample are in a “delta ( $\delta$ )” configuration. For  $\delta$ -doped materials, the dopant layer is very thin, close to a monolayer thickness.

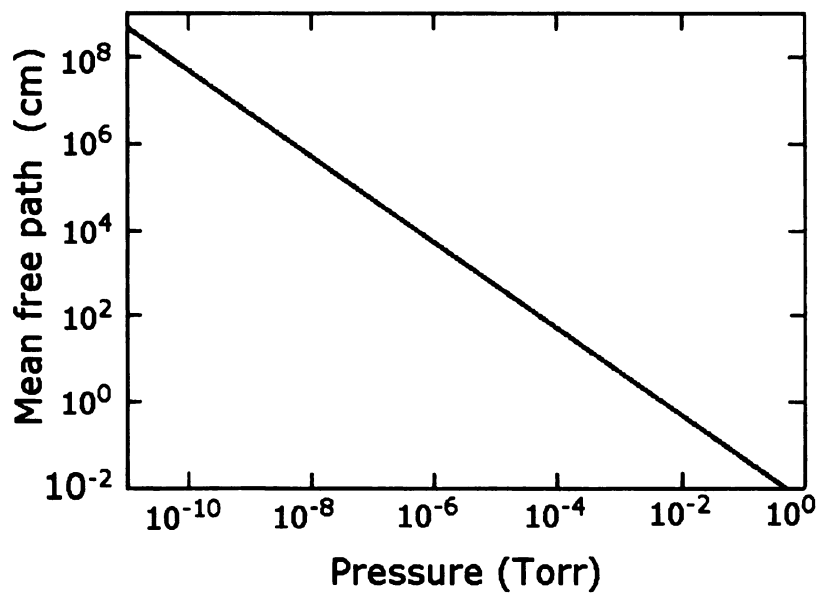


Figure 2.1: Mean free path for nitrogen molecules at 300K.

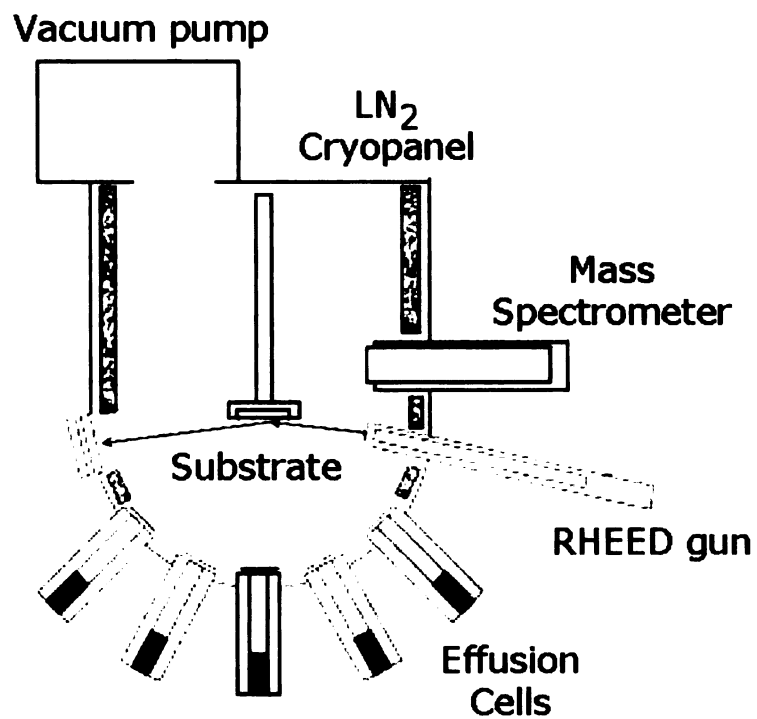


Figure 2.2: Simplified schematic diagram of an MBE apparatus showing Knudsen cells or effusion cells for different source materials with shutters. The sample sits on a heated holder, which is rotated during the growth of the sample.

### 2.1.1 Effusion Cells

The effusion cells used in MBE systems exploit the evaporation process of condensed materials as molecular flux sources in vacuum[29]. The elements that compose the heterostructure are vaporized in these individual furnaces with orifices directed towards the substrate, but shielded from it by shutters. These furnaces are called the Knudsen cells or K-cells. The reasons for the UHV environment are the following: First, it is important to prevent contamination of the substrate. Secondly and more importantly, low pressure is advantageous for molecular flow without collisions with other molecules. In this regime, the mean free path of a molecule is much larger than the length of the chamber, so molecules do not suffer collisions in their path until they meet the substrate[23]. This is the Knudsen or molecular-flow regime of gas. The Knudsen evaporation thus provides a constant flux of the material, providing a molecular beam that is independent of the microscopic properties of the growth surface. The Clapeyron equation describes equilibrium pressure  $p_{eq}$  is denoted as a function of temperature( $T$ ):

$$p_{eq}(T) = A \exp\left(-\frac{\Delta H}{k_B T}\right) \quad (2.1)$$

$\Delta H$  in equation 2.1 is evaporation enthalpy and  $k_B$  is the Boltzmann constant. Under this equilibrium condition the incoming and outgoing flux on the growth surface can be treated independent from each other when  $p_{eq}$  is very low. An ideal Knudsen cell needs to have two basic properties:

- It must be composed of a large enclosure were the condensed material is in thermodynamic equilibrium with the gas phase.
- The orifice size must be so small that the equilibrium pressure  $p_{eq}$  is not perturbed.

The orifice geometry has to fulfill two additional conditions, one for the diameter  $d$ , that fulfills  $d \ll \lambda$ , i.e. the mean free path, at  $p_{eq}$  and one for its wall thickness  $L$ , assumed to be vanishingly thin. Under these conditions, the orifice is a surface with an evaporant pressure  $p_{eq}$  which does not reflect any of the incoming molecules, resulting in surface accommodation is almost 100 % [29].

## 2.2 Formation of Two-dimensional Electron System and $\delta$ -Doping

### 2.2.1 2D Electron System Formation

As emphasized in the previous section, utilizing the MBE technique, it is possible to grow GaAs semiconductor crystals one atomic layer at a time. Moreover the material composition can be changed in successive layers. In this section, a discussion of the formation of the 2DES in the GaAs/ $\text{Al}_x\text{Ga}_{1-x}\text{As}$  heterostructure via the delta-doping technique will be presented briefly.

Gallium and arsenide are in the same row of the periodic table with atomic numbers of 31 and 33, respectively. GaAs is a semiconductor compound formed of these two elements. By substituting the Ga atoms with Al, it is possible to change some electrical properties of the compound such as its energy band gap. The rate of Al substitution  $x$  in our sample is 0.3. The two materials have very similar lattice and dielectric constants and they do not suffer from the lattice mismatch, namely the strain effect. This is one of the greatest advantages of the III-V group heterostructures over the other systems such as SiGe. The quantum well emerges due to the band gap difference of the layers and doping. Doping the material with silicon provides the system with an electric field perpendicular to the interface. The conduction band of the wafer at the interface has an abrupt step, as shown in Figure 2.3. The

$\text{Al}_{0.3}\text{Ga}_{0.7}\text{As}$  that has a wider band gap and it is doped n-type by silicon atoms, so that it has mobile electrons in its conduction band. GaAs with a smaller band gap is typically p-type, with few holes in its valence band. The electrons in the conduction band of  $\text{Al}_{0.3}\text{Ga}_{0.7}\text{As}$  migrate to fill in these holes, but usually end up at the bottom of the conduction band of GaAs. However, positive charge is left on the donor impurities due to migration, which attracts these electrons back toward the interface and bends the band in the process, forming a quantum well. In other words, electrons are transferred, from  $\text{Al}_{0.3}\text{Ga}_{0.7}\text{As}$  to GaAs, forming a dipole layer. The dipole layer makes the Fermi level of the GaAs equal to that of AlGaAs. This is shown in Figure 2.4.

At very low temperatures ( $T \sim 4\text{K}$ ) nearly all of the electrons are in their lowest eigenstates with respect to the motion perpendicular to the well. Therefore the electrons are trapped along the interface and the 2DES is obtained.

A refinement made by leaving a spacer layer of undoped AlGaAs between the n-AlGaAs and GaAs, increases the separation between the electrons and the donors. This further reduces the scattering and increases the mobility of the 2DES, but at the cost of a lower density of electrons.

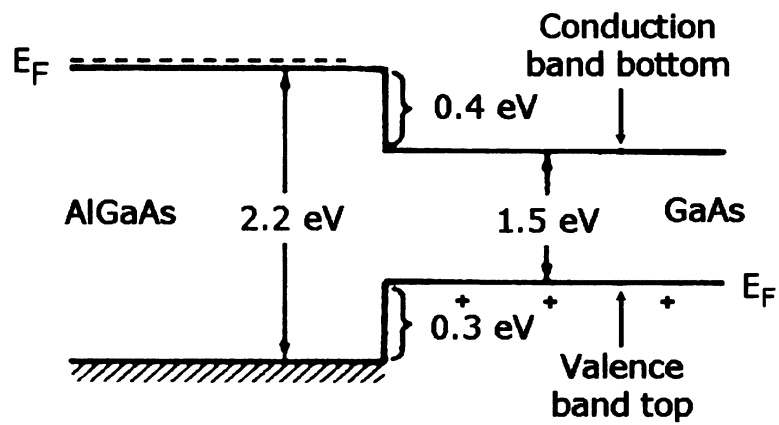


Figure 2.3: The energy-level diagram of AlGaAs and GaAs without energy band bending.

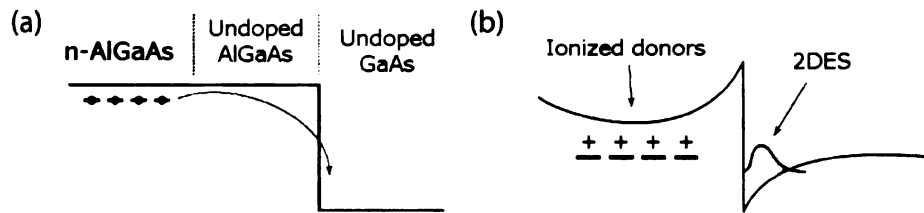


Figure 2.4: The 2DES in GaAs. (a) Using molecular beam epitaxy, layers of semiconductors with different chemical composition can be grown on top of each other, a single crystalline layer at a time. This is used to create structure that has a GaAs layer below an AlGaAs layer. The AlGaAs layer has a larger band gap, leading to a step in the effective potential electrons see. (b) Electrons from dopants in the AlGaAs layer fall into the more energetically favorable undoped GaAs layer, where they form a 2DES at the interface [6].



## 2.2.2 Delta ( $\delta$ ) Doping

The MBE technique is a key tool to produce clean and atomically defined layers and it is also very important for band-gap engineering. An important part of this technique is to implant the donors in the AlGaAs physically as far away from the interface as possible. This reduces the scattering of electrons in the well by the positive donors and increases the mobility of the 2DES many fold. This kind of doping is called remote or modulation doping. Delta doping is motivated by the necessity of well-defined, spatially narrow doping profiles in semiconductors. Doping profiles with high peak concentrations and narrow width distributions are having beneficial affects on many device applications. The narrowest doping profile is achieved if dopants are confined in single atomic layer in the host semiconductor crystal (Figure 2.5).

The two parameters characterizing a  $\delta$ -doping profile are the location of the dopant sheet and the density of the dopants in the plane. A principal method used to achieve the delta-function-like doping profile is the suspension of growth of the host semiconductor by closing the effusion cells during the introduction of the dopant source, and subsequent capping of the host material. It is assumed that the halted growth surface is atomically flat with few atomic terrace steps on the surface. If the dopant atoms do not re-evaporate, then they can form bonds with the atoms on the host semiconductor atoms. In an ideal  $\delta$ -doping profile all the dopants occupy substitutional lattice sites on the surface. Subsequent capping over the dopant atoms can be done by simply by resuming the growth of the epitaxial host semiconductor after terminating the deposition of the doped layer. However, if the semiconductor surface on which the dopant atoms are deposited is rough and contains significant terraces or steps, or if thermally stimulated redistribution of impurities occur during the subsequent growth, then the dopants can not be confined to a single monolayer. Most of the delta-doped growth structures by atomic layer precision are deposited by molecular beam epitaxy due to low growth temperatures ( $<600$  C), which prevents

significant broadening of the dopant profiles. This kind of growth procedure allows the formation of two-dimensional (2D) electrons (for n-type doping) which reside in the unique V-shaped potential well in the host material.

The density of dopant atoms in the doped monolayer is proportional to the dopant flux and the time the semiconductor surface exposed to the dopant flux. Thus, by playing with these parameters one can vary the density of the 2D electron density from sample to sample.

In actual  $\delta$ -doped semiconductors, dopants may not be confined to a single atomic layer but may be distributed over more than a single layer. The factors resulting in broadening of the dopant layer over more than a single atomic layer may be surface roughness and other processes such as diffusion, drift, and segregation. The simplest approximation to quantify the spread of dopants in  $\delta$ -doped semiconductors is the “top-hat” distribution (Figure 2.6).

The width of the  $\delta$ -doped layer usually smaller than the lattice constant,  $a_0$ , however for sufficiently strong doping redistribution processes the width  $\Delta z_d$  may become larger than the lattice constant,  $a_0$ . For these kind of dopant profiles, the maximum concentration and the profile width are related by

$$N^{2D} \approx N^{max} \Delta z_d \quad (2.2)$$

Practically, what is the criteria of having a  $\delta$  function-like doping profile? The answer of this question can be found by comparing the profile width with some relevant length scales such as screening length, free-carrier diffusion length, depletion length, and free-carrier wavelength, etc. The dopant distribution width,  $\Delta z_d$  must be smaller than the shortest of these length scales. De Broglie wavelength of the free-carriers (i.e., electrons or holes) is usually the shortest of these lengths. In a semiconductor crystal this quantity is typically  $\sim 2.5$  nm. Therefore, the distribution

width must satisfy the condition  $\Delta z_d \leq 2.5$  nm for a doping profile to be considered as  $\delta$ -function-like.

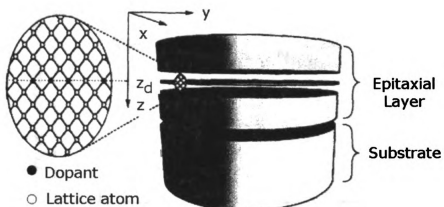


Figure 2.5: Schematic illustration of a semiconductor substrate and an epitaxial film containing  $\delta$ -doped layer. it is also shown that the impurity atoms are confined in a single schematic atomic layer[7].

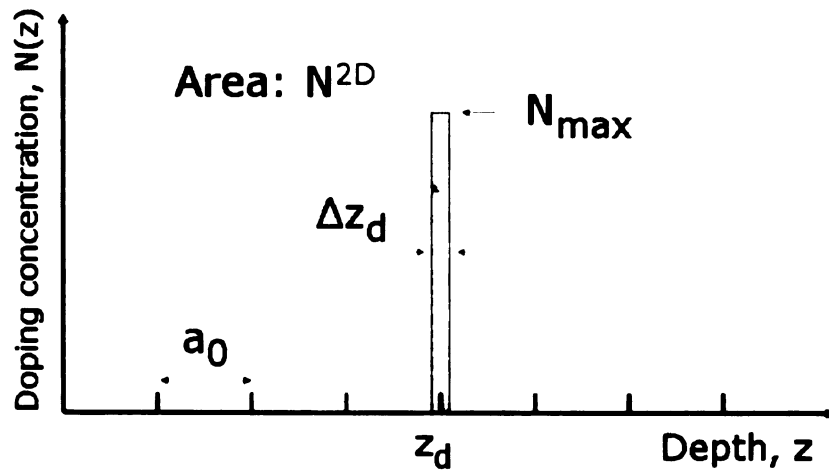


Figure 2.6: Doping profile of a doping spike located at  $z = z_d$  with 2D density of  $N^{2D}$ , maximum concentration  $N^{max}$ , and full-width at half-maximum of  $\Delta z_d$  [7].

# Chapter 3: Experimental Setup and Technique

## 3.1 Introduction

The ability to manipulate and probe the electrons in nanometer-scale systems of dopant atoms and quantum dots represents an emerging line of research. These experiments are motivated by the continued miniaturization of semiconductor devices and potential applications where single charges and spins form the functional part of the device. Techniques used to characterize such semiconductor systems vary depending on the physical quantity desired to be measured. Moreover, the characterization of physical and chemical properties of nano-structures requires techniques with high sensitivity and appropriate spatial resolution[2][30][1][31][19][32]. Scanning probe microscopy (SPM) refers to a class of techniques that use a sharp tip to achieve excellent spatial resolution. Since the donor layer atoms or 2DES is 60-80 nm below the surface of the GaAs/Al<sub>0.3</sub>Ga<sub>0.7</sub>As heterostructured sample, it is practically impossible to use the well-known scanning tunneling microscopy (STM) technique or conventional atomic force microscopy (AFM) to investigate the subsurface physical properties. Low-temperature electric-field-sensitive scanning probe methods have the potential to locally resolve electrons in these systems; such methods include scanning single-electron transistor microscopy[33][34], charged-probe atomic force microscopy[35][36], and subsurface charge accumulation (SCA) imaging[37][38].

## 3.2 Charge Accumulation Imaging

Charge accumulation imaging (CAI)[37] is a cryogenic scanning-probe capacitance technique that can sense the electric field emanating from a sample. Hence, it can locally measure the activity of mobile charges within an underlying quantum system like the dopants or 2DES. An AC excitation is applied to the sample via a base electrode, and a metallic tip is scanned above the top of the sample very close to the surface. The charge is detected by a cryogenic sensor constructed from a high electron mobility transistor (HEMT)[8], which is mounted very close to the metallic tip. The sample and the cryogenic sensor chip with the tip are mounted on a “beetle” type scan head which can also be implemented as scanning tunneling microscope. The microscope sits at the end of a very long stick, with the help of which the microscope is dipped into a liquid  $^3\text{He}$  cryostat, which operates at a base temperature of 270 mK.

Charge accumulation imaging essentially is a capacitive measurement technique, where the tip and sample can be thought as two plates of a capacitor. The schematic diagram for this can be seen in Figure 3.1. The image charge induced on the tip as a response to an a.c. excitation voltage is measured.

CAI is based upon the subsurface charge accumulation imaging (SCA) technique which is developed and implemented by Tessmer et al. with a few significant modifications. For instance, instead of using direct ohmic contact to the quantum system of interest, we apply a vertical tunneling geometry method from the base electrode. The base electrode is typically a heavily doped metallic substrate located 40 nm below the quantum system. The schematic of vertical geometry is seen in the Figure 3.4. Having an ohmic contact to base electrode is advantageous because our measurement becomes insensitive to bulk conductivity of the quantum system. This allows us to probe the system even when it is non-conductive. For example, in a quantum Hall effect (QHE) system, an insulating state, which is called incompressible liquid, results

at certain values of magnetic field when the 2DES is close to an integer Landau level filling. In this case, having the direct contact to the 2D layer would not allow electrons to enter the bulk of the system and subsequently accumulate right beneath the apex of the tip; therefore, our local signal would disappear. As shown in Figure 3.4 (a) our method of measurement with a vertical tunneling geometry does not suffer from this problem. Electrons can enter the available quantum levels in the sample vertically without traveling horizontally through the bulk of the 2DES.

We can apply the method in two ways:

- Scanning-probe: We can scan the tip to acquire the map-like images of the electron density variations while holding sample voltage and magnetic field is fixed.
- Fixed-tip local measurement: We sweep the sample voltage or magnetic field with the tip at a fixed position a few nanometers away from the surface to acquire a capacitance profile.

To understand the capacitance measurement of a quantum system residing inside the sample, we can begin by approximating the tip as a parallel plate. of course, variations of the sample-tip capacitance will result in a change in the amount of charge induced on the tip as a function of excitation voltage. The tip-sample capacitance can change due to the geometric factors such as variation of tip-sample separation. Also quantum contributions arise when one of the plates of the capacitor is not a perfect metal, but instead a material with a finite thermodynamic density of states  $D = dn/d\mu$  such as a semiconductor. In this case, the measured capacitance is reduced from the purely geometric capacitance: for a parallel plate geometry  $C_{meas}$  is given by

$$\frac{1}{C_{meas}} = \frac{1}{C_{geom}} + \frac{1}{e^2 A \frac{dn}{d\mu}} \quad (3.1)$$



where  $e$  is the electron charge and  $A$  is the area of the capacitor. The origin of the effect can be understood by considering the electrostatic potential difference  $\Delta U$  arising from an applied voltage. If the chemical potential of the semiconductor varies by an amount of  $\Delta\mu$  due to a change in its electron density, then the electrostatic potential difference between the plates is:

$$\Delta U = V - \Delta\mu. \quad (3.2)$$

Measuring the charge on the plates, we would find a charge

$$Q = C_{geom}(V - \Delta\mu), \quad (3.3)$$

leading to a reduction of the measured capacitance. Through this electrochemical contribution to the capacitance, CAI can in principle be used to image local changes in the density of states of the underlying quantum system [6].

Since we measure the resonant tunneling a.c. signal in a vertical geometry, the vertical tunneling resistance between the layers, and the capacitances of the bulk 3D substrate, and the quantum system can be thought as an RC equivalent circuit. As we apply the a.c. excitation to the metallic substrate, the tunneling into the quantum system is not instantaneous; there may be a time delay between the measured charge on the tip and the applied a.c. excitation. Thus the measured signal has two components, one in phase with the applied excitation and the other  $90^\circ$  out of phase with it. We call the in-phase capacitance signal  $Q_{in}$ , and the out-of-phase signal  $Q_{out}$ . Figure 3.2 shows the actual tip-sample arrangement and the equivalent circuit. For simplicity, the capacitance between the tip and the quantum system can be thought of as a parallel plate capacitor  $C_{tip}$ . Similarly the capacitance between the quantum system and the metallic substrate is another parallel plate capacitor  $C_T$ , which is in parallel to the tunneling resistance  $RT$ . These form an RC circuit. The plot of  $Q_{in}$

and  $Q_{out}$  with respect to the logarithm of the applied frequency  $f$  or the tunneling resistance  $R_T$  is shown in Figure 3.3.

The plots can be understood qualitatively as follows: For low frequencies, the charge has enough time –compared to the time constant ( $\tau$ ) of the RC circuit– to tunnel into the quantum system and thus stays in phase with the applied a.c. excitation. Hence the in-phase signal, which is purely capacitive, dominates, while the out-of-phase signal is almost zero. As the frequency is increased, the excitation period becomes comparable to the RC time constant, and the measured signal goes out of phase with the applied excitation. Hence the signal shows up mostly in the  $Q_{out}$ , which peaks at a certain value of the frequency  $f_0$ , while the  $Q_{in}$  rolls off. As the frequency is further increased, the excitation period is very short compared to RC and the charge has almost no time to tunnel into the quantum system. Hence both the in-phase and the out-of-phase signal go down.

We can reflect the similar argument on the in-phase and out-of-phase versus the tunneling resistance. The charging components have the identical functional dependence on the frequency  $f$ , and the tunneling resistance  $R_T$  with characteristic values of

$$f_0 = \frac{1}{2\pi R_T (C_T + C_{tip})},$$

$$R_0 = \frac{1}{2\pi f (C_T + C_{tip})}.$$

The magnitude of the curves is set by the tip-sample capacitance difference  $C$  between a fully charging and locally non-charging quantum system. It is also interesting to note that for small resistances ( $\omega RC \ll 1$ ), the in-phase signal will begin to change as:

$$Q_{in} \propto 1 - (\omega\tau)^2, \quad (3.4)$$

where  $\tau = R(C_T + C_{Tip})$ . The out-of-phase signal will be linear in  $\omega\tau$  :

$$Q_{out} \propto \omega\tau. \quad (3.5)$$

Thus, small changes in the tunneling resistance will show up stronger in the lagging phase signal than in the in-phase signal.

A schematic picture of the arrangement for our sample including the donor layer is shown in Figure 3.4 (b). The  $\delta$ -doped Si donor layer is located at 60 nm below the surface of the sample and 20 nm above the above the 2D layer. At sufficiently positive voltages on the tip, electrons enter the 2D system and then tunnel further into positively charged Si donor layer. Thus, we can study the tunneling spectroscopy of the system of ionized donors.

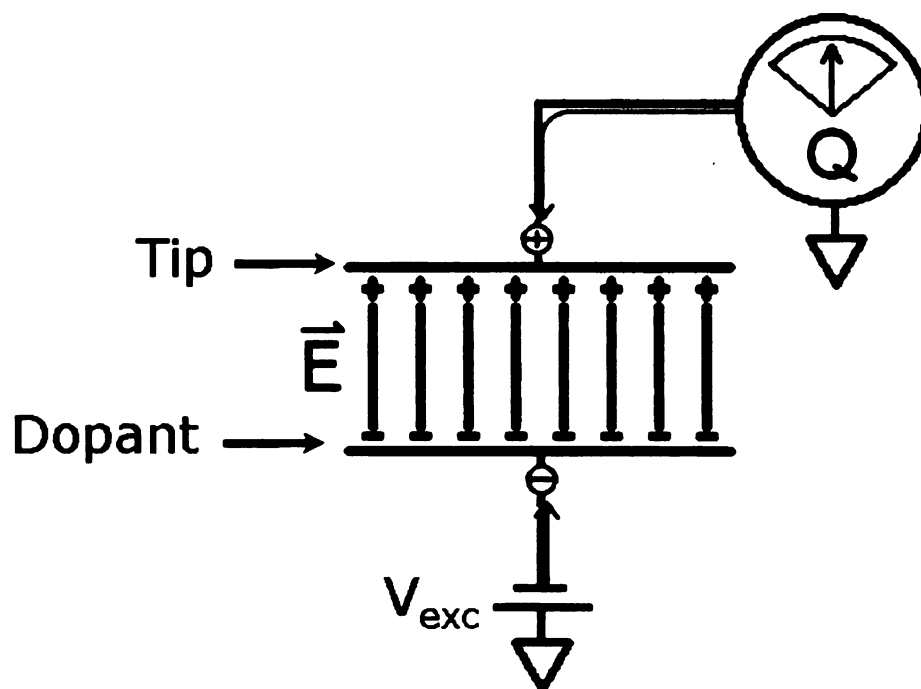


Figure 3.1: Schematic of the CAI technique. CAI is a capacitive technique in which the tip and the quantum system residing below can be thought of as the two plates of a capacitor, with a voltage being applied to the system below that charges up the tip.

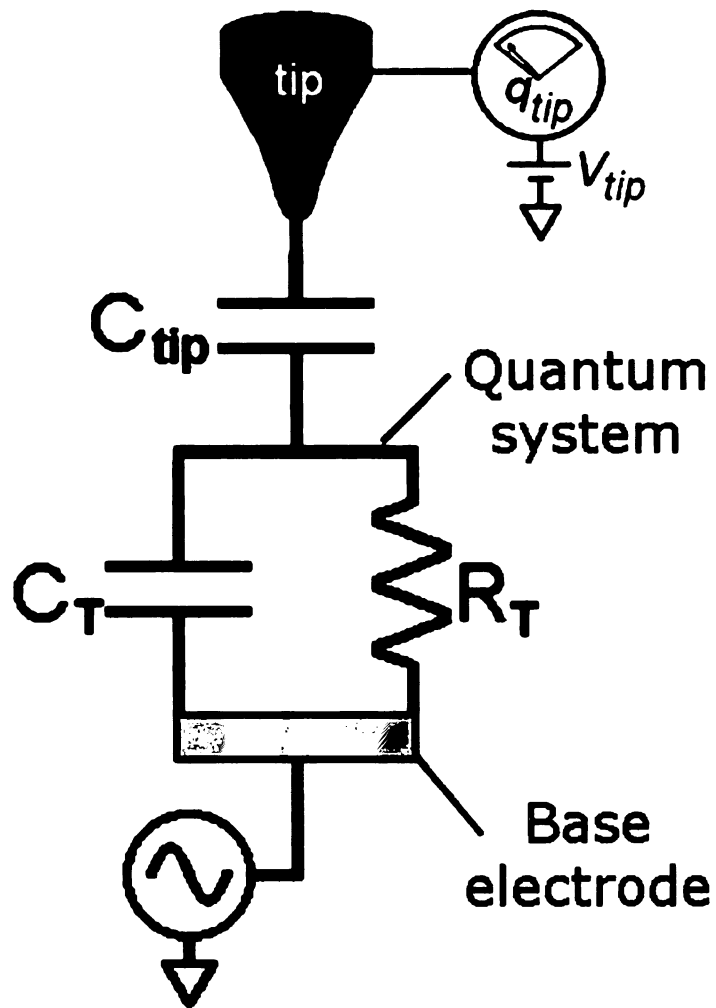


Figure 3.2: The circuit equivalent to the tip sample arrangement in the CAI technique.

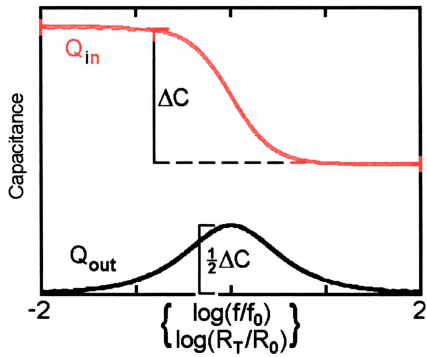


Figure 3.3: The in-phase and the out-of-phase charging as a function of logarithmic frequency and tunneling resistance, as obtained from the model circuit. As the frequency is increased, the capacitor does not have time to charge and discharge during the cycle of the excitation. As we pass through  $\omega = 1/RC_{total}$ , the in-phase signal rolls off while the lagging-phase signal exhibits a peak.

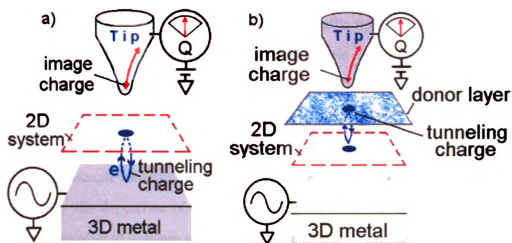


Figure 3.4: Schematic of the vertical tunneling geometry. (a) In the 3D-to-2D case we probe the charging of the 2DES. (b) In the 2D-to-donor layer case we probe the charging of the donor layer. In both cases an ac excitation is applied to the 3D metallic substrate which resides below the tunneling barrier. The charge tunneling into the 2DES or to the donor layer induces an image charge on the tip, which is measured by a cryogenic charge sensor circuit.

### 3.3 Scanning Probe Microscope Design

Scanning-probe microscopy (SPM) reaches out many aspects of the surface and subsurface sciences, including conducting and non-conducting surfaces. There are many techniques developed to study the physical and chemical properties of condensed matter. For example, Binnig and Rohrer designed the first scanning tunneling microscopy (STM) in 1982 and achieved first atomic resolution surface topography or high quality spectroscopy[39, 40]. Later, STM was also used to manipulate atoms spatially on smooth surfaces with a very sharp metallic tip[41]. To be able to study the surface and subsurface characteristics of the sample one must tackle some significant instrumental challenges. First of all, it requires very high stability of the scan head, which leads to small piezo-electric material lengths and therefore small scan ranges. It is also fundamentally important that the microscope have the ability to translate the sample laterally in-situ. The quantum system we study can be easily perturbed by the deposition of charge on the insulating surface of the sample. Having such translational freedom allows us to walk to a new unperturbed location if the area we are scanning is disturbed. Moreover, it opens up the possibility of studying lithographically defined structures such as quantum dots.

The physics that was studied in our experiment requires hours of stable operation to achieve an acceptable signal-to-noise ratio. Moreover, the physics of our experiment requires a micron-scale scan range. It is actually a challenge to build a piezo-electric based microscope with high stability, without compromising on its scan range. In our case, the scan head is immersed into a  $^3\text{He}$ -Oxford cryostat to cool down the sample to desired temperature and the sample rests directly in liquid  $^3\text{He}$  after recondensation. In the conventional Besocke[42] or “beetle” design (Figure 3.5) the sample sits on the top of the carrier piezo-tubes. Therefore using long piezo-tubes to achieve big scan ranges not only compromises the stability, but also keeps the sample at a high position relative to the bottom of the scan head. As a result, for direct immersion in



liquid  $^3\text{He}$ , the liquid level may soon drop down below the level of the sample, causing the sample to warm up before any desired data can be acquired. Instead, another type of scheme called “upside-down Besocke design” [43] in which the sample and tip sits lower on the scan-head compared to the previous one, with the larger scanning piezo-tubes leads to proportionally larger scan range. The upside-down design meant to fulfill three major requirements:

- Thermal stability
- Relatively high scan range
- Positioning the sample location as close as possible to the bottom of the scan-head

A schematic of the design is shown in Figure 3.6, and the actual microscope is shown in Figure 3.7. Three carrier piezo-tubes positioned in a trilateral geometry, and the center-piezo-tube which is used for the scanning, are all soldered to the top plate. Carrier-piezos hold the ramp where the sample holder is screwed in and the center piezo holds both sensor circuit on which the sharp tip is attached via conducting low temperature epoxy. Since the carrier and the center piezo tubes are identical, thermal contraction of the three carrier piezo tubes, which tend to move the sample towards the tip, is compensated by the tip moving upwards, away from the sample as the center piezo-tube to which the tip is attached contracts exactly by the same amount. Therefore, the microscope is thermally compensated, namely, temperature changes do not affect the tip-sample separation. Secondly, as it is seen from the geometry of Figure 3.6 and from the picture of the microscope (Figure 3.7), the sample rests almost at the very bottom of the scan-head, so that the microscope only warms up when the sample space in the cryostat runs out of liquid  $^3\text{He}$ .

The piezo tubes are 7.6 cm long and are soldered to a brass base plate, which is rigidly attached to a 2 m long stainless steel tube which serves as a guide to the

coaxial wires and ribbon cable to be connected to the outer world. As it is indicated before, the longer the piezo tube length, the larger the capability of area scanned by the microscope. The 7.6 cm piezo tube length provides about  $12 \mu\text{m} \times 12 \mu\text{m}$  scan area at base temperature of the  $^3\text{He}$  system ( $\sim 300 \text{ mK}$ ). The sample rests on the small feet that are part of the cylindrical legs, as indicated in Figure 3.6 (a). A mechanism inside the legs allows for the rotation of each supporting foot by  $180^\circ$ . This allows for the brass displacer, used for screening electric field of the piezo tubes, to be installed and removed. Each leg consists of a piston rigidly attached to the foot, and a small Be-Cu compression spring. The resulting upward pressure on the piston presses the supporting piece against the leg, without limiting its rotational motion. This is shown in Figure 3.6 (b). A groove made in the leg fixes the piece in two positions, directed inward or outward. The sample holder diameter is slightly bigger than the opening between two legs. Hence two out of the three legs are notched longitudinally, and the sample is mounted through the gap between them.

Figure 3.6 (c) shows the schematic bottom view of the scan-head assembly. The sample holder is designed as a Besocke ramp (Figure 3.5)[42, 44] except that the sloped ramp is located on one side and the sample is on the opposite side. A slope of 2 is determined for the ramp, yielding a coarse vertical positioning range of 0.4 mm. Moreover, the sample sits on a positioning screw that allows a coarser manual vertical positioning in the range of almost 1 cm. This is important in preventing the tip from being accidentally crashed during the insertion of the sample. In practice, the sample is typically 0.5 cm from the tip after initially inserting the sample holder. Of course, before we can turn the positioning screw to bring it closer, the position of the ramps must be fixed. This is accomplished by pinching the sample holder from the sides using the three clamping screws, shown in Figure 3.6 (c). The clamping screws are attached to the brass displacer that also serves to screen the electric field generated by operating the piezo-electric tubes. After the clamping screws are removed, an end

cap is put in place. The interior of this cap provides a smooth surface for contact with the sides of the sample holder. We ensure low friction by applying  $MoS_2$  powder to the interior surface of the cap in addition to the sides and the ramps of the sample holder. The microscope is cooled by slowly lowering the probe into the cryostat at a cooling rate of 1 K/min. There is little risk of mechanical vibrations causing a crash during this procedure, as gravity tends to pull the sample away from the tip. Finally, the fine sample approach is achieved by the standard inertial walking procedure (namely, slip-stick motion) utilized in “beetle-type” designs. We find our scanning piezo tube (7.6-cm-long x 4.8-mm-diam x 0.8 mm wall thickness) to have a sensitivity of 1300 /V laterally and 73/V vertically at liquid-helium temperatures. Using commercially purchased electronics from RHK Technology, Inc., which provide a voltage range of 130 V, we thus achieve an impressive cryogenic lateral scan range of 34  $\mu$ m. The same large range of motion of the carrier piezo tubes also enables us to do the fine sample approach very quickly. Typically, the full range of the ramps is traversed in approximately 2 min at liquid-helium temperatures. We find the microscope to be sufficiently stable to function without a low-temperature vibration isolation stage. With regard to the entire cryostat, we have taken care to minimize building vibrations using a bungee-cord suspension system. Mechanical pumps, which are part of the cryogenic system, represent a major source of additional vibrations. We have decoupled those modes by using tubing that has a section made of flexible rubber, connected to a section of stainless steel. That produces an impedance mismatch so that part of the vibrations is reflected at the junction[45]. We have also connected the tube rigidly to a heavy lead block at one point and immersed it into a sandbox at another[46].

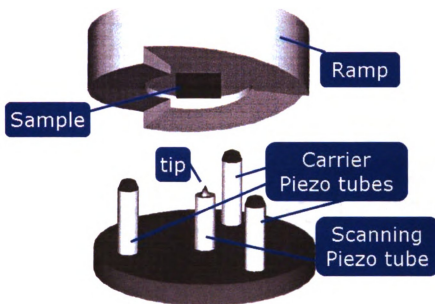


Figure 3.5: Schematic of the Besocke type scanning head. Three carrier piezo-tubes are supporting the sample holder ramps. The sample sits upside-down rigidly mounted on the sample support disk. The outside carrier tubes and the middle scanning tube are all attached to a bottom plate.

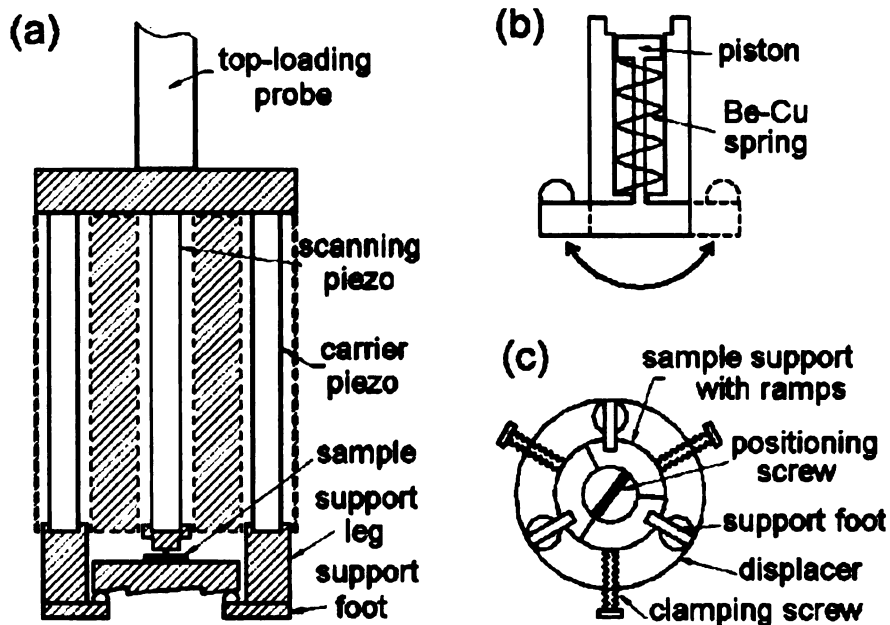


Figure 3.6: (a) Schematic of our scanning head. Both the tip and the sample are supported by identical piezoelectric tubes (dimensions: 7.6 cm-long x 4.8 mm-diam x 0.8 mm-wall thickness). As a result the unit is nearly perfectly thermally compensated. The displacer, outlined in dashes, screens the tip from the electric fields of the piezo-tubes. All the metal parts are made of brass, shown hatched. (b) Sketch of support leg showing the rotating foot assembly. (c) Bottom view of the microscope. The clamping screws fix the ramps to allow the positioning screw to be turned-the sample is attached to the other side of this screw. In this way, we can adjust the vertical position of the sample by as much as 1 cm. The diameter of the unit is 3.8 cm.

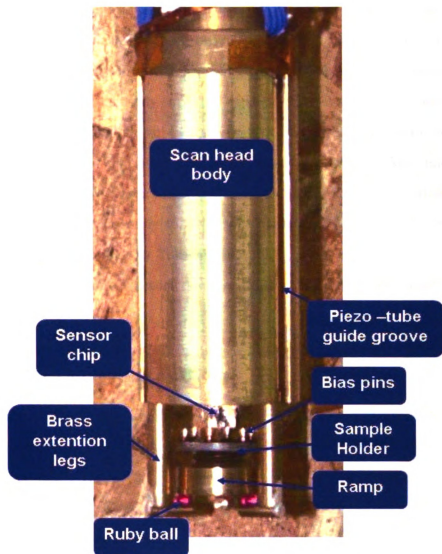


Figure 3.7: Photograph of the actual microscope. The shiny ruby balls at the end of each foot help reduce friction during fine approach of the sample.

## 3.4 The Cryogenic Charge Circuit

Since the most interesting physics is observed at very low temperatures in heterostructure semiconductors, we have to implement circuit elements that have excellent low temperature properties. There are several types of transistors that could be used for constructing a charge sensor, but most of them are not suitable for our experiments due to incompatibility with low temperatures. For example, bipolar junction transistors depend on thermally activated carriers. Those would be impossible to use because their charge carriers will be frozen out at relevant temperatures. In general, field effect transistors (FETs) are used for cryogenic applications. We build our circuit utilizing two high electron mobility transistors (HEMT) which are attached very close to the tip-sample assembly[46, 11]. HEMTs are FETs that were invented at Fujitsu Laboratories in Japan by Takashi Mimura [8], which are GaAs/AlGaAs based modulation doped heterostructure devices. Section 3.4.2 discusses these transistors in detail.

### 3.4.1 The Capacitance Bridge

We used an a.c. charge sensitive technique based on a capacitance bridge to measure the electron activity located 60-80 nm below the surface of a GaAs/AlGaAs heterostructure[37, 47, 48, 49]. In a capacitance bridge, the capacitance of an unknown capacitor is measured against a standard reference[6]. In our experiment, the sample capacitance is formed between the sharp scanning probe tip and the quantum systems below the surface of the sample such as delta-doped silicon layer or 2DES. Here we can analyze the basic operation of a capacitance bridge (Figure 3.8): An a.c. excitation voltage  $V_s$  is applied to the sample capacitance, and another a.c. voltage,  $V_r$ , which has an opposite phase with  $V_s$ , is applied to the reference capacitance which will be represented as standard capacitor later. The voltage generated at the

center point of the bridge is given in terms of  $V_r$ , and  $V_s$ :

$$C_T V = C_s V_s + C_r V_r \quad (3.6)$$

where  $C_T$  is the total capacitance at the center point of the bridge and given by:

$$C_T = C_s + C_r + C_g \quad (3.7)$$

where  $C_g$  is the total stray capacitance to ground. Balancing the bridge is possible by applying a.c. voltages,  $V_s$ , and  $V_r$  with suitable magnitudes and phases resulting in a nulled voltage,  $V$ , at the center point. Balancing the bridge provides us with a measurable sample capacitance as following:

$$C_s = \frac{C_r V_r}{V_s} \quad (3.8)$$

The advantage of the capacitance bridge is that it allows a precise measure of the sample capacitance without needing an independent measurement of the shunt capacitance or of the gain of any amplifiers used to measure  $V$ . In our experiments, we expect small changes in the sample capacitance- of the order of tens of attofarads- as a function of experimental parameters such as tip-sample separation or d.c. bias voltage. Technically, it makes the detection of the sample capacitance much easier, since we are searching a small change in a small signal amplitude instead of a small change in a much larger signal. Assuming that these changes  $C_s$  are small compared to the total capacitance  $C_T$ , then equation 3.9 becomes:

$$C_T(V + \Delta V) = (C_s + \Delta C_s)V_s + C_r V_r \quad (3.9)$$

For a bridge circuit which is previously balanced, the out-of-balance signal becomes:



$$\Delta V = \frac{V_s}{C_T} \Delta C_s \quad (3.10)$$

This can be converted into change in the sample capacitance as a function of experimental parameters. It is also obvious from the equation 3.10 that the out-of-balance signal is inversely proportional to the total capacitance,  $C_T$ . The background capacitance,  $C_g$ , must be minimized to maximize the sensitivity of the bridge. The shunt capacitance of the cables carrying the signal from the base of the cryostat to the lock-in amplifier at which sits in a room temperature environment is of the order of nF. It is a very inefficient technique to use a room temperature amplifier that could lead a huge signal loss while measuring a sample capacitance of the order of fF level. For this reason, we implement and use a cryogenic amplifier that is mounted almost very close to tip ( $\approx 1$  mm), which allows us to reduce the total bridge capacitance  $C_T$  to a value of less than 1 pF.

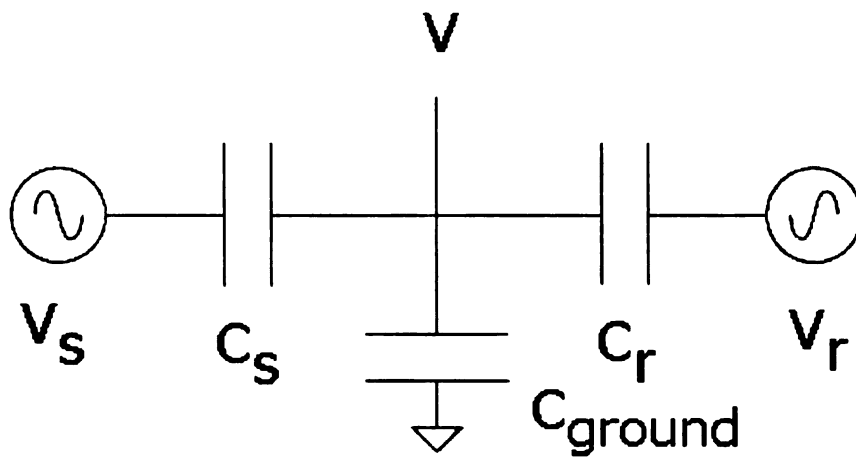


Figure 3.8: Schematic of a simple capacitance bridge. Balancing the bridge involves adjusting the amplitude and phase of  $V_r$  so that the voltage  $V$  at the center of the bridge is zero[6].

### 3.4.2 HEMTs and the Sensor Circuit

For our charge sensor that we use in our experiments, the key advantage is the low input capacitance ( $\approx 0.3$  pF) of HEMTs in comparison with the standard FETs. Moreover, HEMTs can be operated in the ohmic region (Figure 3.11), far away from saturation resulting in the power dissipation is decreased by 2-3 orders of magnitude compared to saturation mode operation[50].

The top-down schematic cross section of Fujitsu model FHX35X HEMT is shown in Figure 3.10. High electron mobility transistors are fabricated using a heterojunction of a highly Si doped n-type  $\text{Al}_x\text{Ga}_{1-x}\text{As}$  layer, n-type GaAs and the undoped GaAs. The value of  $x$  is representative of a fraction of Al in the compound, which is usually 0.3. The epilayers are grown by molecular-beam epitaxy (MBE) on a (100) GaAs substrate. The electrons are generated in the n-type AlGaAs and transferred into the next GaAs layer to form a depleted AlGaAs layer. This happens due to the band-gap difference between AlGaAs and GaAs. This results in a steep canyon in the conduction band on the GaAs side where the electrons can move without colliding with the ionized dopants from which they have originated. This mechanism is exactly how 2D system is usually formed in semiconductor heterostructure which is explained in the previous chapters. In the case of this commercial device, the 2D system is utilized as the conducting channel of the HEMT.

The schematic circuit diagram of the amplifier is shown in Figure 3.12. It is simple and consists of two Fujitsu model FHX35X transistors. The “measurement transistor” is the one on the right which operates in the common-source configuration which has a gain of unity. It picks up the signal and amplifies from the center point of the bridge, at which point the tip is attached. The second transistor shown on the left is called “bias transistor” which is used to provide a high impedance of the order of  $\text{G}\Omega$  and incorporated with a standard capacitor which is implicitly shown in the circuit. The conduction channel of the bias transistor can be “pinched off” to form a large

resistor. This is much convenient than using conventional low temperature resistors, since the transistor's shunt capacitance is much lower. Moreover, it also provides more information about the gain of the measurement transistor by opening up the channel of the bias transistor. This allows us to measure the shunt capacitance of the circuit and input noise of the amplifier. The standard capacitor, which is capacitively coupled to the impedance applied by the bias transistor, is used to subtract away the stray capacitance arising from the background electric field.

Because HEMTs are susceptible to be damaged from static charge, care must be taken during handling, such as application of proper grounding of the bench-top environment while grabbing the HEMT from its package and bonding the gold wires on it during assembling the circuit. We also check for the characteristic fan-shaped family of curves shown in Figure 3.11 of our HEMTs at room temperature before we cool the system down.

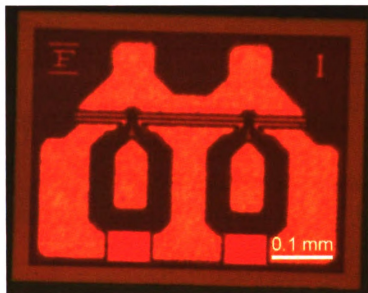


Figure 3.9: A picture of our commercially available device, Fujitsu model FHX35X HEMT, made of GaAs/AlGaAs modulation doped heterostructure. Their low temperature compatibility is excellent with a very low input capacitance.

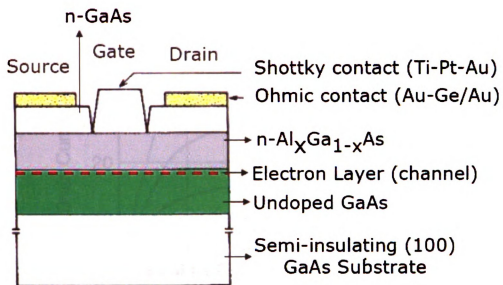


Figure 3.10: Schematic picture of the top-down cross section of a HEMT[8].

### DRAIN CURRENT vs. DRAIN-SOURCE VOLTAGE

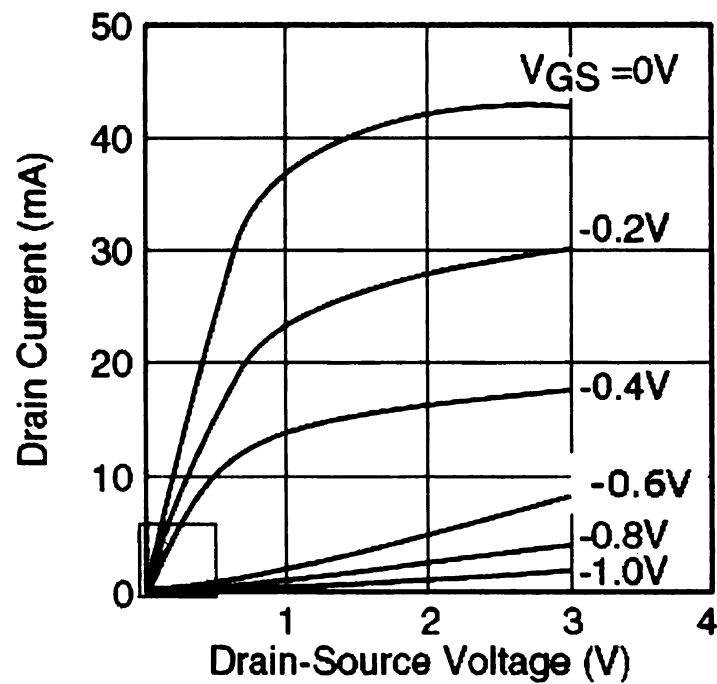


Figure 3.11: Source-drain I-V characteristics, at different gate voltages  $V_{GS}$ , of a typical HEMT. We are operating the circuit at the ohmic regime at which it is shown inside a rectangular box.

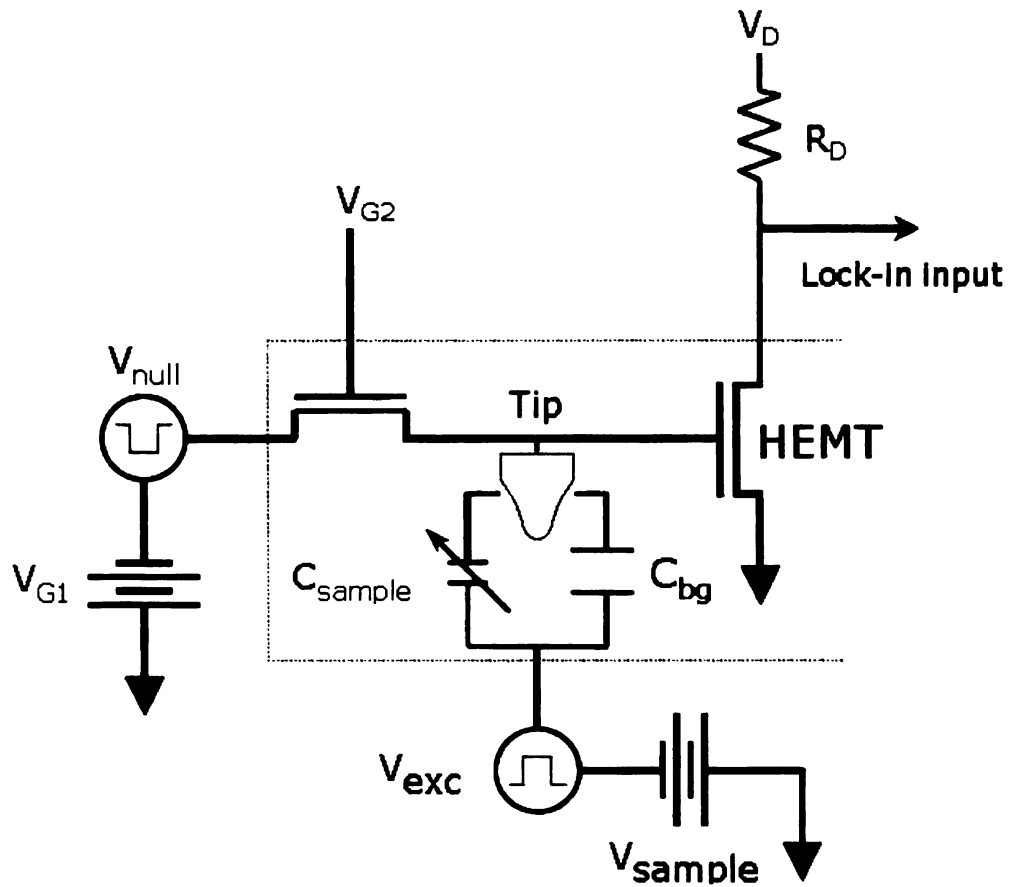


Figure 3.12: Schematic of the cryogenic charge sensor circuit.  $V_{\text{null}}$  is applied to the standard capacitor and  $V_{\text{exc}}$  is the applied a.c. excitation to the sample. The a.c. excitation applied to the standard capacitor, is of the same amplitude but  $180^\circ$  degree out of phase with the excitation voltage that is applied to the sample. The charge sensitivity of the circuit is  $0.01 \text{ electrons}/\sqrt{Hz}$ .



### 3.4.3 Tip

One of the most important parts of the CAI is the extremely sharp STM tip. We used two types of tips in the experiments presented in this thesis: These are platinum/iridium and tungsten tips. Unlike the STM measurements, we have to be very strict concerning the input capacitance of the circuit elements on our sensor chip. To reduce the input capacitance the size of the tip must be adjusted as small as possible. We cut the tip under the optical microscope using a wire cutter which is a very tedious operation. Another crucial part during the operation of the microscope is not to crush the tip. The PtIr and tungsten tips have a radius of curvature of  $\sim 50$  nm and they are very fragile. Dropping the tip during the replacement stage, crushing it during the coarse positioning or any feed-back problem when it is operating in tunneling mode will produce a useless tip. One of the most probable states to produce a crushed tip is to operate the probe in capacitance mode since we turn off the feed-back control. We have to be careful in this mode to avoid bumping any of the features on the surface of the sample. The sample surface must be free from terrain and tall surface contaminants such as micron scale dust particles. To avoid tip-sample crush when working in capacitance mode, we make the slope compensation. Another precaution is to scan the surface in tunneling mode to be certain whether or not there are tall dust particles on the surface of the sample. In Figure 3.13 the SEM picture of the regular and crushed tips are shown.

## 3.5 The Cryostat

We directly mount the bare scan head without the sample and sensor circuit to the end of the  $\sim 2$  m long stainless steel tube. After the scan head is attached, the sensor circuit is carefully placed to the top of the center (scanning) piezo-tube. This procedure must be done deliberately, since the sharp tip with a nanometer scale apex

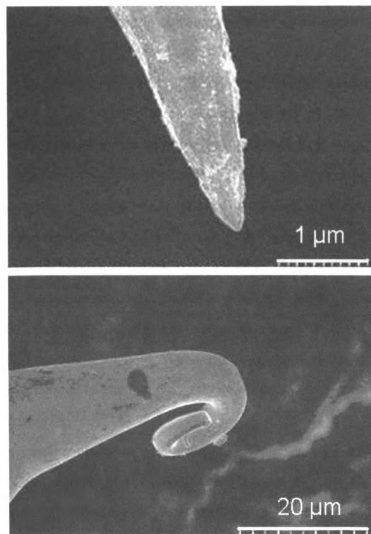


Figure 3.13: SEM micrograph of a regular (top) and a crushed (bottom) Pt/Ir tip is shown. The radius of apex of the tip is approximately 50 nm. Tip must be cut very close to its apex to reduce the input capacitance of the circuit.

is attached to the sensor circuit with the conducting epoxy. It is also important to be cautious not to break the very fragile piezo tubes during the mounting operation. We run the microscope in the tunneling mode at room temperature to test whether walking signal makes the tip get into the tunneling range. Finally, after bench-top controls, we hold the probe with the tip-sample-circuit combination and place it on top of the  $^3\text{He}$  dewar. We lock the probe on the gate and keep the gate valve closed. After pumping the probe down to  $5 \times 10^{-6}$  torr with the turbo pump, we open the gate valve and start to slide the probe inside the dewar very carefully. This operation must be done very slowly for the following two reasons: First we do not want our probe at room temperature to be thermally shocked and let the piezo-tubes break or become depolarized. Secondly, since we set the tip-sample separation is less than 1 mm and any sudden motion may cause tip hit the sample directly. This process of lowering the probe takes approximately 5-6 hours. The cryostat is equipped with a superconducting magnet surrounding the sample space. A magnetic field up to  $10^{-12}$  T can be achieved. Once the microscope is all the way down, it is directly in the middle of the magnetic solenoid. Thus, the magnetic field lines inside are lined up exactly perpendicular to the sample. The schematic picture of this arrangement is shown in Figure 3.14

There are a number of stages before we are able to run the system at the base temperature. The principle of the operation of a  $^3\text{He}$  cryostat can be introduced as following: After all relevant pumping operations and leak checks are fulfilled the whole cryostat is cooled in stages from room temperature to liquid  $^4\text{He}$  temperature of 4.2 K. First, we precool the cryostat down to 77 K by transferring liquid nitrogen to the LHe4 space. Then we deplete the liquid nitrogen ( $LN_2$ ) by siphoning it back and replace the cryostat with liquid  $^4\text{He}$  (LHe4). The sample space is kept under vacuum during the cool-down procedure. The cryostat can be maintained at liquid He4 temperature of  $\sim 4.2$  K for months, by filling it up with LHe4 weekly.

A very simplified overview of the procedure to cool down the system from 4.2 K to the base temperature of 0.270 K is explained below. The most critical part of this procedure is to operate the 1 K pot. It is a small container, which is attached to the sample space from outside. First, we let the 1 K pot draw LHe4 from the LHe4 container via a narrow tube separated by a needle valve and pumped to maintain it at around 1.2 K. The sample space is equipped with a large charcoal adsorption pump, called the sorb, which is another critical ingredient of this procedure. We assume that  $^3\text{He}$  gas has been released already from the storage cylinder into the sample space. At this point the sorb temperature is in equilibrium with the surrounding temperature of LHe4. As a result, He3 in the gas phase gets trapped inside the cold massive surface area of the porous sorb. We then start heating the sorb up to 32 K, causing it to release the  $^3\text{He}$  gas. The  $^3\text{He}$  condenses onto the cold walls of the 1 K pot and drips down to the bottom of the sample space. In order to avoid overheating the sorb and balance the temperature, we use a heat exchanger which cools the sorb with LHe4. This also helps us to maintain temperature below 1.5 K. The process of condensing the  $^3\text{He}$  gas takes about 1 hour. Finally, the base temperature between 0.270 K and 0.290 K is reached by removing the sorb heat; this allows the sorb to pump on the liquid  $^3\text{He}$ . The design of our experiments requires long hours of stable base temperature. Therefore, we run our system in “continuous fill” mode where the 1 K pot helium input valve is slightly open for continues flow of LHe4. The level of opening in the 1 K pot input valve can be adjusted according to its effect on the temperature of the 1 K pot to achieve the lowest base temperature. The sample space remains at the base temperature for about 100 hours, until it runs out of liquid  $^3\text{He}$ . At this point all the  $^3\text{He}$  atoms are stuck inside the adsorption pump to be recycled for the next data run.

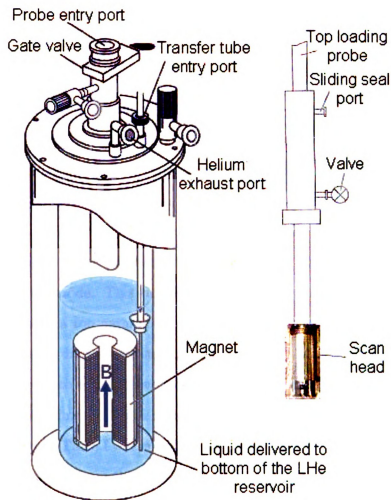


Figure 3.14: (Left) A simplified schematic diagram of the Oxford built top-loader cryostat is shown. The unconventional bungee-cord technique is used to provide the vibration isolation which is not shown in the figure. (Right) Top-loading probe depicted with a picture of our microscope attached from the bottom is depicted. The probe must be inserted slowly inside the cryostat and must be kept there during the experiment. It is surrounded by a superconducting magnet, which is shown in the figure.

# Chapter 4: Donor Molecules and Experiment

## 4.1 Introduction

In this chapter I will discuss measurements of the donor layer charging in our GaAs sample [51]. Si atoms which are randomly distributed on a planar sheet in the  $\text{Al}_{0.3}\text{Ga}_{0.7}\text{As}$  crystal donate their electron to the quantum well created at the interface of  $\text{Al}_{0.3}\text{Ga}_{0.7}\text{As}$  and GaAs. The  $\text{Si}^+$  layer created by Si donor atoms has a density of  $1.25 \times 10^{12} \text{ cm}^{-2}$ . Our study probes the charging of the  $\text{Si}^+$  by allowing electrons to tunnel back into the donor system from a 2D electron system acting as a base electrode. This tunneling will happen when a sufficiently positive voltage is applied to a top gate, or in our case, an effective positive voltage to the tip. The analysis of data shows strong evidence that the Si donor atoms interact with their neighbors to form effective donor molecules. The general outline of this chapter will be as following: I will briefly explain the inspiration of the donor layer charging experiment. Then, I will introduce the gated capacitance and localized probe measurements acquired from the high-quality GaAs sample. I will then present the idea of the donor molecules in the context of the Luttinger-Kohn approximation[3, 52]. Finally, I will introduce the comparison between data and model describing the donor molecule picture established by configuration-interaction calculations. Most of the data presented in this chapter acquired in collaboration with my colleague I. Kuljanishvili.

## 4.2 Spectroscopy of Donor Molecules

In general, single electrons can be resolved by capacitance techniques at liquid helium temperatures if the energy spacing to add successive electrons is on the millivolt scale or greater. As described in detail in Ref. [53], by measuring the capacitance  $C$ , we can detect charges entering the quantum system below the probe. Here for simplicity, we discuss the tip-sample system using a parallel-plate picture. We define the addition energy  $\varepsilon_n$  as the energy for which the  $n^{\text{th}}$  electron enters the donor layer. As  $V_{\text{tip}}$  increases from zero, relative to the 2D-layer chemical potential, the energy of the donor layer with respect to electrons decreases as  $-\alpha_{\text{tip}}eV_{\text{tip}}$ , where  $\alpha_{\text{tip}}$  is the geometry-dependent proportionality constant called the lever arm factor in the literature. In other words, electrons in the underlying 2D electrode are pulled toward the donor layer. The first electron enters when  $-\alpha_{\text{tip}}eV_{\text{tip}}$  crosses the ground state energy of the one-electron quantum state,  $\varepsilon(1) = E(1)$ . As  $V_{\text{tip}}$  increases further, the second electron will be induced to enter when  $-\alpha_{\text{tip}}eV_{\text{tip}}$  equals the energy difference between two-electron and one-electron ground states,  $\varepsilon(2) = E(2) - E(1)$ . In general,  $\varepsilon(n) = E(n) - E(n - 1)$ , where we define  $E(0) \equiv 0$ . The capacitance  $C$  is given by

$$C = \frac{dq_{\text{tip}}}{dV} \propto \frac{\partial \langle n \rangle}{\partial \mu}, \quad (4.1)$$

where  $dV$  corresponds to the excitation voltage,  $\mu$  is the donor layer chemical potential, and  $\langle n \rangle$  the expectation value for the number of electrons in the donor system[53]. Essentially, if an electron is able to enter the quantum system, the excitation voltage causes it to resonate between the system and the underlying electrode—giving rise to a peak in the capacitance.

Electron tunneling spectroscopy through isolated dopants has been observed in transport studies[21, 17]. A hydrogen-like dopant atom is in the core of these studies in terms of its capability of binding a second electron, which is called  $D^-$  state. By

donating the second electron the negatively charged center becomes neutral and it is called as  $D^0$  state. The basic motivation of our scanned probe experiments on donor layer charging is the resonant tunneling device (RTD) measurements[12, 11]. For instance Geim and coworkers reported zero-dimensional states, which result in a resonant structure in the transport experiments. These states are attributed to the random pairs of shallow donors[12]. The additional impurity states can be observed in the current-voltage (I-V) characteristics of a GaAs tunneling device in which the number of these impurity states is controlled carefully. The device is constructed as an AlGaAs double barrier with an intentional Si  $\delta$ -doping in the quantum well. The thickness of the barriers is about 6 nm allowing resonant electron tunneling with a reasonable life time. Tunneling through donor complexes –in this situation paired donors– can be prevailing when the others are out of resonance. Geim has attributed the resonance from deeper levels observed in their I-V curves to a pair of Si donors which are sufficiently in close proximity to be modeled as simple hydrogen-like donor molecules. These ground-breaking resonant-tunneling measurements were not able to resolve the characteristic electronic spectrum of the donor pairs. Statistically having two donor atoms close enough to build a donor molecule in the  $\delta$ -doped region and the possibility of measuring vertical tunneling resonance of through these molecules is motivated us to do a series of measurements.

Here I present and discuss capacitance measurements with a micron-size gate fabricated on top of the sample and localized probe measurements of the electron addition spectrum of silicon donors in a gallium-arsenide heterostructure using a scanning probe technique[51]. This study is the first example of single-electron capacitance spectroscopy performed directly with a scanning probe tip[54]. In addition to the single electron peaks, broader peaks were observed that are consistent with donor molecules, effectively formed by nearest-neighbor pairs of silicon donors[51].

For the local probe measurements, we used a PtIr tip with a radius of curvature



of 50 nm and fixed at a distance of 1 nm from the exposed GaAs surface. Under these conditions, the radius of the area over which we are probing is set mostly by the tip-donor-layer separation, which is approximately 60 nm[55]. Given the  $\sim 60$  nm size of the probed area and average dopant density, we expect to be sensitive to about 140 donors. Figure 4.5 shows an example of the expected energy landscape of the donor-layer quantum system, in the effective-mass picture[3].

## 4.3 Measurements

### 4.3.1 Gated-Capacitance Measurement

Before introducing a more detailed description about the donor layer charging, I will present a capacitance measurement performed on a sample from the same wafer. I fabricated titanium-gold gate on the surface of the sample in the Keck micro-fabrication facility in the clean room environment. This gate electrode replaces the tip and plays the role of the probe. This is a more standard measurement, similar to the study performed by Hampton *et al.*[56].

The measurement reveals the capacitance plateaux of the conduction band of the sample as we increase the bias voltage, i.e., the d.c. tip voltage  $V_{tip}$ . The real advantage of the measurement is the well-defined parallel-plate geometry. The area of the electrode is calculated as  $5.7 \times 10^{-7} \text{ m}^2$ . Another advantage of the measurement is that we do not need the sensor circuit to get a reasonably good capacitance signal because the large gate area leads to an intrinsically large signal. Figure 4.1 shows the resulting curve as a function of gate voltage. The data are acquired in the  $^3\text{He}$  cryostat at below 4 K. The capacitance curves are reproducible, which are collected at various spots above the sample surface. We interpret the data in the following way: For sufficiently negative gate voltage, the 2D layer below the donors is depleted completely. As no charge can tunnel vertically, the signal is simply the substrate-

to-gate capacitance. At around -1.0 V, as charge begins to enter the 2D layer; the capacitance increases, forming a step feature, as indicated. At around +0.1V, charge begins to enter a second potential well formed below the cap layer. This gives a second capacitance step feature, as indicated. The structure of the conduction band is shown in Figure 4.4.

For the voltage range displayed in Figure 4.1, the signal showed negligible phase shifts and hence can be considered as purely capacitance. The out-of-phase capacitance step height is less than the in-phase step by more than an order of magnitude for the data acquired at 20 kHz excitation frequency. This also holds for the local probe data which will be shown later. Also for both types of measurements, all voltages are plotted with respect to the effective zero voltage. This is the voltage for which no electric field terminates on the top electrode (gate or tip). It is shifted from the applied voltage by an amount equal to the contact potential,  $V_{contact}$ . For the PtIr tip used in the local probe measurements,  $V_{contact} = 0.60$  V, as determined from in situ Kelvin Probe measurements[37]. For the gated-capacitance data, the observed shift in the curves implies  $V_{contact} = 0.12$  V; this value agrees reasonably well with the reported work functions of Ti and Au, in comparison to Pt and Ir[57].

In addition to showing the accumulation of electrons in the 2D and cap layers, the gated-capacitance measurement allows us to estimate the density of ionized donors. This follows from the observation that the 2D electron system is fully formed at zero applied voltage. Of course, ionized donors introduce electric field; this in turn changes the slopes of the conduction band potential as shown in Figure 4.4. These slopes must be sufficiently steep to allow the conduction band to dip below the Fermi level at the 2D location. Solving Poissons equation with this constraint yields a density of ions equal to at least 90% of the growth Si density of  $1.25 \times 10^{16} \text{ cm}^{-2}$ . Hence, most of the Si atoms have indeed donated an electron and are ionized at zero applied potential.

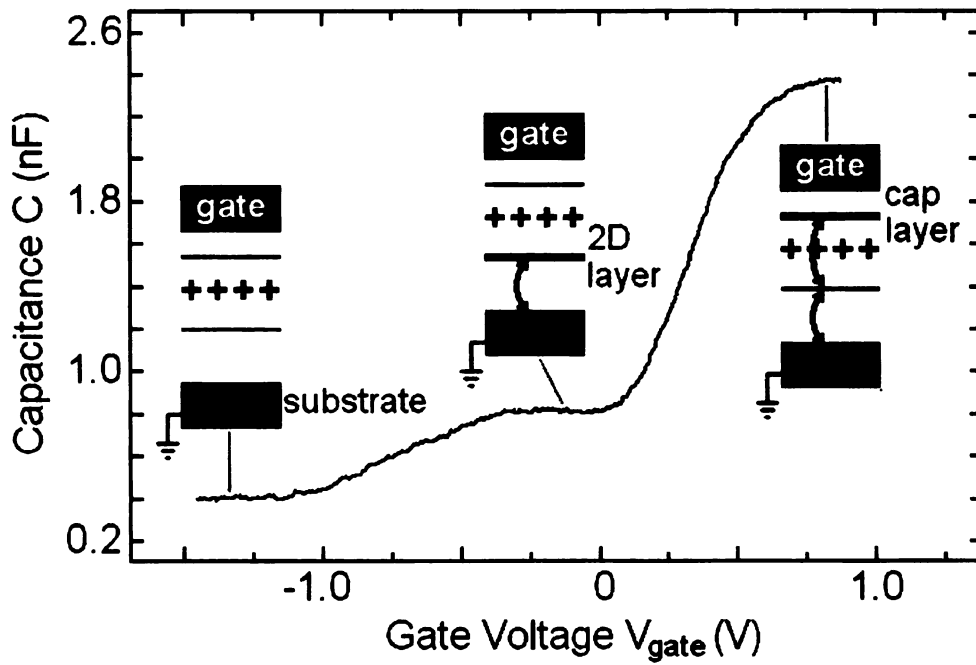


Figure 4.1: The gated capacitance measurement taken by the TiAu planar gate on the surface of the sample with an area of  $5.7 \times 10^{-7} \text{ m}^2$ . The capacitance increases with the ramping voltage forming the three plateaux. The gated measurement provides the background plateau for measurements with the localized probe.

### 4.3.2 Scanning-probe Spectroscopy Measurements

The technique is based on scanning charge accumulation imaging, which in this context can be considered as a scanned-probe version of single-electron capacitance spectroscopy (SECS), pioneered by Ashoori and coworkers[54, 58]. The method is also an extension of the scanning charge accumulation imaging[37] as explained in Chapter 3 in detail. The key component is a metallic tip with an apex of radius  $\sim 50$  nm, connected directly to our cryogenic charge sensor, which achieves a sensitivity of  $0.01 e/\sqrt{Hz}$ . As a reminder I would like to revisit how the technique works: We monitor the tip a.c. charge,  $q_{tip}$ , in response to an a.c. excitation voltage  $V_{exc}$  applied to an underlying electrode, as a function of d.c. bias voltage  $V_{tip}$ . If the quantum system below the tip can accommodate additional charge, the excitation voltage causes it to resonate between the system and the underlying electrode—giving rise to an enhanced capacitance,  $C \equiv q_{tip}/V_{exc}$ . Figure 4.2 shows the main components of the experiment, schematically.

The sample (Figure 4.3) we employed was grown by molecular beam epitaxy and is of exceptional quality, similar to the samples used in previous SECS experiments that probed lithographically defined quantum dots[54, 58]. The conduction-band profile of the sample is shown in Figure 4.4. A degenerately doped substrate acts as a metallic electrode. Above this is a two-dimensional electron layer. This represents an ideal base electrode from which charge can enter the higher layers in the sample. It is separated from the metallic substrate by a superlattice tunneling barrier; the tunneling rate into the 2D layer is an order of magnitude greater than the 20 kHz excitation frequency employed for all the measurements shown here. Hence for this experiment, the 2D layer can be regarded as being in ohmic contact with the substrate. Positioned 20nm above the 2D conductor is the donor layer, which consists of silicon atoms confined to a single monolayer with respect to the  $z$  direction, but randomly positioned with respect to the  $x$ - $y$  direction with an average density of  $1.25 \times 10^{16}$

cm<sup>2</sup>. Charge may also become trapped in the cap layer, which is 30 nm above the donors.

Each data run begins by scanning the tip in both tunneling and capacitance modes to check that the surface was sufficiently clean and free of major electronic defects[43]. To acquire the capacitance curves, the tip is positioned about 1 nm from the GaAs surface and held it at the fixed location while sweeping the tip voltage. To compensate for vibrations and drift effects, several curves were averaged together to achieve an acceptable signal-to-noise ratio. The resulting local capacitance curves consistently showed peaks in the vicinity of  $V_{tip}=0.5$  V, which were not present in the gated measurement.

To display the characteristic structure, Figure 4.6 shows the average of three measurements (black dots) that exhibited the lowest noise, acquired at different locations. Three broad peaks, labeled A, B, and C, are clearly resolved consistently at different tip locations. For comparison, these data are superposed with the gated-capacitance curve (solid blue). Note that the two data sets have different voltage scales. This is expected given that the geometry-dependent alpha parameter namely lever-arm factor should be different for the two measurements. The corresponding alpha parameters can be evaluated for the gate electrode measurement and localized probe measurement with respect to the equations below, respectively;

$$\alpha_{tip} = \frac{C_{tip}}{C_{tip} + C_{2D}} \quad (4.2)$$

$$\alpha_{gate} = \frac{C_{gate}}{C_{gate} + C_{2D}}, \quad (4.3)$$

where  $C_{tip}$  is the tip-to-donor layer capacitance,  $C_{gate}$  is the gate-to-dopant layer capacitance, and  $C_{2D}$  is the 2DEG-to-donor layer capacitance. Comparison of the gated and scanned-probe measurements gives us the capacitance of the tip is smaller than the capacitance of the gate, since there is a vacuum gap between the tip and

sample. For the gated measurement, the parallel-plate geometry and sample growth parameters give a proportionality constant of  $1/4.0$  with respect to the donor layer. For the local probe measurements, the relative scale factor between the two voltage ranges used in Figure 4.6 implies  $\alpha_{tip} = 1/10.8$ . This is a reasonable value consistent with the expected tip-sample mutual capacitance[10, 9]. Clearly, the broad peaks appear only in the local measurements; to help explain their physical origin, we first examine fine-structure peaks that also appear in the data, which is shown in the inset of Figure 4.6.

Figure 4.7 shows the capacitance variation versus tip voltage curve over the voltage range shown in the circular box in Figure 4.6. For these curves the background capacitance was subtracted away using a bridge circuit explained in chapter 3. Shown in this figure is the comparison of data acquired at a single location (not the average of three locations as in Figure 4.6 ) with two different excitation voltage amplitudes, 16 mV(rms) and 3.8 mV(rms). The coarse measurement (gray) is shifted vertically for clarity. The fine measurement (black) shows a series of small peaks. To gauge the reproducibility of the fine-structure peaks, the inset shows two measurements acquired under identical conditions but with a time delay of 9 hours. We see the structure is reproducible partially, where the asterisks mark voltages for which peaks are missing or shifted in position. The observation that some peaks reproduce with almost identical shape and position highlights the level of stability the system achieves over several hours. The missing and shifted peaks likely reflect long time scale variations due to a small percentage of electrons trapped in deep metastable states such as DX centers[23].

Figure 4.8 (top) shows three curves acquired at the voltage marked by the arrow in Figure 4.7, with their average shown on the right. This peak was selected as it is relatively well isolated from neighboring peaks. For this plot we have converted the vertical scale to show the rms charge induced on the tip in units of the electron

charge  $e$ . Figure 4.8 (bottom) shows isolated peaks for both the coarse (blue) and fine (red) excitation amplitudes. For the coarse data, the peak was especially well isolated. The data are compared to two model curves that show the expected semi-elliptical peak shapes for single-electron tunneling for the coarse and fine measurement parameters[55]. With regard to the widths of the peaks, in the low-temperature limit, the widths of the model curves are set by the excitation amplitudes; we see that the single-electron model agrees reasonably well with the measurements. With regard to the vertical scale, if all the electric field lines were captured by the tip, the magnitude of model single-electron peaks would be  $0.99e$  and  $0.92e$ . However, to achieve a good fit, the heights of the model curves are scaled by 0.075. This peak height is roughly consistent with expected captured electric flux for single-electron charging within the donor layer, for which the scale factor should be approximately  $\alpha_{tip} = 1/10.8 = 0.093$  [55, 10]. Hence we conclude that the isolated fine-structure peaks likely reflect individual electrons entering the donor layer below the tip.

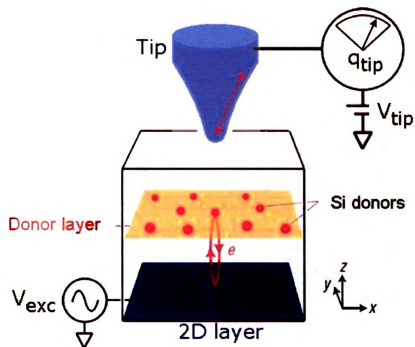


Figure 4.2: A schematic diagram of the key layers in the gallium arsenide [001] heterostructure sample and the measurement technique. An excitation voltage can cause charge to resonate between the Si donor layer and a two-dimensional (2D) layer, which represents an ideal base electrode. This results in image charge appearing on a sharp conducting PtIr tip. A cryogenic transistor attached directly to the tip is used to measure the charging. The donor layer consists of silicon atoms confined to a plane with respect to the  $z$  direction, but randomly positioned with respect to the  $xy$  direction with an average density of  $1.25 \times 10^{16} \text{ m}^{-2}$ . At zero applied voltage, at least 90% of the Si atoms are ionized (that is, have donated an electron). Magnetocapacitance measurements conducted in the kilohertz frequency range indicate negligible donor-layer conductivity for identical samples cut from the same wafer.



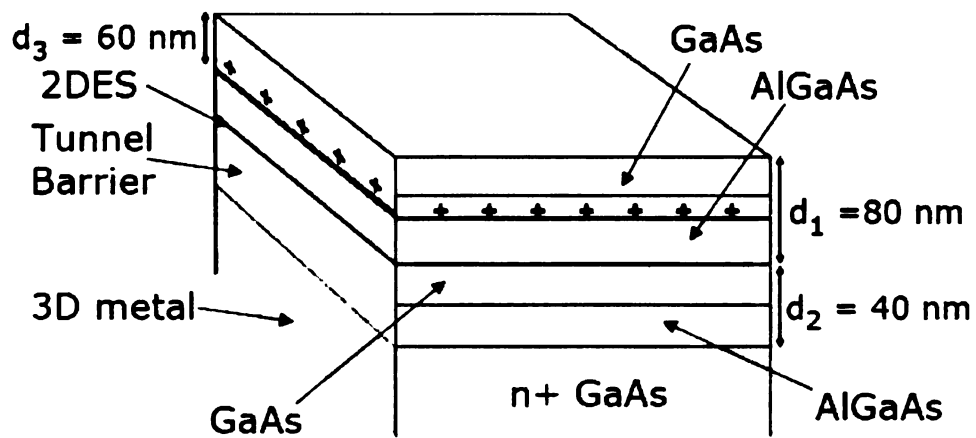


Figure 4.3: A schematic diagram of the bottom-up layers in the gallium arsenide [001] heterostructure sample. The sample is fabricated by molecular beam epitaxy (MBE), which is an exceptional sample growing technique described in Chapter 2. The degenerately n-doped 3D substrate has the tunnel barrier grown upon it. The GaAs/AlGaAs heterojunction is shown on top of it, where the 2DEG forms. The delta-doped layer is shown with the plus signs, which represents the ionized Si donors. At the very top there is a GaAs cap layer.

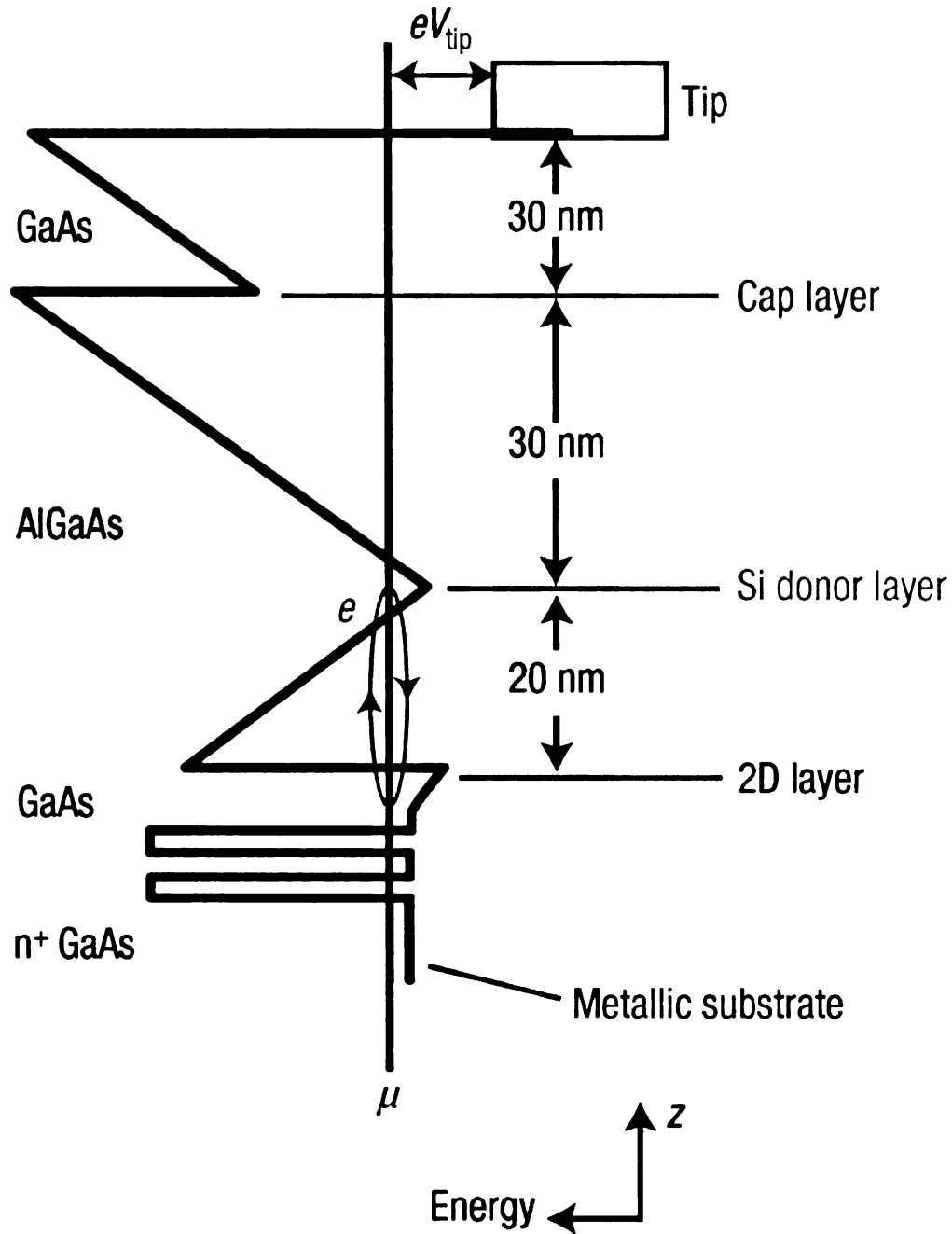


Figure 4.4: A more detailed conduction-band diagram of the sample. The excitation voltage is applied to a degenerately doped substrate that acts as a metallic electrode. Above this is the 2D electron layer. It is separated from the metallic substrate by a superlattice tunneling barrier; the tunneling rate into the 2D layer is an order of magnitude greater than the 20 kHz excitation frequency we used. Hence for this experiment, the 2D layer can be regarded as being in ohmic contact with the substrate.

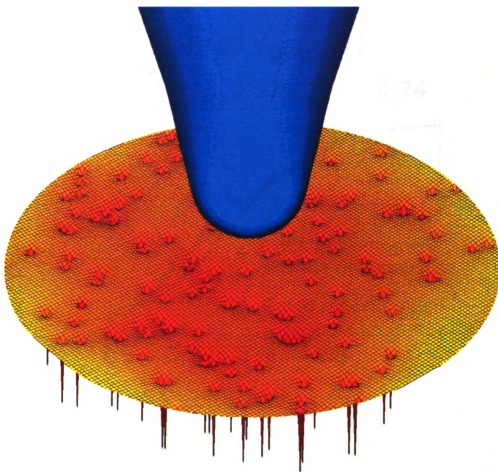


Figure 4.5: A schematic diagram of the area probed by the technique, with Si donors represented as hydrogen-like potentials. For our experimental geometry, the radius of the area over which we are probing is set mostly by the separation between the tip and the donor layer, which is approximately 60 nm [9][10]. Within this area, on average we expect 140 donors. A schematic diagram of the probe is also represented in the figure.

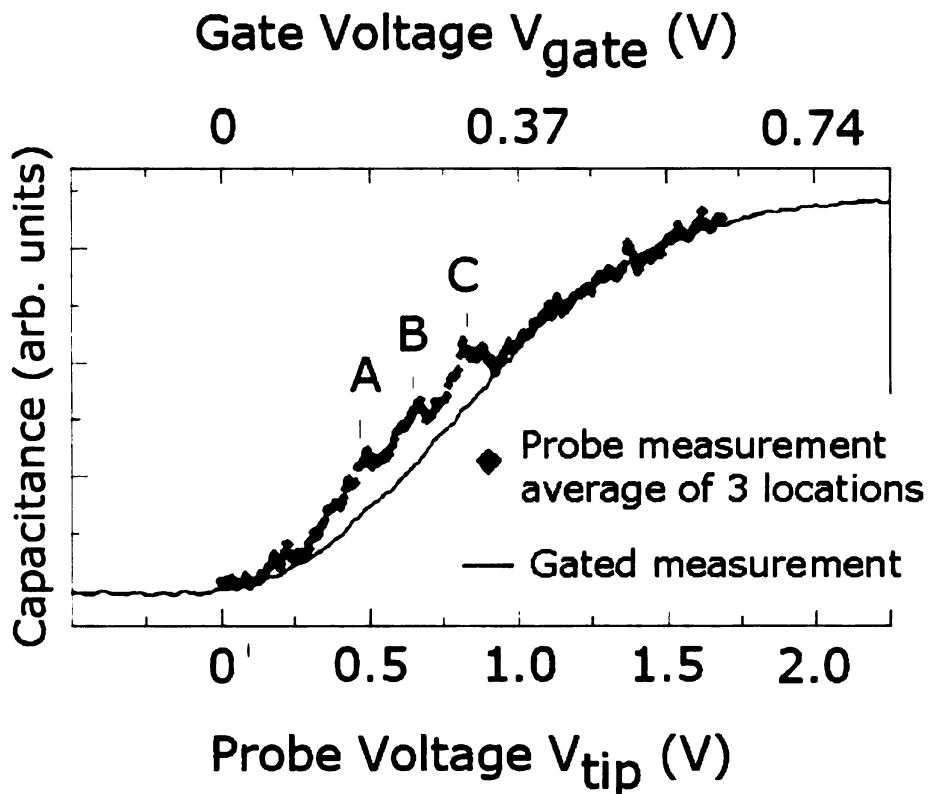


Figure 4.6: Capacitance measured with our local probe superposed with the gated measurement. The local measurement is the average of measurements acquired at three locations. Three broad peaks labeled A,B, and C were consistently observed. For both the local and gated curves, the voltage scales are plotted relative to the effective zero voltage, compensating for the contact potentials between the materials. The excitation voltage amplitude was  $V_{exc}=15$  mV(rms) for both curves. The vertical scale of the probe measurement is exaggerated greatly relative to the gated measurement.

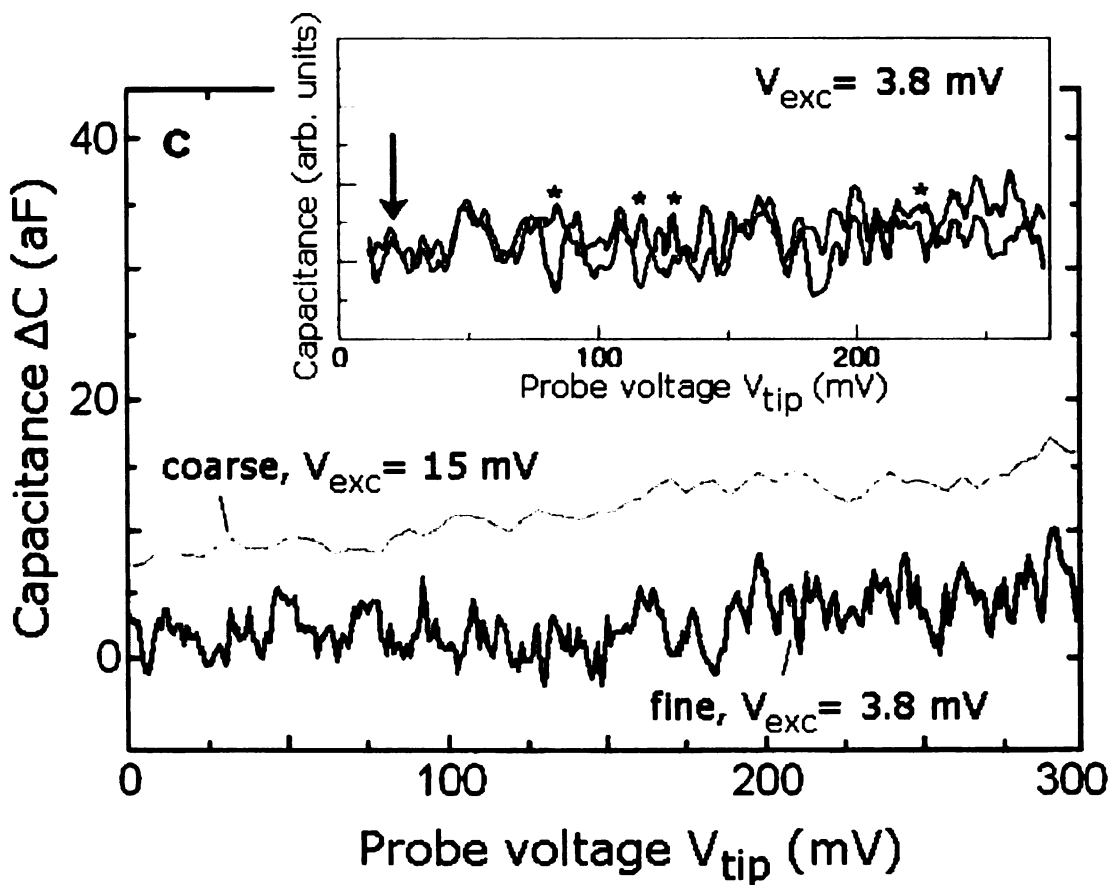


Figure 4.7: Capacitance variation DC versus tip voltage curve over the voltage range shown in the red circle in Figure 4.6. These data were acquired at a single location but with two different excitation voltage amplitudes: “coarse”, 15.0 mV rms and “fine”, 3.8 mV rms. The inset shows two  $V_{exc} = 3.8$  mV measurements acquired under identical conditions but with a time delay of 9 hours.

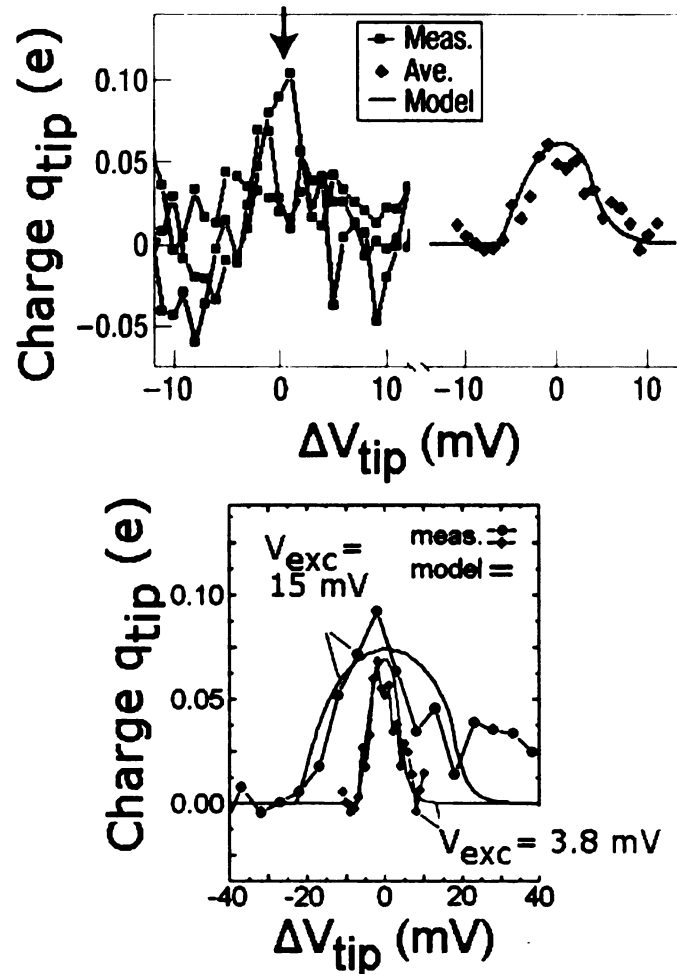


Figure 4.8: (top) Three curves acquired at the voltage marked by the arrow in Figure 4.7 (same location) with an excitation voltage of 3.8 mV. The vertical scale has been converted to charge units and labeled as  $\Delta q_{tip}$  to indicate that we have subtracted away the background charge. Below we plot the average of the three curves. The measurement is compared to a model curve that shows the semielliptical peak shape expected for single-electron tunneling [13,16]. The width of the model curve is set by the 3.8mV excitation amplitude; the asymmetry is caused by the lock-in amplifiers output filter, which is included in the model. (bottom) Comparison of the peak shapes for isolated peaks for both the coarse and fine excitation amplitudes. The average data of (top) is re-plotted (black) along with an especially well-isolated peak observed at a different location and with the coarse excitation voltage of 15.0mV (gray). The data are compared to two model curves that show the expected peak shapes for single-electron tunneling for the coarse and fine measurement parameters.

## 4.4 Donor Molecule Formation-Results of CI Method

### 4.4.1 Introduction

In the previous section, I introduced the gated capacitance measurement, local-probe capacitance curve, and the fine structure analysis, i.e., the single electron-addition spectrum in the donor layer. In this section, I will review the physical significance of the broad peaks in the addition spectrum in Figure 4.6 and introduce the details of the donor molecule model. The comparison between the model and the capacitance data will also be presented.

### 4.4.2 Analysis of Broad Peaks

Given that the fine-structure peaks likely mark electrons entering the donor layer, a natural explanation for the broader peaks (A,B, and C) is that they are formed by clusters of several electrons entering at nearly the same energy. If we convert capacitance to charge units, we find that each peak corresponds to roughly 15 electrons entering the donor system, as described in more detail below. The reason such peaks were not seen in Figure 4.6 and previous capacitance studies, such as Ref. [56], is probably the larger area probed in gated measurements. Micron-size areas are more likely to contain at least one severe defect or impurity that allows charge to penetrate the material and effectively short out interactions with the donor system[51].

What physics could give rise to the broad resonances observed in the local measurements? It is possible that dense groupings of the donors result in electron puddles acting as small quantum dots[59]. In that scenario, an ensemble of puddles that have nearly the same addition energy spectra could explain the peaks. However, given that the positions of donors should be random, it seems unlikely that 15 such puddles would form within a radius of only 60 nm with sufficiently similar characteristics. Considering the opposite limit, a candidate for identical quantum objects is single

silicon donors. However, isolated Si donors in GaAs and AlGaAs can bind exactly two electrons [23][4], analogous to an isolated hydrogen ion in free space, which can also accommodate two electrons and form the negative  $H^-$  state. Hence, neglecting for the moment the interaction with the tip, an ensemble of isolated donors would yield only two broad peaks in the capacitance spectrum, whereas we observe three. Pairs of closely spaced silicon donors represent another candidate quantum system, which we will refer to as two-donor molecules (2DMs).

With regard to the gated-capacitance measurement, Figure 4.1 clearly does not exhibit any remarkable features representing the electrons entering the donor layer on the region between 2D plateau and cap-layer. We believe this is due to the micron-size area of the gate electrode, which is much greater than the area of the CAI local probe. Essentially, there is a high probability of the defects and impurities below the gate electrode. In contrast, the gated capacitance measurement provides a good reference as a background curve giving rise to the main plateaux that maps out the layers and quantum wells in the heterostructure.

### 4.4.3 Effective Mass Approximation

I described the impurities and dopant systems in semiconductors in chapter 1. One of the common features of impurity systems is that we can approximate an ionized donor acting as a hydrogen-like atom. The question is how to determine the wave functions and energy eigenvalues of the impurity atom by considering the significance of the dielectric screening and energy band structure of the host crystal. For simplicity, I would like emphasize certain aspects of the problem. The strong screening of the high dielectric constant ( $\kappa=12.1$  for GaAs) of a typical semiconductor crystal reduces the potential of the impurity nucleus significantly. This weak impurity potential varies over a large distance compared to the lattice constant. In the 1950s Luttinger and Kohn systematically developed a theory regarding these simplifications



self consistently. This theory is called “effective mass theory” of impurity states or the “Luttinger-Kohn approximation”. Here, I will review the theory briefly starting with the Schrödinger equation satisfied by the impurity wave function  $\psi_i(\mathbf{r})$ ,

$$\left[ \frac{\hbar^2}{2m} \nabla^2 + V_i(\mathbf{r}) + V_p(\mathbf{r}) \right] \psi_i(\mathbf{r}) = E_i(\mathbf{r}) \psi_i(\mathbf{r}), \quad (4.4)$$

where  $V_i(\mathbf{r})$  is the impurity potential,  $V_p(\mathbf{r})$  is the periodic potential of the crystal, and  $E_i$  is the energy eigenvalue. For a donor impurities Luttinger and Kohn expanded the electronic wavefunctions in terms of the functions instead of Bloch functions  $\psi_{nk}(\mathbf{r})$ ,

$$\chi_{nk}(\mathbf{r}) = e^{i\mathbf{k}\cdot\mathbf{r}} u_{n0}(\mathbf{r}) \quad (4.5)$$

which are called Luttinger-Kohn functions. By substituting the complete set of expanded functions

$$\psi_i(\mathbf{r}) = \sum_n \sum_k A_{nk} \chi_{nk}(\mathbf{r}) \quad (4.6)$$

in the Schrödinger equation, Eq. (4.4) and making use of the simplifications mentioned above they were able to show that impurity wave functions can be expressed approximately as

$$\psi_i(\mathbf{r}) \simeq F_c(\mathbf{r}) u_{n0}(\mathbf{r}). \quad (4.7)$$

The  $F_c(\mathbf{r})$  is known as effective mass wave functions or envelope function (Fig. 4.10), where  $c$  is the conduction band label. It satisfies the effective mass equation which is the final reduced form of the Schrödinger equation (Eq. 4.4). It is an equation for the envelope function alone, containing an “effective Hamiltonian”,

$$\{E_c(-i\nabla) + V_i(\mathbf{r})\} F_c(\mathbf{r}) = E_{ci} F_c(\mathbf{r}), \quad (4.8)$$

where  $E_C(-i\nabla)$  is obtained by replacing  $\mathbf{k}$  in the band energy  $E_C(\mathbf{k})$  by the operator  $-i\nabla$ . The effective Hamiltonian would still be an extremely complicated if the full band structure is considered for  $E_C(\mathbf{k})$ . However, the wave function is assumed to be drawn from only a small region of  $\mathbf{k}$ -space and  $E_C(\mathbf{k})$  can be simplified to be consistent with this.

The impurity potential can be approximated by the Coulomb potential

$$V(r) = -\frac{e^2}{\kappa r}, \quad (4.9)$$

where  $e$  is the charge of the ionized impurity and  $\kappa$  is the static dielectric constant of the semiconductor. In Figure (4.9) the representative form of a dopant potential is shown. III-V semiconductors such as GaAs have a single conduction band minimum at  $\mathbf{k}=0$ . The conduction band to a good approximation is spherical and parabolic. The energy of a spherical parabolic band with effective mass  $m^*$  can be written as

$$E_k = \frac{\hbar^2 k^2}{2m^*} \quad (4.10)$$

The effective mass equation then yields

$$\left[ -\frac{\hbar^2 \nabla^2}{2m^*} - \frac{e^2}{\kappa r} \right] F_c(\mathbf{r}) = E_{ci} F_c(\mathbf{r}) \quad (4.11)$$

which is the Schrödinger equation for an hydrogen-like atom. The solution for the ground state wave function of a hydrogen-like potential gives an exponentially decaying dependence in 3D spatial coordinates,

$$\psi(\mathbf{r}) = (\pi a_B^3)^{-\frac{1}{2}} \exp\left(-\frac{\mathbf{r}}{a_B}\right) \quad (4.12)$$

The eigenfunctions are characterized by an effective Bohr radius of

$$a_B^* = \frac{\hbar^2 \kappa}{m^* e^2} \quad (4.13)$$

The binding energy of the impurity ground state is the effective Rydberg ( $Ry^*$ ) given by

$$R^* = \frac{\hbar^2}{2m^* a_B^{*2}} = \frac{m^* e^4}{2\hbar^2 \kappa^2} \quad (4.14)$$

The energy eigenvalues are those of a hydrogen-like atom given by

$$E_{n_H} = -\frac{Ry^*}{n_H^2} \quad (4.15)$$

where  $n_H$  is the principle quantum number with the integer values. A schematic representation of the parabolic band energy spectrum is given in the Fig. (4.11). This picture is applicable to donor impurities in GaAs. The donor level resides just below the conduction band edge and for an acceptor the ground state lies above the valence band edge. These impurity levels residing close to the corresponding band edges are called “shallow levels”. The Bohr radius ( $a_B$ ) and effective Rydberg energy ( $Ry^*$ ) for a donor impurity in GaAs with  $m^*=0.07m_e$  and  $\kappa = 12$  correspond to 9 nm and 6.6 meV, respectively. This demonstrates that the Bohr radius is more than a factor of ten greater than the lattice constant (0.56 nm) of GaAs and the ionization energy of the impurity electron is less than 1% of the energy gap (1.52 eV) of GaAs[60].

The excited state wave functions are more diffuse than for the ground state and the excited state wave functions have vanishing amplitude at the donor nucleus. Therefore, the effective mass approximation works for the excited states better than ground state of the ionized impurity electron[61].

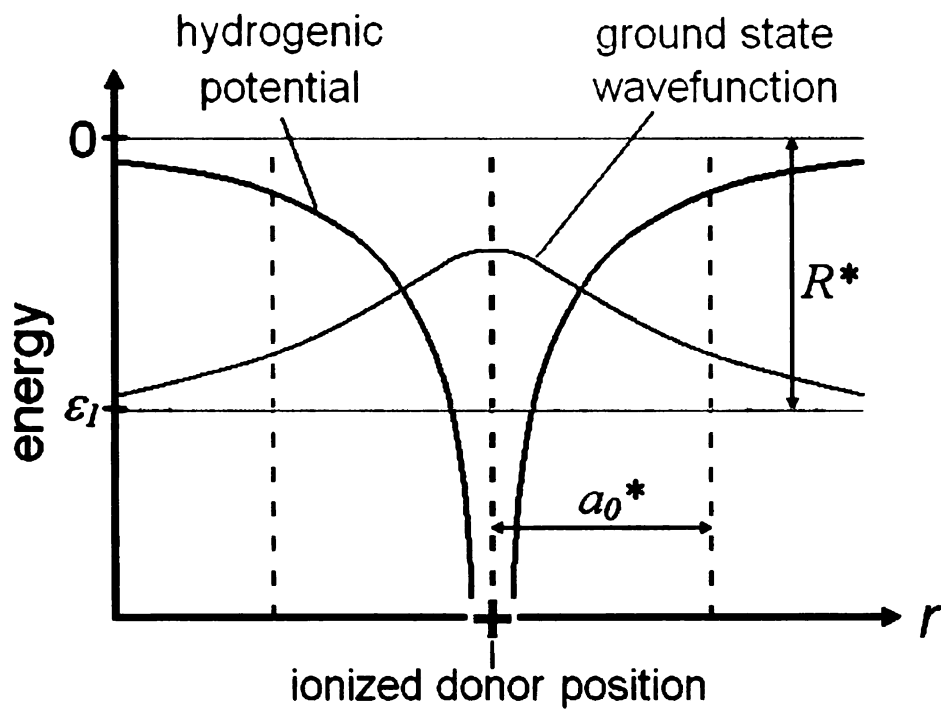


Figure 4.9: A representative picture of the hydrogen-like dopant atom is shown. Ground state wave function and the potential energy are shown. Energy level of the ground state is represented in Rydberg energy,  $R^*$ . The effective Bohr radius,  $a_0^*$  for the ionized donor in the crystal is also depicted in the figure [11].

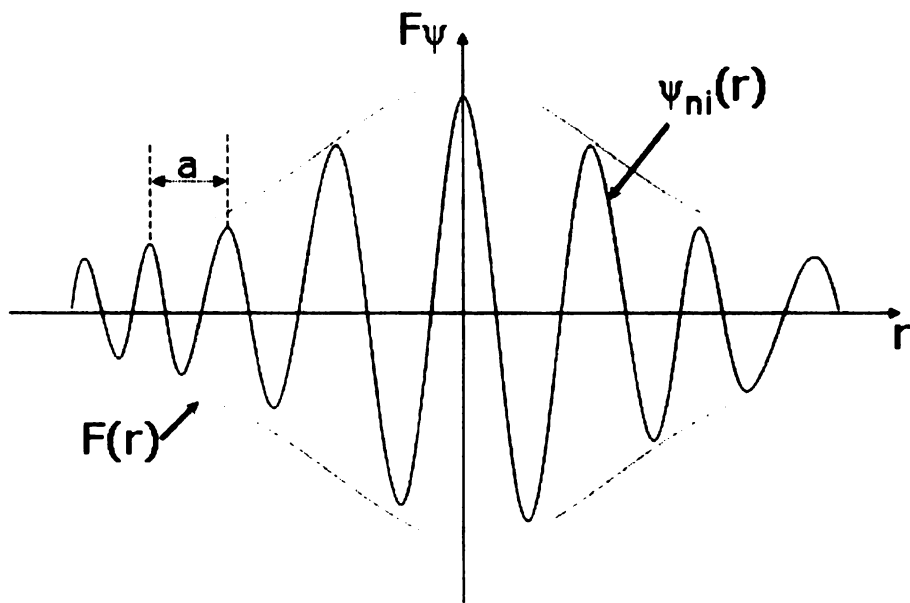


Figure 4.10: Simple representation of effective mass wave function or envelope function  $F_C(\mathbf{r})$  and the impurity wave function  $\psi_i(\mathbf{r})$ , where  $a$  is the lattice constant.

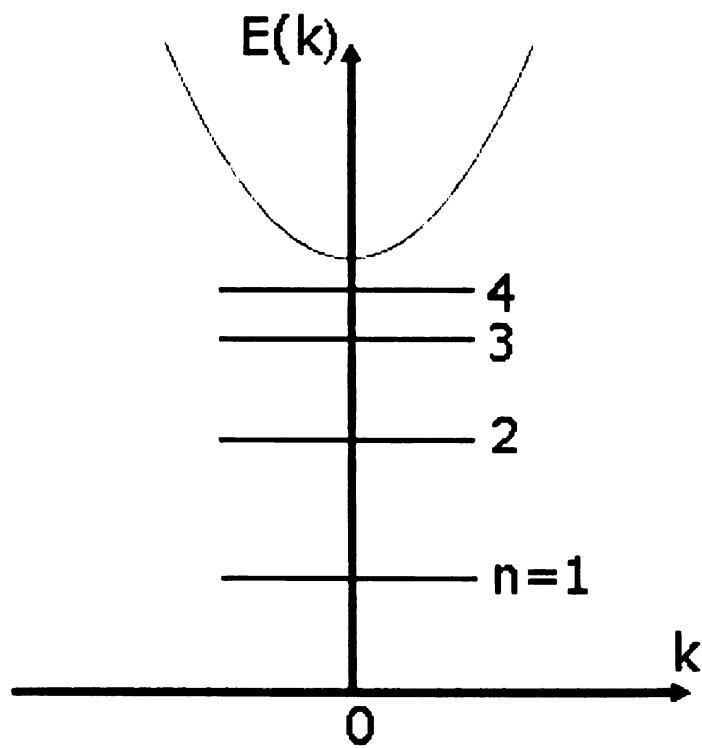


Figure 4.11: Hydrogen-like energy spectrum of a shallow donor impurity.

#### 4.4.4 Configuration-Interaction Results

To explore the addition spectrum of 2DMs, we have calculated the electronic energies of two silicon donors separated by a distance  $d$ , but otherwise isolated. The calculations were performed using the configuration-interaction method in the effective-mass theory. In this approximation, a donor is regarded as a hydrogen-like atom with an effective Bohr radius  $a_0^*$  and effective Rydberg energy  $Ry^*$  given in equations 4.13 and 4.15. In our system, Si donors reside in  $\text{Al}_{0.3}\text{Ga}_{0.7}\text{As}$ , for which  $a_0^* = 7.3$  nm and  $Ry^* = 8.1$  meV [62]. The results for the first four electrons are plotted in Figure 4.13. Interestingly,  $E(3)$  is lower than  $E(2)$  for large separations, but the two lines cross at  $\sim a_0^*$ . This means that at large separations, the molecule holds three electrons, similar to the  $H^-$  state; but for small separations only two electrons can be accommodated. The intuitive picture is that the neutral system can polarize and weakly bind the third electron. But this is prohibited for small separations for which the direct Coulomb repulsion dominates. This effect has been the subject of previous studies. We see that  $E(4)$  is always higher energy than  $E(3)$ , hence the fourth electron is never bound.

To compare the calculations to our measurements, it is instructive to gauge the likelihood of finding 2DMs in our system. Figure 4.14 shows the statistical nearest-neighbor distances for donors dispersed randomly within a 2D layer. Nearest-neighbor distances essentially follow Poissonian distributions [63]; selecting a donor at random, it can be shown that the probability to find its  $m^{\text{th}}$  nearest neighbor between a distance  $R$  and  $R+dR$ ,  $f(\rho)dR$  is

$$f(\rho)dR = \frac{(\pi R^2 \rho)^{m-1}}{(m-1)!} 2\pi R \rho \exp(-\pi R^2 \rho) dR \quad (4.16)$$

where  $\rho$  is the 2D density. For the curves shown in Figure 4.14, we used the nominal donor density of our sample,  $\rho = 1.25 \times 10^{16} \text{ cm}^{-2}$ . With regard to 2DMs, we see that

on average the first nearest neighbor will be less than an  $a_0^*$  away. Hence we expect that many 2DMs will be present in the experiment. However, as shown in Figure 4.13, the configuration-interaction calculations predict only two bound electrons for these small separations; this is inconsistent with our observation of three peaks. With regard to isolated donors, Figure 4.14 shows that only a small fraction of the donors will have no neighbors within one effective Bohr radius. Hence it is unlikely that isolated donors will contribute significantly to the addition spectrum.

Thus far we have neglected the perturbative influence of the tip. With respect to the donor-layer plane, the positive tip voltage gives a curved background potential that tends to increase the confinement. We can therefore improve our theoretical model by including an image charge in the calculations that approximates this potential. The solid curve of Figure 4.15 (Top) shows the expected confinement potential for  $V_{tip} = 0.45$  V, which is the potential in the vicinity of peak A; the dashed curve is the image-charge approximation incorporated into the configuration-interaction calculations. We see the image-charge approximation is somewhat weaker than the expected confinement; moreover we take this potential as fixed, even though the tip voltage varies during the measurement. Hence, this is a very rough approximation of the tip's influence, necessitated by the computationally intensive nature of the calculations. The decision to err on the side of weak confinement is justified by the fact that the confinement effect weakens for donors not directly below the tip. Figure 4.15 (Bottom) shows the corresponding 2DM calculations for the electronic energies for the first four electrons. In this case we see that  $E(3)$  is lower than  $E(2)$  even for small separations. Hence this spectrum shows that the third electron will always be bound. Moreover, the fourth electron is also bound, but very weakly. All subsequent electrons are unbound in this calculation.



#### 4.4.5 Influence of non-nearest neighbors

In addition to interactions with the tip and with nearest neighbor donors, a complete model suitable to directly simulate the measurements must also include the effects of the non-nearest neighbors. We can gain insight into the physics of the system by comparing rigorous calculations of the binding energy of the first electron  $E(1)$  to a very simple Coulomb-shift approach. The black curves of Figure 4.12 compare the rigorous binding energy of the two-atom molecule (solid) to a curve derived by shifting the binding energy of an isolated H atom by the Coulomb energy of a charged neighbor at a distance  $d$ :  $e/4\pi\epsilon_0d$  (dashed). We see that for distances greater than  $a_0$ , the two agree to within a precision of  $\sim 15\%$ . The gray curves make a similar comparison for a three atom equilateral triangle, reproduced from Ref. [12], and an isolated H atom Coulomb shifted by two neighbors at a distance  $d$ . We see that this simple-minded approach does a surprisingly good job of predicting the addition energy for the first electron. However, as the unshifted energies are based on an isolated H atom, it is too simplistic to generate the full addition spectra for two-atom molecules.

Motivated by these ideas, we have developed a model that extends the 2DM configuration-interaction calculations to account for non-nearest neighbors. Figure 4.16 schematically introduces the method, which follows essentially a Monte Carlo approach [51, 63]. We consider a 2D area of  $\pi(60 \text{ nm})^2$  with 140 donors, labeled  $i$  in the figure. We position the donors randomly within the area and group them into 70 nearest-neighbor pairs, labeled  $k$ . Each pair has assigned to it an addition spectrum  $\epsilon_{1,2,3,4}^k$  based on the separation of the two atoms as given by Figure 4.17. To simulate the capacitance-versus voltage curve, we consider the Coulomb shift  $U_i^k$  of every quantum level due to all the other donors. This leads to an ensemble of 2DM energy levels, resulting in broad peaks similar to the measurements. The width of the peaks is  $\sim 1 Ry^*$ , arising mostly from the variation in Coulomb shifts as each 2DM

has a different configuration of neighbors [51, 55].

To make the model realistic, we consider that the ionization of the system changes throughout the measurement. For example, for the first electron to enter the area, we assume all the donors are ionized. Hence we calculate the Coulomb shifts for each pair  $k \sum_i U_i^k$  using a charge of  $+e$  for all donors. In this case, the pair that has the lowest energy  $\epsilon_1^k + \sum_i U_i^k$  receives the electron, filling its first state and thus contributing to the capacitance at this energy. For all subsequent electron additions into other pairs, we must consider that this particular pair no longer has two fully ionized atoms. In other words, for the second electron, which would likely enter some other pair, the Coulomb shifts will be slightly reduced due to the previous charge that has already entered the system and partially neutralized one pair of atoms. To account for this effect in a straightforward way, we assume perfect screening: every time an electron enters a 2DM, we add  $-e/2$  to each atom of the pair. The model also includes the screening effect of the nearby 2D layer in our sample by using appropriately positioned image charges. Our routine calculates capacitance curves in this way, using the effective Rydberg as the energy scale. To generate smooth data that represents the average capacitance curve, we perform the calculation for hundreds of random ensembles and average the results together.

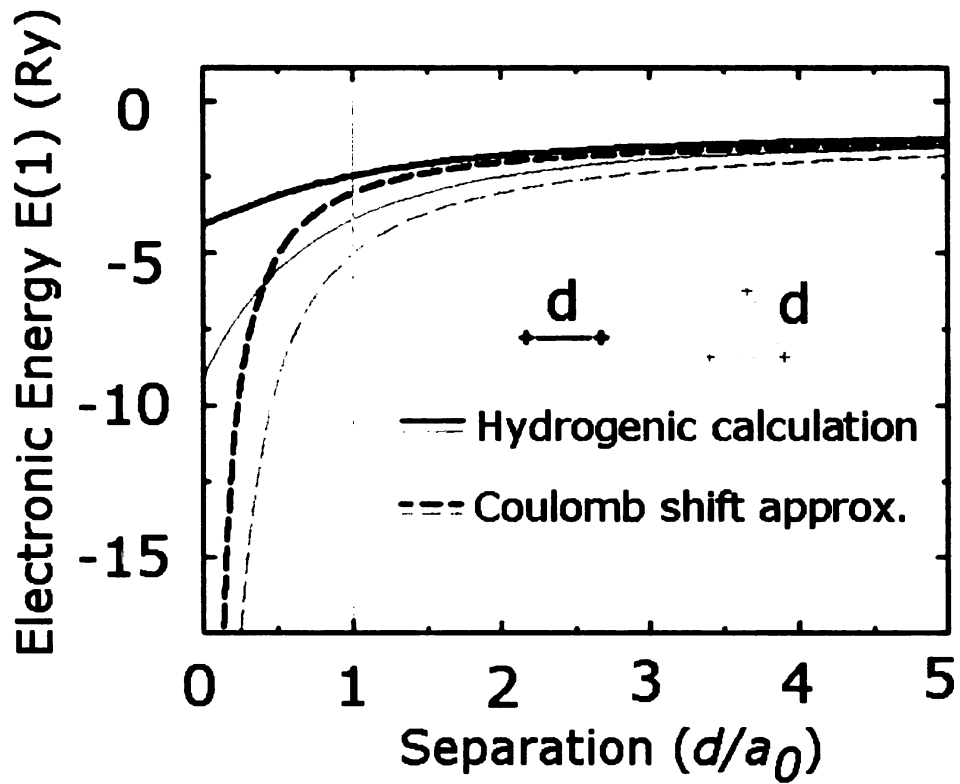


Figure 4.12: A comparison between a rigorous calculation of the binding energy of the first electron (solid) and a simple Coulomb-shift approximation (dashed). The black curves correspond to two donors and the gray curves correspond to three. The solid gray curve is reproduced from Ref [12].

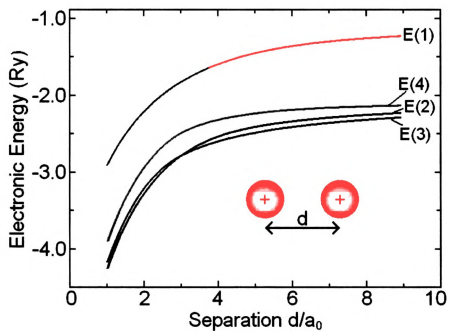


Figure 4.13: Configuration-interaction calculation of the electronic energies of two donors separated by a distance  $d$ , but otherwise isolated, as shown in the inset. At small separations, the model predicts two bound electrons for each donor molecule.

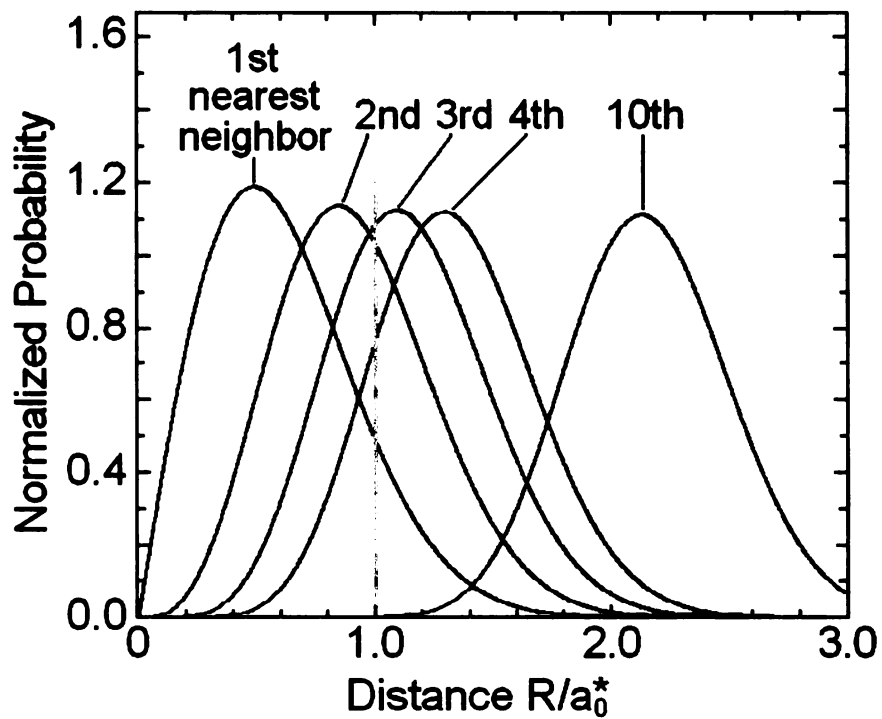


Figure 4.14: Statistical nearest-neighbor distances for donors in our system, calculated using the nominal growth density of donors in our sample. For comparison to theory, the distances are given with respect to the effective Bohr radius.

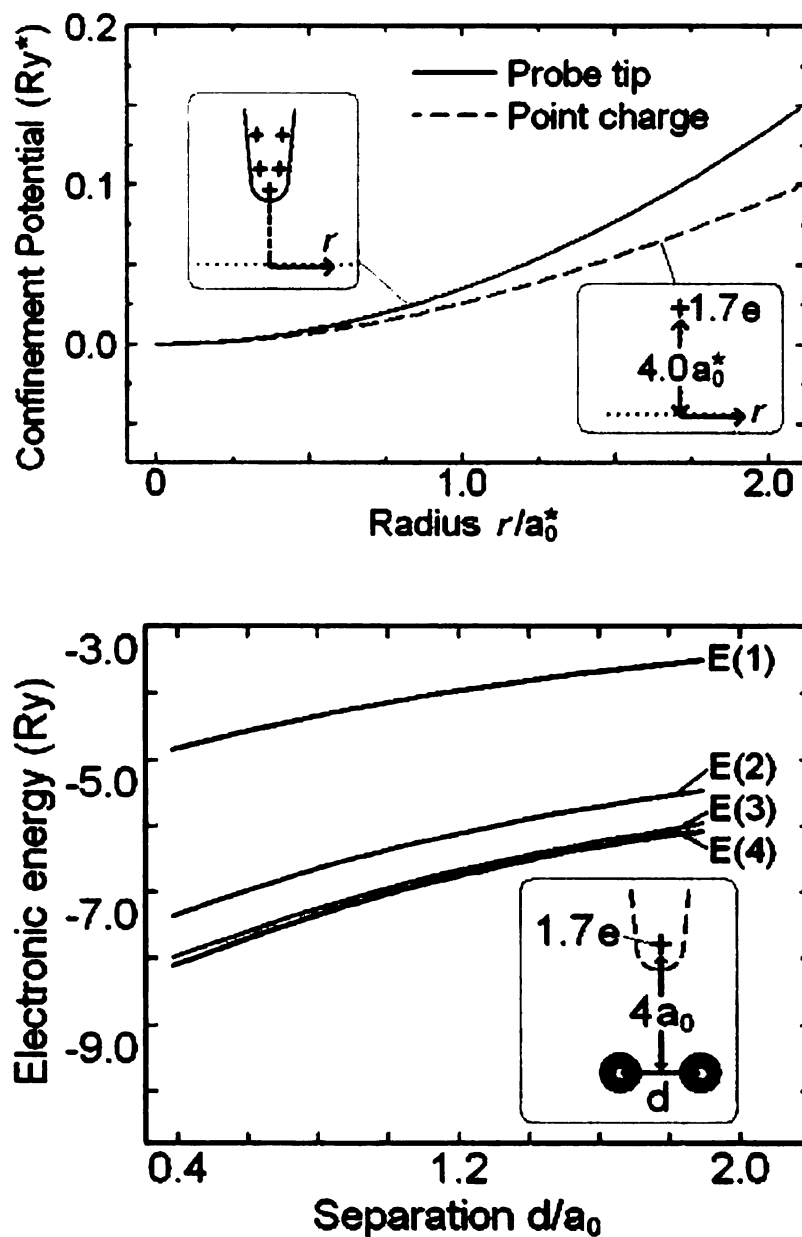


Figure 4.15: (Top)(Solid) calculated tip confinement potential in the donor layer [11,16]. (Dashed) image-charge approximation incorporated into the configuration-interaction calculations. A point charge of  $1.7e$  was employed at a distance of  $4a_0$ , as indicated in the inset. (Bottom) Revised configuration-interaction calculations including the rough approximation for the tip potential. This revised model predicts four bound electrons for each donor molecule—even for separations less than  $a_0$ .

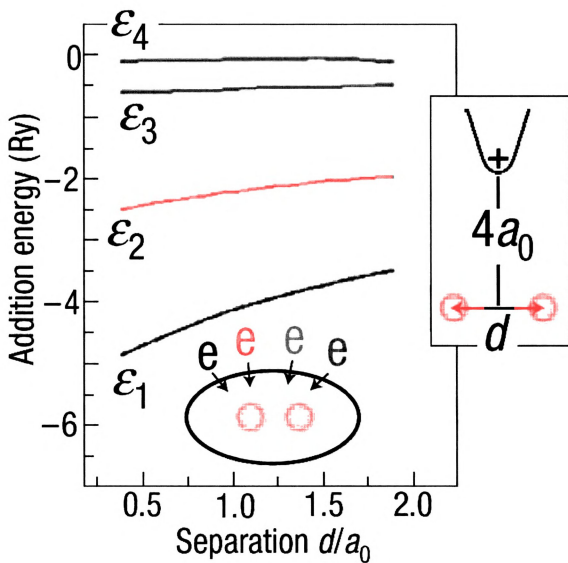


Figure 4.16: Configuration-interaction calculations of the 2DM addition energies for all bound electrons as a function of separation of the two ions  $d$ . (Inset) The calculations include an image charge to approximate the potential applied by the tip.

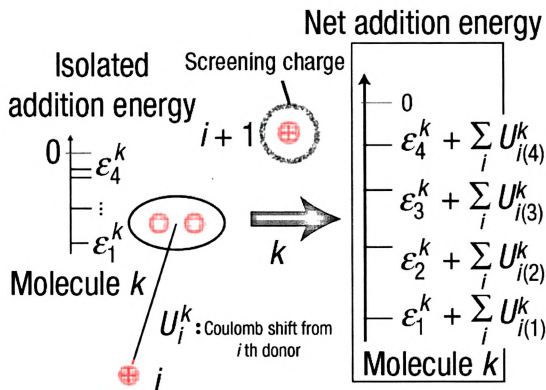


Figure 4.17: Schematic representation of the full modeling procedure. We start from a random ensemble of donors and group them into nearest-neighbor pairs to form molecules  $k$ . The addition energies shown on the left are used to assign the isolated addition energy of each molecule,  $\epsilon_1^k, \epsilon_2^k$ , and so on. Last, the model includes the Coulomb energy shift from all non-nearest neighbors; we account for the fact that this shift will be different for successive electrons owing to changes in the screening charge of non-nearest-neighbor donors.



#### 4.4.6 Comparing the calculation and measurement

Figure 4.18 shows a representative measured capacitance curve and curves calculated with the full 2DM model. The measured curve was acquired at a single location; similarly, the modeled curves are two examples of individual random configurations of dopants within the simulated area. Figure 4.19 compares a measured curve which is the average of three locations with a model curve obtained by averaging over many random configurations of donors. Understanding the detailed shape of each broad peak that results from this calculation is subtle, stemming from the fact that the ionization of the system changes during the measurement; that is, the donors become neutralized as charge is added to the layer. The modeling shows that the resulting peak width is roughly  $1 Ry^*$ . To directly compare measurement with theory, the background step feature has been subtracted from the measured data, which are shown in units of effective Rydbergs and shifted horizontally so that peak C is at zero. This is consistent with peak C lying near zero  $Ry^*$ , the energy above which the electrons are unbound. No other free parameters were used in the comparison. We see that the charge magnitude and relative energy spacing of the model peaks are in good agreement with the measurements, with peaks A and B corresponding to the average addition energies of the first and second electron  $\epsilon_{1,2}$  as indicated; the model predicts that the third and fourth electron peaks  $\epsilon_{3,4}$  will be unresolved, consistent with peak C. Hence, we believe that the 2DM model captures the key physics of the system. However, the model does not account for all of the features in the data, in particular the smaller peaks indicated by the colored arrows in Figure 4.19. With regard to the peak near  $-7 Ry^*$ , indicated by the left-hand brown arrow, the energy and magnitude are approximately consistent with the expected first-electron peak for 3DMs, a rough estimate gives  $-9 Ry^*$  and  $3.5 e/Ry^*$  for the energy and magnitude of this peak. No other 3DM peaks are as prominent in the measured data, probably owing to the overlap between the 3DM and 2DM spectra. We believe that some of

the measured structure between  $-6 Ry^*$  and  $0 Ry^*$ , such as the small peak near  $-5 Ry^*$  (right-hand brown arrow), arises from 3DMs. Small peaks also occur at positive energy, indicated by the purple arrows in Figure 4.19. In this case, we speculate that the peaks arise from the interplay between the tip potential and donor-molecule resonant states (that is, virtual bound states).

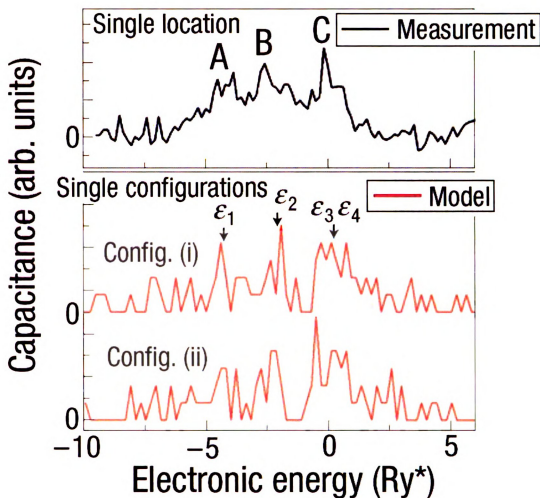


Figure 4.18: Comparison between representative measured data acquired at a single tip position (black) and representative modeled data (red); the modeled curves were calculated based on two different random configurations of donors, labeled config. (i) and config. (ii). To enable a direct comparison, we subtract the background capacitance from the measurements and plot the voltage in units of effective Rydbergs (scale factor  $\alpha_{tip}/8.1 \times 10^{-3} \text{V}/Ry^*$ ). The effective voltage increment for both the measured and modeled curves is approximately  $0.2 Ry^*$ . We see that the model predicts distinct broad peaks corresponding to the average electron addition spectra of the 2DMs; these peaks are reasonably qualitatively consistent with the observed peaks A, B and C. In contrast, the smaller fine-structure peaks, which correspond to individual charges entering the system, are different for different random configurations of the donors.

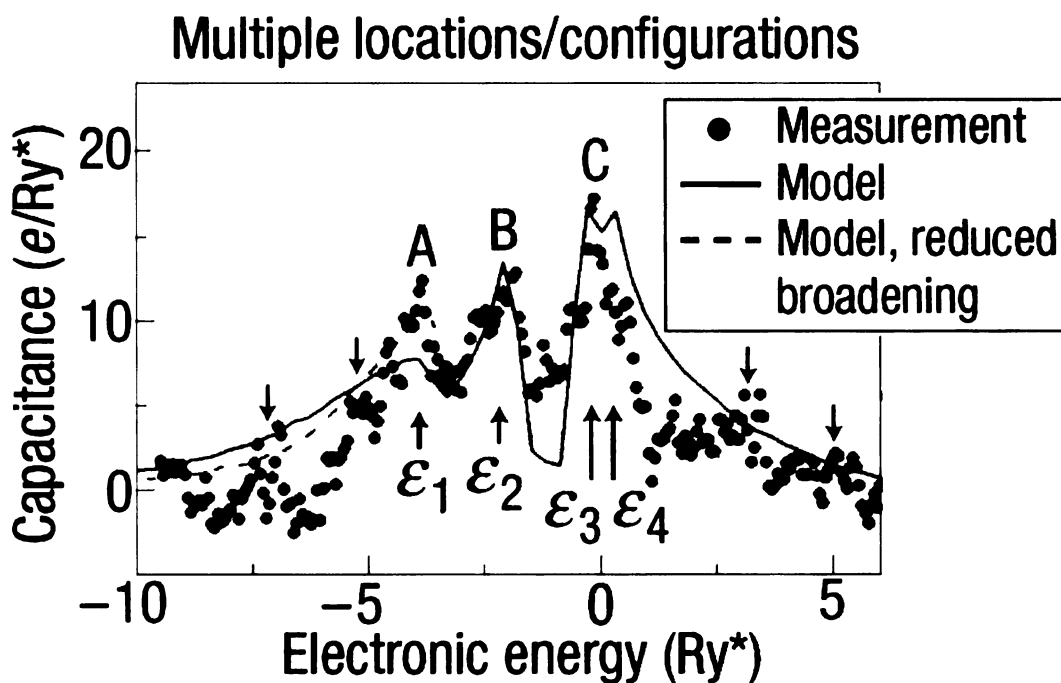


Figure 4.19: Comparison between the model and the measured data. The background capacitance (Figure 4.6 solid curve) has been subtracted from the local measurement (Figure 4.6 dots) to isolate the peaks. We display both the measured and modeled curves with the same horizontal scale of  $Ry^*$  and vertical scale of electrons per  $Ry^*$ . Although the match between experiment and theory is not exact, the overall agreement suggests that the donor-molecule model captures the correct physics. The gray curve addresses the discrepancy with regard to peak A, for which the predicted peak is significantly broader than the measurement; here we have reduced the broadening in the calculation by positioning the 2D layer 8 nm closer to the donor layer, which tends to sharpen the resonances.

# Chapter 5: Donor Layer Spectroscopy of a Gated Sample

In this chapter, I will introduce scanning-probe results describing donor layer charging acquired at fixed probe positions at an elevated temperature and in the vicinity of a metallic surface gate. In chapter 5, the data acquired from a bare surface at 0.27 K for a fixed tip position were described[51]. The data presented here are broadly consistent with the previous measurements. We analyzed the peaks in the context of thermal emission and field emission theories.

## 5.1 Thermal and Field Emission Theory

There are different physical mechanisms for charge to escape from a potential well. One of those mechanisms is that charge gets pushed out of the well due to an electric field between electrons. Another way that electrons can escape from a potential well is by thermal energy acquisition via lattice vibrations called phonons. Hence we should consider both the thermal distribution function and field dependence in the shape of the potential barrier. For low field strength, emission over the barrier (thermionic emission) is dominant and the temperature dependence of the Fermi-Dirac distribution function is mainly responsible for emitted charge carriers. For the opposite limit, in which the field is assumed to be high and temperature kept low, emission of electrons with energies below the energy barrier predominates. In this case, field dependence of the shape of the potential well is responsible for the emitted charge carriers, which is called “field emission” [64]. Field emission of electrons is a direct manifestation of quantum mechanical tunneling and it does not have a classical analog[65]. The thermal energy distribution is described by Boltzmann’s

statistics with a probability proportional to  $e^{-E/kT}$ , where  $E$  is the energy,  $T$  is the temperature, and  $k$  is the Boltzmann constant. The average thermal energy of an electron at room temperature is about 25 meV, and about 6 meV at liquid nitrogen temperature and about 0.4 meV for liquid helium temperature[66]. If the energy of the electron is sufficiently large compared to the barrier that confines it, it has a considerable probability to hop over the barrier and become unbound.

This effect can be introduced using finite square-well potential in the context of an electron continuum, such as electrons in a metal as shown in Figure 5.1 (a). The energy difference  $E_{vac} - E_F = \phi$  is known as the work function, where  $E_{vac}$  is the barrier height and  $E_F$  is the Fermi level of the continuum.  $\phi$  is the energy barrier that an electron must overcome in order to reach the energy level of the vacuum (far away from the continuum or well states) [13].

Careful theoretical treatment of thermionic emission from a metal leads to the Richardson's equation [64][67]:

$$J = AT^2 \exp\left(-\frac{\phi}{kT}\right). \quad (5.1)$$

Equation 5.1 relates the current density ( $J$ ) of a thermionic emission to the work function ( $\phi$ ) and temperature ( $T$ ) of the emitting system, where  $A$  is the Richardson's constant and  $k$  is the Boltzmann constant. Similarly, the thermal ionization of a hydrogen-like atom ( $D^0 = D^+ + e$ ) can be characterized in the form of an exponential function like Richardson's equation [68]. The characteristic temperature can be drawn from the internal partition function of the atom, which is sum over all nuclear and electronic states. For simplicity, we will take only the electronic bound states of the hydrogen-like atom giving:

$$Z_{D^0} \propto e^{-\epsilon/kT}, \quad (5.2)$$

where  $\varepsilon$  is the binding energy. The characteristic temperature,  $\Theta_{D0}$  from Equation 5.2 is:

$$\Theta_{D0} = |\varepsilon|/k. \quad (5.3)$$

With regard to field emission, for a metal the effect is described by the Fowler-Nordheim equation[69][70][65][71]. The Fowler-Nordheim tunneling current density for a potential barrier is given by,

$$J = K_1 F^2 \exp\left(-\frac{K_2}{F}\right), \quad (5.4)$$

where  $J$  is the current density,  $F$  is the electric field,  $K_1$  and  $K_2$  are field ( $F$ ) and effective barrier ( $\phi$ ) dependent conduction parameters[71]. In Figure 5.1 the effect of the potential of external electric field is shown.

The field strength required for tunneling can be estimated from the Heisenberg uncertainty principle[14]. Appreciable tunneling can occur only when the uncertainty in the position of the electron becomes comparable to the width of the barrier  $\phi/eF$ , where  $eF$  is the barrier slope due to the field. To calculate the uncertainty in momentum, the uncertainty in the kinetic energy can be taken of the order of the barrier height  $\phi$ . By plugging in these into uncertainty principle equation,

$$\Delta x \Delta p = \left(\frac{\phi}{Fe}\right) \sqrt{2m\phi} \approx \frac{\hbar}{2}, \quad (5.5)$$

and

$$F \approx \sqrt{\frac{8m\phi^3}{\hbar^2 e^2}} \approx 10^8 \text{ V/cm}, \quad (5.6)$$

where we use  $\phi = 1 \text{ eV}$  and  $m = 0.511 \text{ Mev}/c^2$  for the estimated field threshold  $F$ .

This estimation of the field strength for the field emission phenomenon does not include the contribution of the Coulomb interaction of the electron to its image charge in the Fermi sea. Thus, it is nearly an order of magnitude larger than the actual fields

for charge emission from the metals [65].

The same effect occurs for atomic systems, as shown in Figure 5.1 (b). In this context, it is usually referred to a “field ionization”. For natural atoms, this effect needs even higher electric fields  $(2-5) \times 10^8$  V/cm than required for field emission from metals [14].



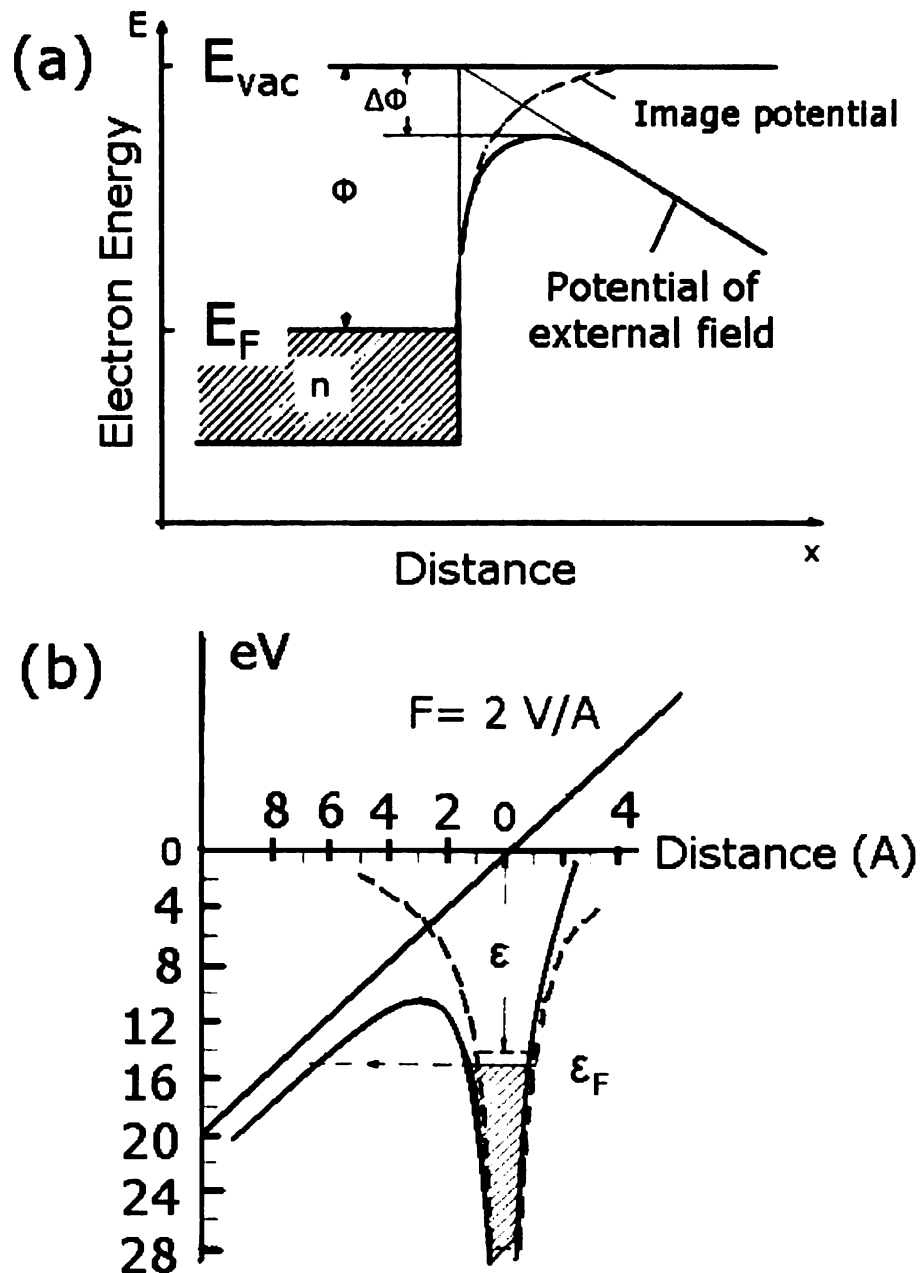


Figure 5.1: (a) Schematic diagram of the thermal emission of electrons from a continuum. An electron in potential well must overcome the work function barrier  $\phi = E_{vac} - E_F$  in order to reach the energy level of the vacuum and escape from the well. If an external field is applied, then  $\phi$  is reduced by an amount of  $\Delta\phi$  [13]. (b) A potential-energy diagram for a 1s electron of a H atom in a field of 2V/Å. Broken lines show the Coulomb potential in the absence of an external field [14].

## 5.2 Measurement and Analysis of Donor Molecules at 77 K

The localized probe measurements presented in this chapter were acquired at liquid nitrogen temperature at 77 K. Figure 5.2 shows the three plateaux characteristic of the vertical tunneling scheme of the electrons in the heterostructure: When the effective probe voltage is less than 0 V, the 2DES is totally depleted and the capacitance is low due to the large tip-3D substrate separation. By ramping the probe voltage to around 1 V, the Fermi level is pulled up so that 2DES is populated and capacitance increases. After full population of 2DES, the layer becomes metallic and the tip-2DES plane separation defines the capacitance. The region circled in red represents the donor layer charging, which is generally consistent with the previous measurements acquired at a fixed tip position at 0.27 K. For both measurements, the separation between the tip and the sample surface is held about 1 nm.

If the CAI curves in Figure 4.6 (0.27 K) and Figure 5.2 (77 K) are compared we see some differences. Figure 5.3 shows the comparison. Also shown, in blue, is a gated CAI curve that serves to show the background capacitance. The 0.27 K curve (red) shows three broad peaks, A, B, and C, which were attributed to four bound states. For the 77 K curve (black) peak C is missing. Moreover, peaks A and B are less-well resolved.

We can use thermal ionization theory to analyze these data. We should remember that, in our sample, Si donors reside in  $\text{Al}_{0.3}\text{Ga}_{0.7}\text{As}$ , for which  $a_0 = 7.3$  nm and  $Ry^* = 8.1$  meV [62, 51]. The thermal energy ( $kT$ ) is calculated as 6.6 meV at 77 K, which is comparable with the effective Rydberg energy of 8.1 meV for ionized Si donors in our crystal. In Figure 4.17 (a) configuration interaction calculations show that a donor molecule can accommodate up to 4 electrons and their average binding energies are  $\varepsilon_1 = 4 Ry^*$ ,  $\varepsilon_2 = 2.5 Ry^*$ ,  $\varepsilon_3 = 0.6 Ry^*$ , and  $\varepsilon_4 = 0.2 Ry^*$ , respectively. These

are the approximate values taken from Figure 4.17 (a), using a separation between Si atoms constituting the donor molecule of about one effective Bohr radius. Given that  $Ry^*$  is equal to 8.1 meV, the binding energies are  $\varepsilon_1 = 32.4$  meV,  $\varepsilon_2 = 20.3$  meV,  $\varepsilon_3 = 5.0$  meV, and  $\varepsilon_4 = 1.6$  meV. Substituting these binding energies ( $\varepsilon_n$ ; where  $n=1, \dots, 4$ ) to the Equation 5.3, we can calculate the corresponding characteristic ionization temperatures for the bound electronic states of a donor molecule, which are listed in Table 5.1. The ionization temperatures for the third and fourth bound states, which are 58 K and 19 K, are significantly lower compared to our elevated temperature, which is 77 K. Hence, the weakly bound third and fourth electrons should be on average emitted thermally from the two-donor molecule electronic states. However, this argument is not valid for the first and second electronic states. The corresponding ionization temperatures of these states are 385 K and 235 K, respectively, which are much higher compared to 77 K. In other words, these states are deeply bound and the thermal activation of the electrons at 77 K is not on average enough to knock out the electrons from the donor molecules. this picture is consistent with the picture we get from comparing two curves (red and black) in Figure 5.3 as the missing peak C corresponds to the third and fourth bound electrons.

Table 5.1: Characteristic Ionization Temperatures for 2DM Bound States

Bound State ( $\varepsilon$ )	Binding Energy (meV)	Characteristic Temperature ( $\Theta_{2DM}$ , K)
1	32.4	375
2	20.3	235
3	5.0	58
4	1.6	19

The second observation from the comparison of the two curves is that the peaks labeled A and B are not resolved for the data acquired at 77 K. The thermal broadening width of bound states is determined by the width of the Fermi function derivative  $= 3.5kT$ . At 77 K, the parameter is  $3.5 \times (6.6 \text{ meV}) \cong 20 \text{ meV}$ . This is greater than  $\varepsilon_1 - \varepsilon_2 = 12.1 \text{ meV}$  [72], hence we expect the peaks due to the first and second bound

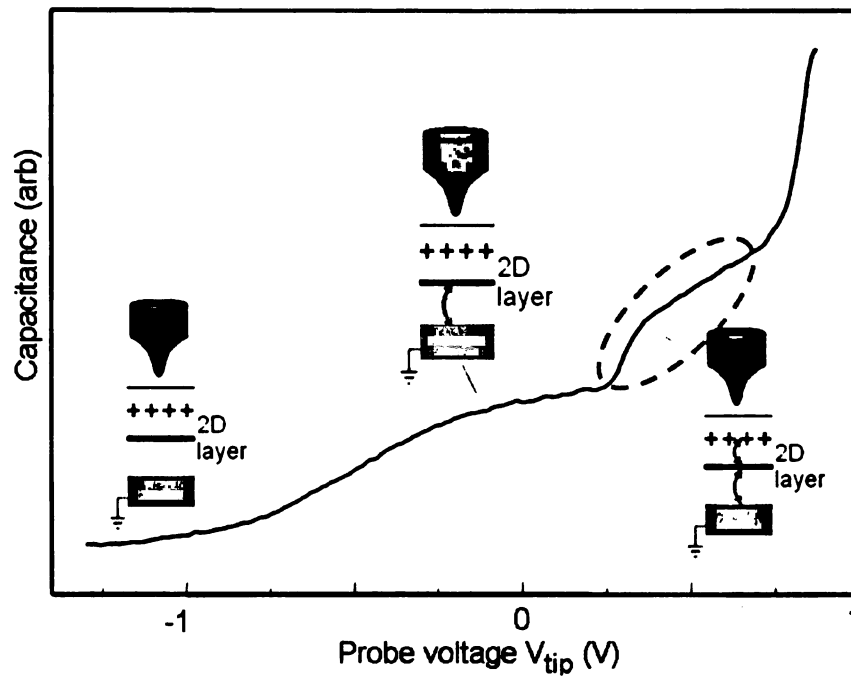


Figure 5.2: Capacitance curve acquired at 77 K with a probe at a fixed position 1nm above the surface of the wafer. The encircled region shows the donor layer resonance, which is consistent with the previous measurements.

electrons to be poorly resolved.

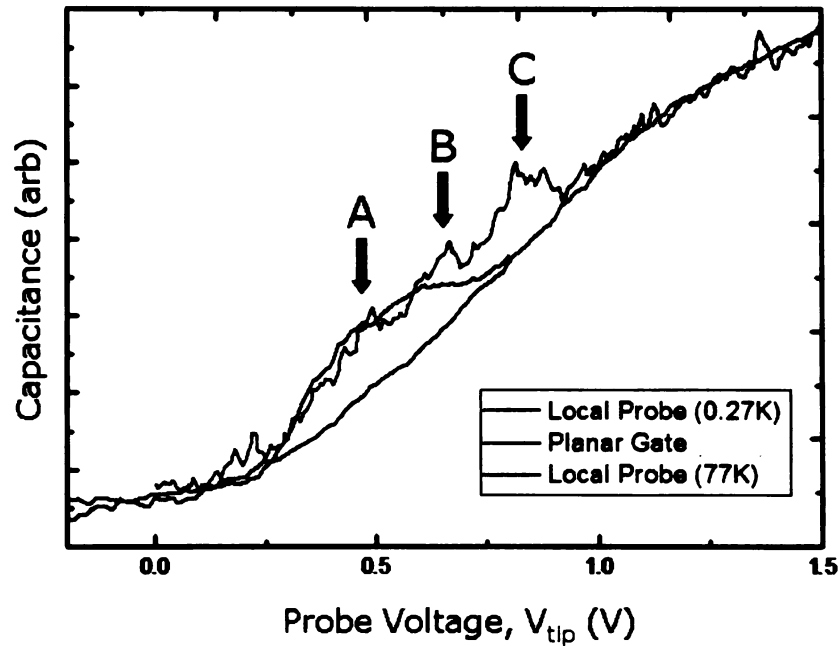


Figure 5.3: Capacitance curves for data acquired at 0.27 K and 77 K superposed with the gated capacitance curve (Ref. Figure 4.1) The third and fourth bound electrons, peak C, are missing for the data acquired at liquid N<sub>2</sub> temperature, which can be attributed to the thermal emission of electrons from 2DMs. The excitation voltage,  $V_{exc}$  applied to the curve taken at 77 K is also larger than the  $V_{exc}$  applied to the curve taken at 0.27 K, which are 16 mV and 3.8 mV. The excitation amplitude present at the donor layer is diminished by the lever arm factor  $\alpha \cong 10$ . Hence, excitation voltage does not significantly contribute to the broadening of these unresolved peaks.

## 5.3 Measurement and Analysis of Field Emission of Donor Molecules

The effect of external electric field on small numbers of dopant atoms inside a semiconductor is highly interesting for recent quantum information proposals. Precise control of the electronic states of a single dopant atom is needed for a functional quantum computer[19, 17, 18, 30, 1]. The potential gradient due to the presence of a metallic gate has a significant effect on the donor layer charging experiments introduced earlier in this thesis. In the previous section I explained how thermal energy can influence the donor molecule addition spectrum. In this section the evolution of the donor layer charging will be introduced as the tip is brought closer to a top gate from the side.

We fabricated 25 nm tall titanium-gold gates on top of the surface of the  $\text{Al}_{0.3}\text{Ga}_{0.7}\text{As}/\text{GaAs}$  wafer by the electron beam lithography technique, which is depicted in Figure 5.4. Figure 5.4 (a) shows a scanning electron microscope (SEM) picture of a metallic mesh deposited on the surface. The width of the lines are 200 nm and they are  $12.5 \mu\text{m}$  apart from each other. In Figure 5.4 (c), an enlarged version of the SEM image of circular gate is shown. This image shows that our lithographically defined gates are spatially precise on the scale of about 50 nm, which is comparable to the radius of our CAI tip. Figure 5.4 (b) shows the topography of the circular gate imaged by the CAI method. Our technique is very stable for hours while scanning at low temperatures inside the cryostat. The image is averaged over 32 times and there were no evidence of a considerable drift in the position of the imaged gate. The circular regions A1 and A2 represent the probed areas for the local probe measurements. A1 is approximately a distance of 100 nm from the gate, while the distance between gate and A2 is about 500 nm. Figure 5.4 (d) is a three dimensional tunneling mode image of the gates showing representative tip diagrams

at the far (A2) and near (A1) gate positions.

The method becomes more subtle compared to the local-probe measurements for the sample with no surface gate. Since we have 25 nm tall topographic structures on the crystal surface, we move the tip very carefully so as not to bump into any of these surface structures. After thermal cycling we begin each data run by scanning the tip in both tunneling and capacitance modes to check that the surface is sufficiently clean and free from major electronic defects. Tip must be held back at least 30 nm from the surface for the initial capacitance-mode scanning so as to avoid crashing into the gates. To acquire the capacitance curves, we select a certain location and position the tip about 1 nm above the GaAs surface.

We start by focusing on data acquired at five distances from the surface gate. In Figure 5.5 the evolution of the capacitance curves is seen, for which the locations are labeled from A to E. These locations are selected far from the gate to closer distances. The data for curve A is acquired at a location which is about  $0.5 \mu\text{m}$  away from the gate. The formation of 2DES and donor layer charging resonance can be clearly observed from curve A, which is consistent with the local-probe measurements in the absence of the top gate. As we move our tip to the locations closer to the surface gate, two clear gradual distinctions in the capacitance curves B, C, and D are observed: First, the donor layer resonance is dramatically suppressed. Second, the 2DES plateau formation is perturbed resulting in a positive slope. It means that we never get a fully formed 2DES in all of the area interacting with the tip. The tip is located on top of the metal gate to acquire the data for curve E. The flat curve is an expected result since the metallic behavior of the gate screens the charge activity inside the semiconductor crystal; the result is simply a capacitance corresponding to the tip-metal gate separation.

Turning our attention first to the plateau formation, we expect the gate potential to affect the two-dimensional system residing 80 nm below the gate. In the parallel

plate capacitor approximation, the presence of the gate electrodes should give an offset equal to the effective potential due to the work function. In this case this would result in a shift in the plateau formation in our CAI curves. This should be the case for the region right below the gates [6, 73]. When our probe is near the gate, the fringing electric field effectively gives a range of voltages for the plateau formation. We believe this is the reason we see poorly formed plateaus in the C-V curves of Figure 5.5 for probe positions close to the gate.

Next we can focus on the energies, where the donor layer resonance is expected. This region corresponds to the effective probe voltage range from 0.2 V to 0.8 V, shown in Figure 5.6. We show three curves: The red and black curves are the data collected by localized-probe at locations A1 and A2, respectively (see Figure 5.4). The blue curve is our background curve acquired by the gated capacitance technique, which was explained in chapter 5. The same adjustments are done to superimpose the background curve with the other curves.

In Figure 5.7 we plot these data with the background subtracted. It is seen that there is a significant reduction in the amplitude of the donor resonances. The value of the enhanced capacitance of the donor resonance for the case close to the gate (location A1 in Figure 5.4) is decreased more than 50% compared to the value taken from the data at the location A2, where it is approximately 100 nm in the vicinity of the gate electrode.

What physics could give rise to the suppression of the charging effect due to the electron tunneling between the base electrode (2DES) and donor layer? We analyze these data in the context of field-ionization theory. The top gate and 2DES can be considered as a finite-length parallel plate capacitor with a dielectric constant of  $\kappa = 12.1$ . The fringing electric field emerging from the top plate and terminating at the 2DES creates a potential gradient over the region between these two plates as seen in Figure 5.9. For the data shown in this section we have not applied any external



d.c. voltage to the gate. We observed the influence of the potential gradient due to the work function difference between the metallic gate and the sample. From the difference between the contact potentials of PtIr tip and TiAu gold gate, we can determine the effective potential applied by gate electrode: The contact potential of the PtIr tip, and GaAs sample,  $V_{contact}^{PtIr}$ , is determined as 0.6 V from *in situ* Kelvin probe measurements[37]. Comparing capacitance curves acquired with the tip to those acquired with a TiAu electrode, the observed shift in the curves implies  $V_{contact}^{TiAu} = 0.12$  V; this value agrees reasonably well with the reported work functions of Ti and Au, in comparison to Pt and Ir [57]. In other words, the effective gate potential is 120 mV.

Field-emission phenomenon is a pure quantum mechanical effect, which was introduced earlier in this chapter . The schematic diagram representing the potential energy of two-donor molecules (2DM) can be seen in Figure 5.8. In the presence of a fringing electric field the symmetry of hydrogen-like potentials created by the donor centers is broken (on average). The potential energy diagram is depicted for both cases, in the presence and absence of the gate potential, shown in Figure 5.8. The tilt emerging in the donor-molecule potential opens up a reasonable probability for the bound electrons to tunnel away from the molecule. This argument is valid if the width of the barrier is comparable with the spatial extent of the electron wave function. For natural H atoms in free space a field strength of  $F \approx 5 \times 10^8$  V/cm is necessary for electrons to be emitted. As can be seen from Equation 5.5,  $F$  scales inversely with the size of the bound electron and roughly in proportion to the binding energy. Hence, as a rough estimate we can scale the H-atom results using our effective radius of  $\sim 3 a_B^* \approx 21$  nm and binding energies of  $\varepsilon_1 = 32.4$  meV,  $\varepsilon_2 = 20.3$  meV. This procedure yields  $3.2 \times 10^3$  V/cm and  $2.0 \times 10^3$  V/cm as the threshold field for the first and second bound electrons. The constant electric field created by the local gate potential, assuming the gate electrode and 2DES act as a parallel plate capacitor with

a separation of 80 nm and a dielectric constant  $\kappa=12.1$  is  $1.24 \times 10^3$  V/cm, which is comparable to the estimated scaled value of threshold electric field,  $F(\varepsilon_1)$  and  $F(\varepsilon_2)$ . Given that these two calculated electric fields are on the same order of magnitude we can conclude that the emission of the first and second bound electrons is possible through tunneling across the tilted hydrogen-like potential barrier, which is qualitatively consistent with our observations of the donor layer charging near a surface gate electrode.

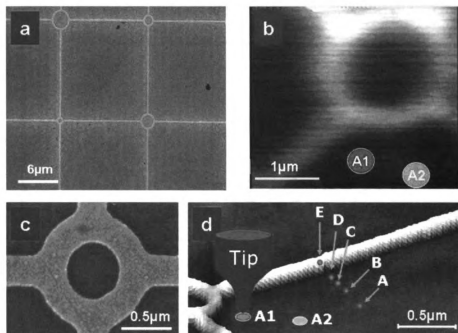


Figure 5.4: (a) A scanning electron microscope (SEM) micrograph of the gates fabricated on the surface of the wafer by electron beam lithography is shown. The separation between the line shapes is  $12.5 \mu\text{m}$ . The planar dimension of the mesh is approximately  $1 \text{ mm} \times 1 \text{ mm}$ . (b) Scanning-probe image of a circular gate in capacitance mode. This image is an average of 32 capacitance scans. (c) Enlarged SEM image of circular gate with a diameter of  $0.5 \mu\text{m}$ . (d) Scanning tunneling image of the gate is depicted with the labels showing the locations of the data acquired for localized probe measurement. A schematic diagram of tip is also shown.

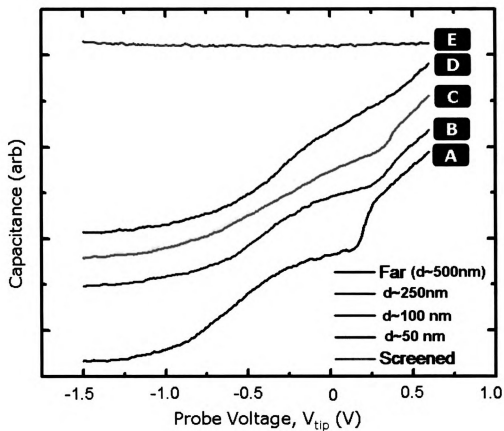


Figure 5.5: The evolution of the capacitance curves acquired at different tip locations are shown. The deformation of 2DES plateau and suppression of the donor layer charging is observed due to the proximity of the probe to the gate electrode.

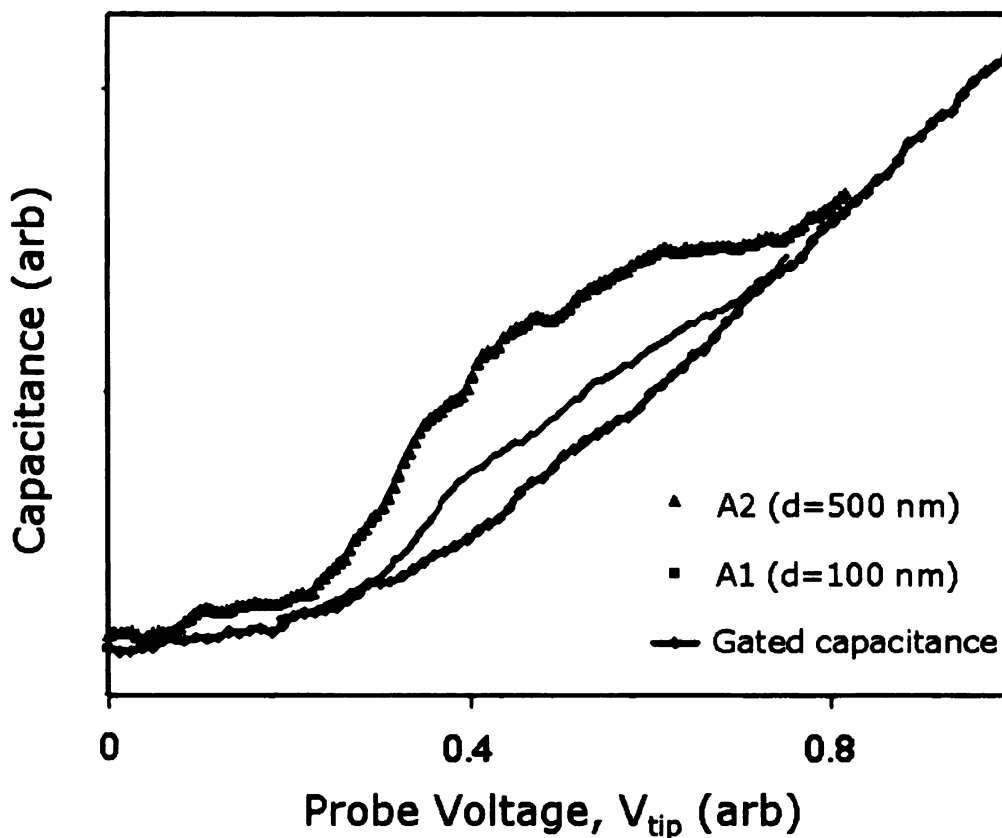


Figure 5.6: Localized-probe data acquired at 77 K corresponding to the locations in the presence (A1) and absence (A2) of a gate potential are shown in red and black, respectively. The black curve represents the data at the tip position where the gate potential does not influence the donor layer, which is the same data as the black curve in Figure 5.3. The blue curve is the gated capacitance measurement which is used as a background curve for the localized-probe measurements. The adjustments are done in order to superimpose the data on top of each other. The lever arm factor difference between tip-sample and gate-sample are adjusted to scale the capacitance acquired by both methods. The shifts with regard to probe voltage were also required to correct for perturbations of trapped charges.

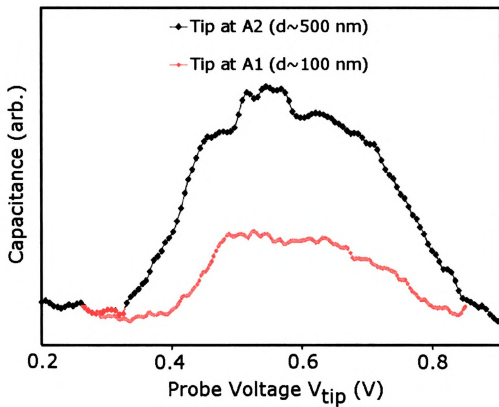


Figure 5.7: Comparison of curves acquired at A1 and A2 with the background curve is subtracted from each. The clear suppression of resonance in the vicinity of the gate electrode is observed. This corresponds to a decrease of more than 50% in the amplitude of the enhanced capacitance peak due to charging into the donor layer.

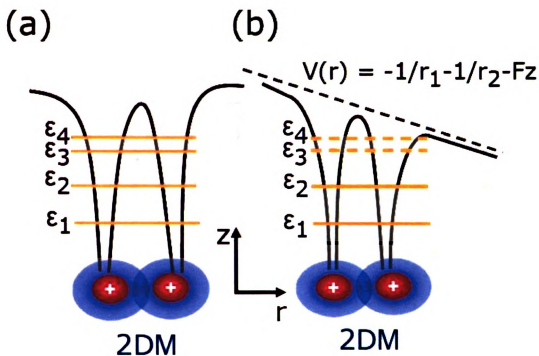


Figure 5.8: (a) (b) The schematic potential landscape of the two-atom donor molecules (2DMs) in the absence and the presence of the electric field are shown. These are also representing the potential landscapes at the locations A2 and A1 shown in Figure 5.9. The four bound state energy levels are also represented with the orange lines, schematically.

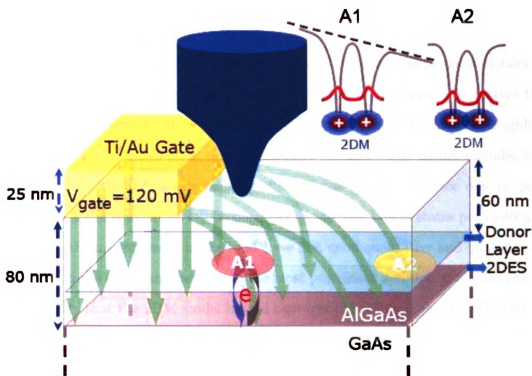


Figure 5.9: A simplified schematic representation of the localized-probe measurement in the vicinity of the gate electrodes is shown. The delta-doped donor layer resides 60 nm below the surface and 2DES is formed 20 nm below the donor layer. The region labeled as A1 represents the probed area of the donor layer near gate in the  $x$ - $y$  plane, whereas A2 shows the area away from the gate. The corresponding potential landscapes of the two-donor molecules (2DM) for A1 and A2 are also shown. The schematic diagram of fringing electric field ( $F$ ) created in the GaAs sample by gate potential is depicted with green arrows.



# Chapter 6: Conclusions and Future Directions

## 6.1 Summary

In summary, we have measured the electron addition spectrum of silicon donors in a gallium-arsenide heterostructure using a scanning probe technique. To analyze the data we have developed a theoretical model based on the idea that nearest-neighbor pairs effectively form two-atom donor molecules (2DMs). The model includes the influence of the tip and the broadening effect of non-nearest neighbor donors, predicting that three resonances will be observed due to four bound states per molecule. Comparing the measurement to the model, we find good qualitative and quantitative agreement in the shape and position of the most prominent addition spectrum peaks. This suggests that the 2DM model indeed captures the relevant physics. This study represents the first measurement of the electron addition spectrum of donor molecules in a semiconductor system.

We have also measured the donor layer charging in the presence of a titanium-gold gate at 77 K. We observed that weakly bound third and fourth electrons are missing from the addition spectrum of donor molecules. This effect is attributed to the thermal activation of electrons enabling them to overcome the potential barrier. This is consistent with the characteristic ionization temperatures calculated for each electron binding energy, which are calculated by configuration-interaction theory. We also conclude that first and the second peaks are less-well resolved due to thermal broadening. Finally, the suppression of the addition spectrum peaks of donor molecules in proximity to a surface gate electrode is explained in the context of the field-ionization theory. We observed more than a 50% reduction in the amplitude

of the resonance peak created by the tunneling of first and second electrons. The threshold of electric field enabling electrons to escape from the tilted potential barrier in the vicinity of top gate is estimated. It is of the same order of magnitude as the electric field created in the sample by the effective gate potential. This leads us to conclude that the reduction is likely due to the emission of electrons by the electric field in our semiconductor heterostructure.

## 6.2 Future Directions

Thus far, we have probed Si doped  $\text{Al}_{0.3}\text{Ga}_{0.7}\text{As}/\text{GaAs}$  for which the lateral positions of dopants are random. The immediate future direction is to develop a more quantitative analysis comparing data with the model, which includes temperature and density variations of two-dimensional electron system due to the effective potential of the gate electrodes [74].

In addition to our study on donor layer charging, my colleague, M. Gasseller, has recently imaged the spatial distribution of boron acceptors in silicon, as seen in Figure 6.1. The logical direction for the future research is to probe controlled arrangements of donor atoms instead of randomly distributed dopants. Our CAI technique can be utilized more efficiently to study small lithographically-defined clusters of donors. Adjacent clusters will be separated by a distance much greater than the effective Bohr radius; hence the measurement will effectively probe isolated donor molecules. This effort will take advantage of recent advances in the nanotechnology of donors in silicon – driven in large part by the proposal of the Kane computer.

Recent years, we have seen considerable progress in realizing nanometer-scale control of phosphorus donors in silicon [1]. This is an example of a dopant system which possesses the ideal parameters for our technique to probe. In collaboration with Michelle Simmons at the University of New South Wales, Sydney, Australia, the initial

proposed experiment will probe an array of donor molecules as shown schematically in Figure 6.2. Each molecule will consist of two phosphorus donors, with 100 nm between nearest-neighbor molecules – much greater than the Bohr radius. The distance between the two atoms in a molecule will vary from  $\sim 1$  to  $\sim 15$  nm.

Subsequent studies will probe more complex arrangements of atoms within molecules, as the fabrication technology matures further. We also plan to apply the CAI technique to samples with small surface gates in proximity to the donors to study further how metallic interfaces and applied electric fields perturb the quantum levels [2, 30].

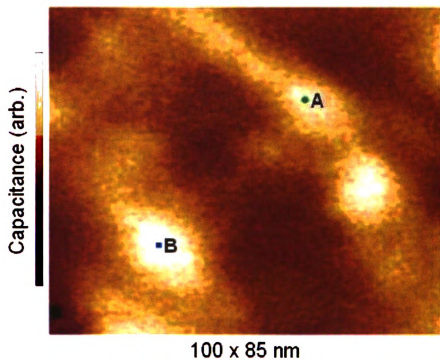


Figure 6.1: CAI image with the tip voltage set at 0.05 V. The density of the bright high-capacitance features is consistent with the delta-doped B concentration in Si crystal. [Courtesy M. Gasseller].

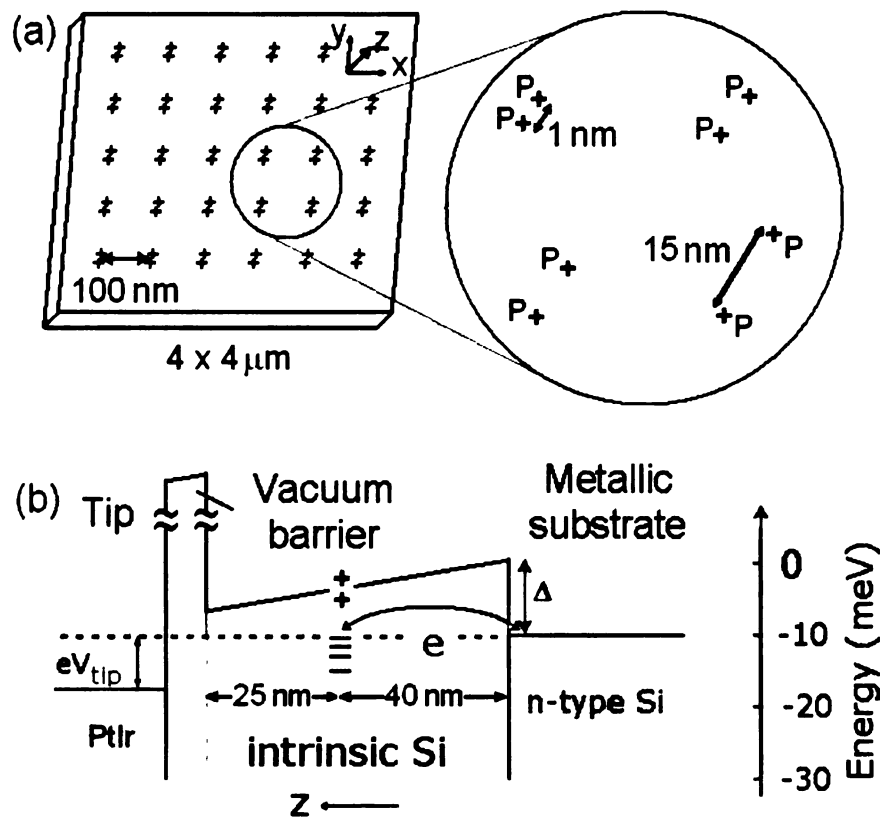


Figure 6.2: (a) Schematic of isolated donor molecule CAI measurement. The sample will be grown by the Simmons research group at the Atomic Fabrication Facility at the University of New South Wales [Perera]. (b) Conduction band profile.

# Appendix A: Configuration Interaction Theory

## A.1 Introduction

The Schrodinger equation

$$H\Psi = E\Psi \tag{A.1}$$

establishes the foundation for the solution of all the problems in atomic and molecular structures[75, 76]. Knowing the exact form of the Hamiltonian for a molecular system and the methods for solving an eigenvalue equation, it is theoretically possible to exactly determine the total energy and wave function for that system. Practically, the solution of the wave equation, even for the simplest case of diatomic molecules, can not be accomplished without applying many approximations since they are very complicated system of mutually interacting nuclei and electrons[77]. For molecules Born-Oppenheimer(BO) approximation is the first approximation which is used in all quantum chemical systems, in which the nuclear and electronic wave functions are considered separable[75]. This approximation relies on the physical picture of massive nuclei moving much slower than the electronic motion[78]. According to the BO approximation, the total wave function can be written

$$\Psi(r, R) = \psi_e(r)\phi(R) \tag{A.2}$$

The function  $\psi_e(r)$  is called the *electronic wave function* and depends only on the quantum states of electrons for fixed positions of the nuclei. The function  $\phi(R)$  is called the *nuclear wave function* and it describes the rotational and vibrational motion of nuclei[77].

The electronic Hamiltonian in atomic units can be written as the form of

$$H_e = - \sum_{i=1}^n \frac{1}{2} \nabla_i^2 - \sum_{i=1}^n \sum_{A=1}^M \frac{Z_A}{r_{iA}} + \sum_{i=1}^n \sum_{j>i}^n \frac{1}{r_{ij}} \quad (\text{A.3})$$

where first term is the kinetic energy expression,  $r_{iA}$  are the separation between nuclei and electrons, and  $r_{ij}$  are the electron-electron distances. The nuclear Hamiltonian depends on the total electronic energy at each choice of nuclear configurations. In the context of the BO approximation, the nuclei move on a potential energy surface obtained by solving the electronic wave equation.

## A.2 Variation Method

Even with the separation of the nuclear and electronic wave functions provided by the BO approximation, the electronic Schrödinger equation does not have any known solution. In other words more approximations are needed to get a solution. Nearly all current electronic structure calculations are based on the approximation of variational principle. For any normalized approximate wave function  $\Psi$ , the energy is just the expectation value of the Hamiltonian operator. The variational principle is based on the fact that the energy  $E$  achieved by this method is a rigorous upper bound to the true energy. Namely, the energy  $E$  calculated for any approximate wave function  $\Psi$  will lie above the exact energy of the relevant quantum mechanical system. Therefore the “best” wave function of a given form is that for which all parameters have been varied to yield the lowest energy[75]. If the assumed functions are sufficiently comprehensive, the true energy may be approached quite closely. The main drawback to this procedure is that it is difficult to estimate how far to calculate the energy from the true energy. If we assume that a quantum mechanical system satisfies the equation (A.1), in particular the ground state Schrödinger equation can

be denoted as

$$H\psi_0 = E_0\psi_0 \quad (\text{A.4})$$

If ground state wave function  $\psi_0$  were known,  $E_0$  could be calculated from the integration

$$E_0 = \int \psi_0^* \mathbf{H} \psi_0 d\nu \quad (\text{A.5})$$

where  $d\nu$  is the total volume element for all particles in the system.

In practice, it is hard to deal with finding  $\psi_0$ , so that one could only guess a good trial function called “variation function”,  $\phi$ , which is supposed to approximate  $\psi_0$ . Even though the specific form of the exact solutions  $\psi_0, \psi_1, \psi_2, \dots$  is not known,  $\phi$  could be expanded in terms of these functions mathematically

$$\phi = \sum_n \alpha_n \psi_n \quad (\text{A.6})$$

The function  $\phi$  may be chosen arbitrarily to be normalized in a way that

$$\sum_n |\alpha_n|^2 = 1 \quad (\text{A.7})$$

An expectation value for this trial function can be found as

$$W_0 = \int \phi^* \mathbf{H} \phi d\nu \quad (\text{A.8})$$

From the combination of equations (A.6) and (A.8) we can get

$$\begin{aligned} W_0 &= \sum_m \sum_n \alpha_m^* \alpha_n \int \phi_m^* H \phi_n d\nu \\ &= \sum_m \sum_n \alpha_m^* \alpha_n E_n \int \phi_m^* \phi_n d\nu \end{aligned} \quad (\text{A.9})$$



Since the functions  $\phi_m$  and  $\phi_n$  are chosen to be orthogonal if  $m \neq n$

$$W_0 = \sum_n |\alpha_n|^2 E_n \quad (\text{A.10})$$

By subtracting  $E_0$  from both sides of equation (A.10), the result becomes

$$W_0 - E_0 = \sum_n |\alpha_n|^2 (E_n - E_0) \quad (\text{A.11})$$

Since  $E_n \geq E_0$  for all  $n$ , and  $|\alpha_n|^2 \geq 0$ , the right side of this equation is  $\geq 0$ . Therefore, it has been shown that the variational energy always obeys the rule

$$W_0 \geq E_0 \quad (\text{A.12})$$

Since the value of  $W_0 \geq E_0$  for any set of parameters chosen, the parameters should be adjusted to produce a minimum value of  $W_0$  in order to approach the minimum energy as close as possible. A possible way of doing this is to minimize the partial derivative of the variational energy with respect to the adjustable parameters of the trial wave function. A particular method of doing this is to choose  $\phi$  as a linear combination of specific arbitrary functions with adjustable parameters for the expansion coefficient of the form of

$$\phi = c_1 \xi_1 + c_2 \xi_2 + \dots + c_n \xi_n \quad (\text{A.13})$$

where each arbitrary function  $\xi_n$  is precisely specified. Such function is called a “linear variation function”, and yields  $W_0$  in the form

$$W_0 = \left\{ \sum_{m=1}^N \sum_{n=1}^N c_m c_n H_{mn} \right\} / \sum_{m=1}^N \sum_{n=1}^N c_m c_n S_{mn} \quad (\text{A.14})$$

where

$$H_{mn} = \int \xi_m^* H \xi_n d\nu, \quad S_{mn} = \int \xi_m^* \xi_n d\nu \quad (\text{A.15})$$

where  $S_{mn}$  is the normalization integral. Then it is easier to differentiate the rearranged form of the equation (A.14)

$$W_0 \sum_{m=1}^N \sum_{n=1}^N c_m c_n S_{mn} = \sum_{m=1}^N \sum_{n=1}^N c_m c_n H_{mn} \quad (\text{A.16})$$

with respect to the arbitrary  $c_k$

$$\begin{aligned} \left( \frac{\partial W_0}{\partial c_k} \right) \sum_{m=1}^N \sum_{n=1}^N c_m c_n S_{mn} &+ W_0 \frac{\partial}{\partial c_k} \left( \sum_{m=1}^N \sum_{n=1}^N c_m c_n S_{mn} \right) \\ &= \frac{\partial}{\partial c_k} \left( \sum_{m=1}^N \sum_{n=1}^N c_m c_n H_{mn} \right) \end{aligned} \quad (\text{A.17})$$

The condition for the minimum  $W_0$  is that  $\partial W_0 / \partial c_k = 0$  for  $k = 1, 2, \dots, n$ . This leads to the set of equations

$$W_0 \frac{\partial}{\partial c_k} \left( \sum_{m=1}^N \sum_{n=1}^N c_m c_n S_{mn} \right) = \frac{\partial}{\partial c_k} \left( \sum_{m=1}^N \sum_{n=1}^N c_m c_n H_{mn} \right) \quad (\text{A.18})$$

Since  $\partial c_j / \partial c_k = \delta_{jk}$ , equation (A.18) reduces to

$$\sum_{n=1}^N c_n (H_{nk} - S_{nk} W_0) = 0 \quad k=1, 2, \dots, N \quad (\text{A.19})$$

with the assumption of  $S_{mn} = S_{nm}$  and  $H_{mn} = H_{nm}$ . This constitutes a set of  $N$  homogeneous linear equations with  $N$  independent variables  $c_1, c_2, \dots, c_N$ . This set of equations can have nontrivial solutions if the determinant of the coefficients of the

$c_n$  be zero

$$\begin{vmatrix} H_{11} - S_{11}W_0 & H_{12} - S_{12}W_0 & \cdots & H_{1N} - S_{1N}W_0 \\ H_{21} - S_{21}W_0 & H_{22} - S_{22}W_0 & \cdots & H_{2N} - S_{2N}W_0 \\ \vdots & \vdots & & \vdots \\ H_{N1} - S_{N1}W_0 & H_{N2} - S_{N2}W_0 & \cdots & H_{NN} - S_{NN}W_0 \end{vmatrix} = 0 \quad (\text{A.20})$$

There are  $N$  roots of this equation and the lowest value of  $W_0$  is the upper limit to  $E_0$ . The coefficients  $c_k$  that are not normalized can be determined by successive substitution of these roots into equation A.19[79].

### A.3 Strong Correlation (The Heitler-London Picture)

Two different conceptual methods have been implemented to understand the qualitative and quantitative behavior of the bonding in quantum many-body systems: The Heitler-London (HL) approach and the molecular orbital (MO) model. The first one is the assuming electrons strongly correlated quantum mechanical objects treated by Heitler and London for the calculations of the ground state for  $\text{H}_2$  molecule. The HL theory, which is also called valence bond theory, can be recognized as the very starting point of the molecular quantum mechanics. The valence-bond method involves the use of a wave function such that the two electrons of electron-pair bond between two atoms tend to remain on two different atoms[80]. The motivation for Heitler and London was, at first, to estimate the Van der Waals interaction energy between two H atoms assuming that they are adequately far apart from each other. The Van der Waals interaction is universally valid for all atoms and molecules, however, the magnitude of interaction is much smaller than the exchange interaction between the atoms, whose electron clouds overlap significantly[81].

The theoretical understanding of bonding has been developed after the Heitler and London's work on the ground state of  $H_2$  molecule soon after the development of quantum mechanics[82]. If two protons are brought together in the original two hydrogen atom problem, the Pauli exclusion principle requires that the two-electron wave function be properly antisymmetrized with respect to interchange of electrons:

$$\Psi(r_1\sigma_1, r_2\sigma_2) = -\Psi(r_2\sigma_2, r_1\sigma_1) \quad (\text{A.21})$$

where  $\sigma_1$  and  $\sigma_2$  refer to spin up and spin down spinors, respectively.

Since there is no spin-orbit coupling in the Hamiltonian of the system the spatial and spin variables can be separated:

$$\Psi(r_1\sigma_1, r_2\sigma_2) = \Psi(r_1, r_2)\chi(\sigma_1, \sigma_2) \quad (\text{A.22})$$

where  $\chi$  are the spin orbitals.

The spatial wave function can be taken as a combination of products of hydrogen-like wave functions of the individual electrons. The Pauli principle requires that the spin function be antisymmetric if the spatial function is symmetric under interchange of electrons and vice versa. The ground state wave function can be denoted as a singlet and triplet parts of the form of

$$\begin{aligned} \Psi_{HL}^s(1, 2) &= N_s [\phi_1(\mathbf{r}_1)\phi_2(\mathbf{r}_2) + \phi_2(\mathbf{r}_1)\phi_1(\mathbf{r}_2)] \chi_s(\sigma_1, \sigma_2) \\ \Psi_{HL}^t(1, 2) &= N_t [\phi_1(\mathbf{r}_1)\phi_2(\mathbf{r}_2) - \phi_2(\mathbf{r}_1)\phi_1(\mathbf{r}_2)] \chi_t(\sigma_1, \sigma_2) \end{aligned} \quad (\text{A.23})$$

Where  $N_s$  and  $N_t$  are the normalization constants,  $\phi_{1,2}(\mathbf{r})$  are the spatial orbitals corresponding to each electron centered on nuclei 1 and 2, and  $\chi_s$  and  $\chi_t$  are singlet and triplet spin wave functions, respectively. The wave function chosen in the Heitler-London picture does not allow two electrons occupy the same site and, therefore, has

a built in correlation that reduces the Coulomb repulsion between the electrons. Since the Hamiltonian is spin independent, the only way the spin orbitals affect the energies is in the determination of the symmetry of the spatial wave functions[83].

## A.4 Hartree-Fock Approximation

### A.4.1 Molecular Orbital Theory

The molecular orbital theory, was first developed by Hund[84] and Mulliken[85]. It is based on the idea of independent electrons. In atoms, electrons reside in orbitals of differing energy levels such as 1s, 2s, 3d, etc. These orbitals represent the probability distribution for finding an electron anywhere around the atom. Molecular orbital theory implies that electrons in molecules likewise exist in different orbitals that give the probability of finding the electron at particular points around the molecule. To produce the set of orbitals for a molecule, one must add the atomic wave functions for the bonded atoms in the molecular structure.

The simplest and historically most concentrated molecule is the  $\text{H}_2$ . Each hydrogen atom in  $\text{H}_2$  has only the 1s orbital, so to get the MO one must add two 1s orbitals in a particular manner that is such that respecting the phase structure of the atomic orbitals (Figure A.1). The in-phase overlap combination (top set of orbitals in Figure A.1) produces a build-up of electron density between the two nuclei which results in a lower energy for that orbital. The electrons occupying the  $\sigma_{\text{H}-\text{H}}$  orbital represent the bonding pair of electrons from the Lewis structure of  $\text{H}_2$  and is named a “bonding molecular orbital”. The other molecular orbital produced,  $\sigma_{\text{H}-\text{H}}^*$  shows a decrease in electron density between the nuclei reaching a value of zero at the midpoint between the nuclei where there is a nodal plane. Since the  $\sigma_{\text{H}-\text{H}}^*$  orbital shows a decrease in bonding between the two nuclei, it is called an “anti-bonding molecular orbital”. Due to the decrease in electron density between the nuclei, the anti-bonding orbital

is higher in energy than both the bonding orbital and the hydrogen 1s orbitals. In the molecule  $H_2$ , no electrons occupy the anti-bonding orbital.

Relative energies of the bonding, anti-bonding, and atomic orbitals can be constructed and shown in an orbital correlation diagram, as in Figure A.2. In general, bonding molecular orbitals are lower in energy than either of their parent atomic orbitals. Similarly, anti-bonding orbitals are higher in energy than either of its parent atomic orbitals. Because of the law of conservation of energy, the amount of stabilization of the bonding orbital must equal the amount of destabilization of the anti-bonding orbital[86]. The correlation diagram can be more complicated for combinations of other atomic orbitals. Eventually one can produce molecular orbitals as the linear combinations of atomic orbitals(LCAO). The molecular orbital volume encompasses the whole molecule. It is assumed that the electrons would fill the molecular orbitals of molecules like electrons fill atomic orbitals in atoms:

- The molecular orbitals are filled in a way that yields the lowest potential energy for the molecule.
- The maximum number of electrons in each molecular orbital is two. (follows the Pauli exclusion principle.)
- Orbitals of equal energy are half filled with parallel spin before they begin to pair up. (follows Hund's Rule.)

The molecular orbital theory worked very well compared to strong interaction since most chemical bonds are relatively weakly correlated. The independent electron model is not very successful in the systems such as copper-based high temperature superconductors[87] that have strongly correlated electrons.

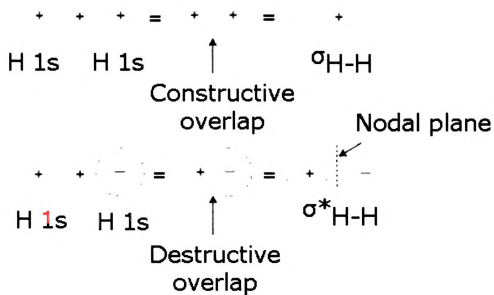


Figure A.1: Two 1s orbitals combine to form a bonding and an anti-bonding molecular orbitals.

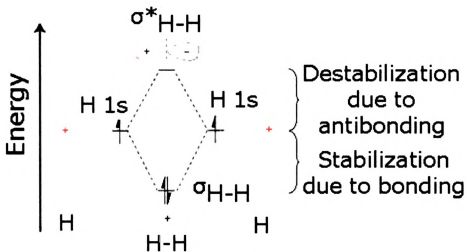


Figure A.2: An orbital correlation diagram for hydrogen. Notice that the orbitals of the separated atoms are written on either side of the diagram as horizontal lines at heights denoting their relative energies. The electrons in each atomic orbital are represented by arrows. In the middle of the diagram, the molecular orbitals of the molecule of interest are written. Dashed lines connect the parent atomic orbitals with the daughter molecular orbitals.



## A.4.2 Self Consistent Field

Hartree[88], Fock[89], and Slater[90] come up with a very distinctive idea of treating the interacting electrons as being independent of each other and introduced the idea of self consistent field(SCF). The self consistent field can be defined as the interaction field an electron experiences when the spatial average over the positions of all the other electrons are calculated. Calculations within the independent-electron approximation are often a prerequisite for those which include correlation effects. Within this approximation, the ground state wave function for  $H_2$  becomes

$$\psi_{HF}^S(\mathbf{r}_1, \mathbf{r}_2) = N_s [\phi_1(\mathbf{r}_1)\phi_1(\mathbf{r}_2) + \phi_1(\mathbf{r}_1)\phi_2(\mathbf{r}_1) + \phi_2(\mathbf{r}_1)\phi_1(\mathbf{r}_2) + \phi_2(\mathbf{r}_1)\phi_2(\mathbf{r}_2)] \chi(\sigma_1, \sigma_2) \quad (\text{A.24})$$

Different from the HL (Eqn: A.23), in the HF wave function  $\phi_1\phi_1$  and  $\phi_2\phi_2$  are called the ionic configurations. It an important fact that when two hydrogen atoms are pulled apart, the wave function does not reduce to the atomic limit. On the other hand in the HL wave function the expression does not yield the true wave function for small inter-atomic distances. The correct wave function lies between the two extremes. These two forms of basic understanding is not only valid for  $H_2$  molecule but all quantum chemical and solid state systems.

The trouble lies under SCF idea is that it would assume that an electron acted electrostatically, not only on the other electrons, but also on itself. This self-interaction term must be eliminated. The correction to the original coulomb potential is called the "exchange-correlation potential" which has to be done to get an acceptable self-consistent field. It includes both the self-interaction effects and the spin dependent exchange effects of many-electron wave functions[91].

The choice of method of setting up exchange-correlation potential is at the center of the SCF problem. The first procedure is that which Hartree used before the

Hartree-Fock method was implemented. Hartree just assumed that one should use only a potential arising from all occupied orbitals for finding an occupied spin orbital  $\phi_i$  except  $\phi_i$  itself. It is seen that for an isolated atom this method worked as well as the Hartree-Fock method since it takes care of the self-interaction problem. But it is not a good method to use for molecules and crystals.

### A.4.3 Hartree-Fock Theory

The molecular orbital approximation has provided a theoretical framework for the explanation of a wide variety of quantum mechanical phenomena. The mathematical expression of the molecular orbital model is the Hartree-Fock (HF) approximation. For closed-shell atoms and molecules the HF wave function is of the form

$$\psi_e = A(n)\phi_1(\mathbf{r}_1, \sigma_1)\phi_2(\mathbf{r}_2, \sigma_2)\dots\phi_n(\mathbf{r}_n, \sigma_n) \quad (\text{A.25})$$

in which the  $A(n)$  is the antisymmetrizer for  $n$  electrons and the  $\phi$ 's are spin and spatial orbitals, i.e. single electron wave functions, products of a spatial orbital  $\phi$  and one electron spin function  $\sigma_1=1/2$  or  $\sigma_2=-1/2$ . The spin orbitals can be denoted as

$$\chi_i = \sigma_{1,2}$$

To describe a quantum mechanical system, the Hilbert space of the wave functions and the Hamiltonian describing the kinetic and potential energy of a state have to be specified. The Hilbert space considered in the Hartree-Fock theory contains all Slater

determinants:

$$\psi_e = \frac{1}{\sqrt{n!}} \begin{vmatrix} \phi_1(1) & \phi_1(2) & \dots & \phi_1(n) \\ \phi_2(1) & \phi_2(2) & \dots & \phi_2(n) \\ \cdot & \cdot & \cdot & \cdot \\ \cdot & \cdot & \cdot & \cdot \\ \phi_n(1) & \phi_n(2) & \dots & \phi_n(n) \end{vmatrix} \quad (\text{A.26})$$

For a given geometry of a particular molecule in a closed shell state, any number of different Slater determinants may be used as approximate wave functions. However, there is only one HF determinant, namely that for which the orbitals have been varied to give the lowest possible energy of  $\int \psi_e^* H_e \psi_e d\tau$ .

By minimizing the energy resulting from the single determinant wave function in equation (A.26) one can derive a rather complicated set of Hartree-Fock equations. The essential point is that the HF wave function is the best variational wave function which can be constructed by assigning each electron to a separate orbital, or function depending only on the coordinates of the electron. The HF equations can be solved in closed form only for one-electron systems such as hydrogen atom. However, for atoms the HF equations may be solved to a rather high accuracy by numerical integration.[92]

For molecules, however, one invariably expands the orbitals  $\phi_i$  in terms of a set of analytic basis functions. Since it is never possible to use a mathematically complete set of functions in molecular calculations of a practical nature, only the approximate solutions of the HF equations are achievable. The best (lowest energy) single determinant wave function constructed within a finite basis set is “the self-consistent field” wave function. Clearly, as the size of a basis set is expanded, the SCF energy and wave function will approach the HF results.

Symmetry and equivalence restrictions are usually adopted in SCF calculations.

Each orbital is assumed to be a symmetry orbital, or more precisely, each orbital must transform according to one of the irreducible representations of the molecule's point group[93]. The solution of the HF equations including symmetry and equivalence restrictions yields the restricted Hartree-Fock (RHF) wave function.

#### A.4.4 The Energy Expression

All the orbitals in the Slater determinant (A.26) usually constructed as to be orthogonal to each other:

$$\int \phi_i(1)\phi_j(1)d\nu(1) = \delta_{ij} \quad (\text{A.27})$$

where  $d\nu(1)$  indicates space and spin coordinates integration of electron number 1. Given orbital orthogonality, an expression can be obtained for the energy (excluding the nuclear repulsion of a single determinant wave function of the form

$$\begin{aligned} E &= \int \psi_e^* H_e \psi_e d\tau \\ &= \sum_i \phi_i^*(1) \left\{ -\frac{\nabla_1^2}{2} - \sum_A \frac{Z_A}{r_{1A}} \right\} \phi_i(1) d\nu(1) \\ &+ \sum_i \sum_j \left[ \int \int \phi_i^*(1) \phi_j^*(2) \frac{1}{r_{ij}} \phi_i(1) \phi_j(2) d\nu(1) d\nu(2) \right] \\ &- \sum_i \sum_j \left[ \int \int \phi_i^*(1) \phi_j^*(2) \frac{1}{r_{ij}} \phi_j(1) \phi_i(2) d\nu(1) d\nu(2) \right] \end{aligned} \quad (\text{A.28})$$

The spin interactions in equation A.28 drop out immediately since none of the terms in the electrostatic Hamiltonian are spin dependent and

$$\begin{aligned} \int \sigma_1^*(1) \sigma_1(1) ds(1) &= \int \sigma_2^*(1) \sigma_2(1) ds(1) = 1 \\ \int \sigma_1^*(1) \sigma_2(1) ds(1) &= \int \sigma_2^*(1) \sigma_1(1) ds(1) = 0 \end{aligned} \quad (\text{A.29})$$

The first summation goes over the one-electron integrals. The next two summation terms are the electron repulsion integrals or two-electron integrals. The former are generally called Coulomb integrals while the latter are called exchange integrals. From the calculations of Cade-Huo[94], it is seen that the Coulomb integrals are significantly larger than the exchange integrals.

## A.5 Configuration Interaction Calculations

### A.5.1 Basis Sets

A basis set by definition is a collection of vectors which spans a space in which a problem is solved. In computational quantum chemistry the set of one-electron wave functions used to build molecular orbital wave functions is called the basis set. The hydrogen-like wave functions modified for electron correlation are generally not used, since they lead to mathematical complications and time-consuming calculations. Instead, wave functions are used in which the radial terms,  $\psi_r$ , are simplified. The most common such wave functions are Slater-type orbitals (STO) and Gaussian-type orbitals (GTO).

In quantum chemical calculations one would like to use the largest basis sets possible. It is important to know the accuracy of the basis set used[95]. Earlier STOs were used as basis functions due to their similarity with the eigenfunctions of the hydrogen atom as shown in Figure A.30. Their simplified general definition is

$$S = N e^{-\alpha r} \tag{A.30}$$

with N being a normalization factor,  $\alpha$  is the orbital exponent and r is the radius. STOs are mostly used to calculate the energies of diatomic molecules. They are

described by the function depending on the spherical harmonics:

$$\phi(\alpha, n, l, m; r, \theta, \phi) = Nr^{n-1}e^{-\alpha r}Y_{l,m}(\theta, \phi), \quad (\text{A.31})$$

where  $r$ ,  $\theta$ , and  $\phi$  are spherical coordinates, and  $Y_{l,m}$  is the angular momentum part. The  $n$ ,  $l$ , and  $m$  are principle, angular momentum, and magnetic quantum numbers, respectively. A simple example of STO for a hydrogen-like system takes the form of[15]:

$$STO = \left[\frac{\alpha^3}{\pi}\right]^{0.5}e^{-\alpha r}, \quad (\text{A.32})$$

Slater type orbitals have the shortcoming that most of the required integrals needed in the course of the SCF procedure must be calculated numerically which drastically decreases the speed of a computation. Therefore, a modification is introduced to the wave function by implementing Gaussian type functions, which contain the exponential  $e^{-\beta r^2}$ , instead of the  $e^{-\alpha r}$  of the STOs. Computations with Gaussian based functions are much easier than STOs. The linear combinations of such gaussian functions are used to approximate the basis functions to the atomic orbitals. A simple GTO is introduced as:

$$GTO(3G) = c_1e^{-\beta_1 r^2} + c_2e^{-\beta_2 r^2} + c_3e^{-\beta_3 r^2}, \quad (\text{A.33})$$

where 3G represents the GTO is constructed from three Gaussian type functions. The values of  $c_i$  and  $\beta_i$ , ( $i = 1, 2, 3$ ) minimizes the energy and they can be solved by different methods [15]. The main difference to the STOs is that the variable in the exponential function is squared. This leads to a vanishing slope at the center of the GTOs instead of a cusp with finite slope. A comparison between GTOs and STOs can be seen in Figure A.4 There have been some debates whether this qualitative difference leads to unexpected results but it was concluded it does not have a significant influence

on the results. GTOs are sometimes called Gaussian primitives and they constitute real orbitals called Gaussian-type functions (GTF). A Cartesian Gaussian centered on an atom “a” can be written as:

$$G_{i,j,k} = N x_a^i y_a^j z_a^k e^{-\alpha r_a^2}, \quad (\text{A.34})$$

where  $i$ ,  $j$ ,  $k$  are positive integers,  $\alpha$  is a positive orbital exponent,  $x_a$ ,  $y_a$ , and  $z_a$  are Cartesian coordinates with the origin located at a, and  $N$  is the normalization constant. When  $i + j + k = 0$ , GTF is called the s-type function; when  $i + j + k = 1$  it is called the p-type function, and if  $i + j + k = 2$  it is called the d-type function.

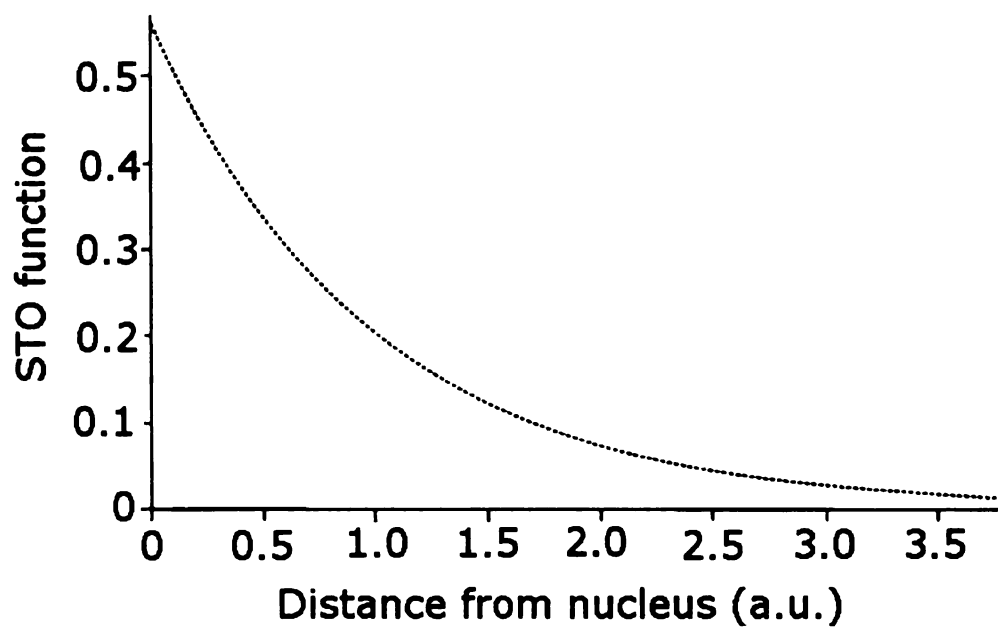


Figure A.3: Plot of the STO against the distance of the electron from the nucleus [15].



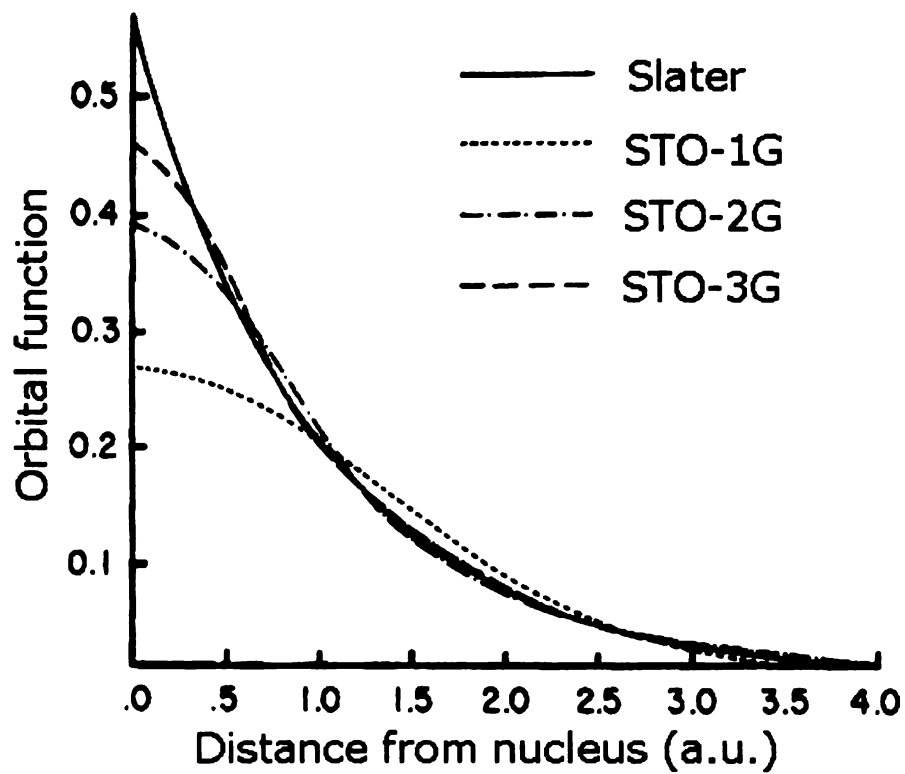


Figure A.4: Comparison of the quality of the least-squares fit of a 1s Slater function obtained at the STO-1G, STO-2G, and STO-3G levels[16].

## A.6 Donor molecule picture

Consider an electronic system (molecule or atom) represented by a model in which the nuclei are replaced by fixed electric charges (Born–Oppenheimer model). With the corresponding Schrödinger equation (Eq.A.1), the independent electron model gives

$$H_e \Psi = E_0 \Psi \quad (\text{A.35})$$

Products of atomic or molecular orbitals are solutions of equation A.35 and Slater determinants must be introduced to take account of the spin and Pauli principle. A given choice of orbitals is called a configuration and the various convenient linear combinations of Slater determinants produced by such a choice give approximations of wave functions associated with molecular or atomic states 'belonging to the considered configuration'.

The atomic or molecular orbitals could be improved and there are ways to do so. However, even when using the best orbitals a small gap remains between the calculated energy and the experimental one. The Hartree-Fock (HF) method describes the optimal Slater determinant representation of a molecular wave function and their computationally feasible solution via the SCF method. Slater determinant representations have the advantage that they satisfy the antisymmetry principle and account for the indistinguishability of individual electrons; however, they do not correlate the motions of electrons with opposite spins, i. e. there exists a nonzero probability of two electrons with opposite spins occupying the exact same point in space. Moreover, the Fock operator, which defines an optimal spin orbital by treating the electron within that orbital as if it were moving in the average field of the other electrons, does not correlate the motions of electrons too. For these reasons, HF or SCF wave functions are said to be uncorrelated and the HF model is described as a "one-electron" or "independent particle" model. Because in reality electrostatic forces prevent electrons

from occupying an identical point in space, the exact non-relativistic energy must be lower than the variationally determined HF limit energy. The difference between the HF limit energy,  $E_{HF}$ , and the exact non-relativistic energy,  $E_{exact}$ , is defined to be the “correlation energy”,  $E_{corr}$  :

$$E_{corr} = E_{exact} - E_{HF} \quad (\text{A.36})$$

The correlation energy is practically of the order of 1 per cent. Although this gap is small from the total energy point of view it has an important effect on the calculation of properties like atomization and isomerization energies. In some cases, the self-consistent field approximation leads to wrong results, even for qualitative predictions. For  $F_2$ , Wahl’s extended basis calculations showed the Hartree-Fock energy of  $F_2$  to be more than 1 eV above the energy of two F atoms, leading to the wrong conclusion that the  $F_2$  molecule is unstable. More generally a gap can introduce a significant error in the calculation of all non-stationary properties because even if the approximate wave function is satisfactory from the energetic point of view it must be far from the exact wave function in the Hilbert space.

A new improvement is needed. Many different ways have been explored, one being to assume that the infinite set of products of orbitals which satisfy equation A.35 forms a basis in the Hilbert space. A simple choice was to take a Slater determinant of orbitals, and this gave us the Hartree-Fock equations. The exact ground state energy and exact ground-state wave function can be obtained including electron correlation effects by minimizing the energy with respect to all normalized, antisymmetric, wave functions. In practice it is not possible to introduce an infinite set of configurations. Thus, the basis functions are truncated and therefore only approximate wave functions can be reached. Since several Slater determinants are very close together in energy and describing the system with a single Slater determinant will be a poor approximation,

a method is used to improve the molecular-orbital approximation to write the wave function as a sum of several Slater determinants. This is the “configuration interaction (CI) method” [96].  $\Psi$  can be expanded in terms of such products as

$$\Psi_i = \sum_{j=1}^{\infty} C_{ij} \Phi_i \quad (\text{A.37})$$

If the spin is taken into account the exact wave function including the spin will be expanded in terms of linear combinations of Slater determinants.

I have introduced the results of configuration interaction calculations for two-donor molecules with the tip potential in Chapter 4. Figure A.5 shows the flow chart summarizing CI calculations for our system done by James Harrison in Chemistry Department at Michigan State University . Calculations start with the correct choice of the basis functions. Prof. Harrison used the augmented Dunny basis functions given as:

$$e^{-\alpha r} = c \int f(rx) e^{-rx^2} dx, \quad (\text{A.38})$$

where easily evaluated Gaussian-type function in the integrand is approximated to the Slater-type atomic orbitals. The Hamiltonian for our system includes the kinetic energy expression, electron-electron interaction, the nuclear interaction, and the effective potential applied by the tip:

$$\hat{H} = -\frac{1}{2}\nabla_1^2 - \frac{1}{2}\nabla_2^2 + \sum_{i>j} \frac{1}{r_{ij}} + \sum_{k=1}^2 \frac{Z_k}{|\mathbf{r}_i - \mathbf{r}_k|} - \sum \phi(\mathbf{r}_i)e, \quad (\text{A.39})$$

where  $Z$  is the nuclear charge and  $e$  is electron charge, and  $\phi$  stands for the electric potential due to an approximated image charge for the tip. Then CI wave function is generated from the molecular orbitals, which are calculated from the augmented basis functions using HF-SCF approximation. CI wave function can be represented

through the linear combinations of molecular orbitals:

$$|\psi\rangle = \sum_i \sum_j c_{ij} A \phi_i \phi_j, \quad (\text{A.40})$$

where  $\phi_i$  and  $\phi_j$  are molecular orbitals,  $c_{ij}$  are the coefficients of the molecular orbitals, and  $A$  is the normalization constant. Finally, the Schrodinger equation is solved for the energies of possible bound states of our system, which will be presented in Chapter 4.

### Flow chart for CI calculations

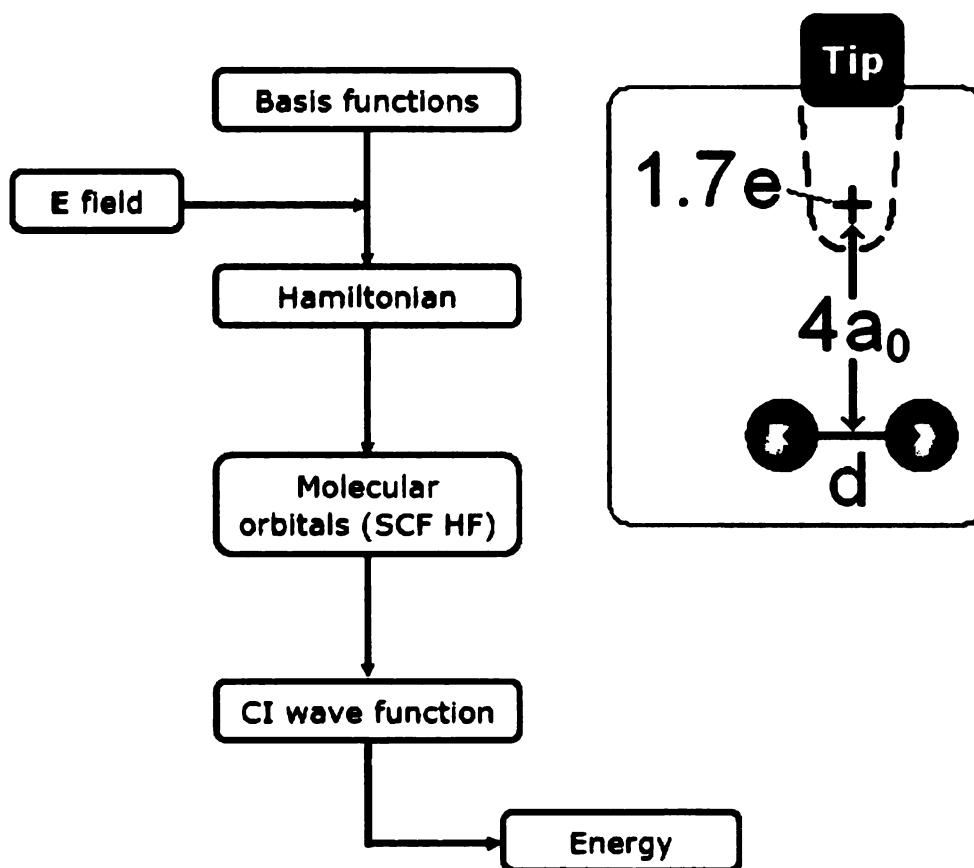


Figure A.5: (Left) The summarized ingredients of configuration interaction method. Calculations start with correct choice of basis functions and determining the relevant Hamiltonian for the system. Self consistent field (SCF) Hartee-Fock molecular orbitals must be generated to solve for the energy of the system for CI wave functions. (Right) The schematic diagram representing donor atoms constituting donor molecule and tip approximated as a point charge.

# Appendix B: Gate Fabrication

In this appendix, I will introduce the surface gate fabrication process on our GaAs sample. Here I present the technical issues and recipes. Since the certain parameters and conditions fluctuate for each fabrication attempt, one must operate on a couple of dummy samples for calibration. I will explain the process under these main titles: Sample cleaning, resist covering, electron-beam lithography, and developing, evaporation and lift-off. Each step of the fabrication is processed in the Keck microfabrication facility.

## B.1 Sample cleaning

1. Customized sample cutting: Before cleaning we cut the sample from the wafer. The dimensions are about 0.5 cm by 0.5cm. Care must be taken not to scratch the sample surface. We used glass slides and a very sharp scribe to cleave the sample. Place the glass slide on the sample and draw a line along the guiding edge of the glass slide by the scribe. Then cleave the sample along the scratched line by applying force over the sample with the handle of the scribe.
2. Place the sample into a beaker half filled with acetone. Cover the bottom of the beaker with a filter paper to prevent the sample bumping on the walls of the beaker. GaAs sample is very brittle and there is a high chance either to crack or get the surface scratched.
3. Put the beaker in ultrasound machine and clean it 10 minutes. Use cotton tip for removing any visible dirt residues.
4. Prepare two other beakers half filled with isopropyl alcohol (IPA) and deionized (DI) water. Take the sample out of the acetone beaker carefully with tweezers

holding away from the center. Insert sample before acetone gets dried into the IPA. Shake the sample inside the IPA about 1 minute. Next, insert it into the DI water and rinse it about 1 minute. Then blow dry with N<sub>2</sub>.

5. Note: There should not be any visible residue of contaminants on the sample surface after cleaning.

## **B.2 Bilayer resist covering**

1. Note: We need to cover the sample with the resist immediately after cleaning the surface.
2. Prepare the spin chamber by covering the tray with aluminum foil and cleaning the spinning top in acetone and IPA. Replace the spinning top on the spinning axis.
3. Adjust spin rate to 5600 RPM and test it.
4. Replace the sample over the vacuum holder.
5. Blow dry with N<sub>2</sub> during the sample is spinning on the vacuum holder.
6. Pour one drop of 950K PMMA/MMA 9% at the center of the sample with a clean piped. Spin resist 50 seconds.
7. Bake the sample on the hot plate at 170 C for 1/2 hour.
8. After cooling the sample down to room temperature take it from the oven and put it back on the vacuum holder.
9. Blow dry with N<sub>2</sub> again. Drop 4% 950K PMMA/MMA at the center of the sample. Spin it 50 sec at 5000 RPM.
10. Bake it again at 150 C for 1 hour in the oven.



## B.3 E-beam writing — JEOL JSM 840A Scanning Electron Microscope

### B.3.1 Key parameters

The e-beam writing process is performed in a JEOL JSM 840A scanning electron microscope. I used the following key parameter to get the best quality surface gates:

1. *Accelerating voltage*: 35 keV. Higher acceleration voltage reduces the extra exposure due to the backscattering of the electrons.
2. *Probe current*: (16-20) pA. Smaller probe current increases the resolution. Probe current stabilizes in about 45 minutes
3. *Aperture setting*: 4. We use the smallest aperture setting to get small probe current.
4. *Working Distance*: 15 mm. Resolution increases as the working distance gets smaller.
5. *Magnification*: 400. The correct magnification must be entered to the software program editor from where the computer gets the patterns to be written.
6. *Chamber pressure during writing*:  $9 \times 10^{-6}$  Torr.
7. *Mode*: SEM1
8. *Area dose*:  $280 \mu\text{C}/\text{cm}^2$  for lines,  $268 \mu\text{C}/\text{cm}^2$  for circles.
9. *Center to center distance*: 206 Å

### B.3.2 Alignment and pattern writing

Before writing, the microscope beam must be properly aligned, focused, corrected for astigmatism, etc. This is performed first on a hole on the stage holding the sample. Then, we focus on smaller features on the sample holder that can easily be used for focusing at a magnification of 300000, the maximum magnification of the SEM. These processes must be done as fast as possible since the sample should be saved from exposure to the beam current.

1. Attach the sample to the sample holder with the clips from the sides.
2. Align the stage:  $X = 25.0$ ,  $Y = 25.0$ ,  $Z_{coarse} = 39$ ,  $tilt = 0$ ,  $rotation = 0$ ,  $Z_{fine}$  is counterclockwise all the way.
3. Insert and mount the sample in the SEM main chamber and remove the rod. Pump out the vacuum lock.
4. Turn the “detector ” DOWN (SEI) and “collector” UP.
5. Switch the scan mode to LSP.
6. Adjust the brightness to see the line.
7. *Saturation*: Turn on the filament current slowly till the line broadens once and narrows a little and stays there. That is the filament current setting. Note it in the log book.
8. Set scan mode to PIC. Set *emission reading*: 80, *filament current*: 225 mA, *probe current*: 16-20 pA.
9. Take faraday cage below the beam, turn on white switch to the left and measure beam current if necessary.
10. Set brightness to zero.

11. Align the stage to the writing position, blank off the beam to EXT first , change to desired magnification (400) and change EXT SCAN to “ON”
12. After writing the pattern move the stage manually to change the sample position for the subsequent writing.
13. After finishing whole pattern writing pull stage back to initial position.
14. Turn the filament off slowly (a few seconds).
15. Acceleration voltage OFF.
16. Set to the maximum magnification (300000).
17. Beam blanker OFF.
18. Take the sample out

## **B.4 Developing, TiAu deposition, and lift-off**

1. *Developer*: MIBK:IPA = 1:3. Soak sample after E-beam writing into the developer for 70 seconds.
2. *Stopper*: Soak in and shake the sample in the IPA for 30 seconds.
3. Rinse with DI water for 20 seconds.
4. *Metal Deposition*: Deposit  $\approx 30 \text{ \AA}$  Ti wetting layer and  $\approx 250 \text{ \AA}$  Au in the thermal evaporator performing under standard conditions.
5. *Lift-off*: Soak in warm acetone ( $\approx 80 \text{ C}$ ) about 10 minutes. If necessary apply 2-3 second ultrasound shaking.

## B.5 Four-pattern procedure

Here, I will introduce the specific technical tips about the e-beam writing procedure of our “4pattern” mesh, which is a CAD generated file stored under “NPGS /Projects/Cemil/4pattern.DC2”. It is also saved under the directory “endeavor/users /CMP Tessmer/Kayis/NPGS”. Our procedure to fabricate the 4pattern mesh can be summarized as the following: The 1mm by 1mm full pattern is made of overlapping segments of 200  $\mu\text{m}$  by 200  $\mu\text{m}$  mesh, which consists of circles and line shapes. The circles have the diameters of 0.5  $\mu\text{m}$ , 1  $\mu\text{m}$ , 1.5  $\mu\text{m}$ , and 2  $\mu\text{m}$ . The CAD generated “4pattern” file is written 25 times on a 5 by 5 matrix consecutively. Each run takes about seven minutes and whole procedure takes about two and a half hours. It is a challenge to keep the beam current stable since the procedure takes longer time span. Moreover, the dimensions of the whole pattern is macroscopically large. Hence, it is very important to achieve precise beam current parameters by aligning the SEM and adjusting the parameters such as astigmatism. The positions of the consecutive patterns is determined by moving the sample manually using the external  $x$ - $y$  control settings of the stage. For JEOL JSM-840A the smallest increment is 2 $\mu\text{m}$ , which allows a quite good alignment comparing with the 4pattern dimensions. I moved the sample about 190  $\mu\text{m}$ , which is approximately 10  $\mu\text{m}$  less than the mesh length. This results in the two consecutive patterns to overlap, which makes the full pattern electrically in contact (see Figure B.1).

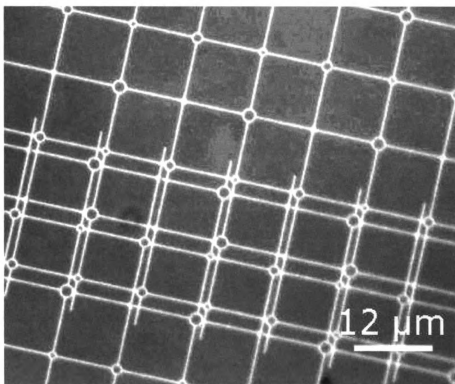


Figure B.1: An image of the “4pattern” fabricated on the surface of the sample taken by an optical microscope. The overlap of the edges is seen in the figure.

## Bibliography

- [1] F. J. Ruess et al. Realization of atomically controlled dopant devices in silicon. *Small*, 3:563, 2007.
- [2] S. E. S. Andresen et al. Charge state control and relaxation in an atomically doped silicon device. *Nanoletters*, 7:2000, 2007.
- [3] J. M. Luttinger W. Kohn. Theory of donor states in silicon. *Phys. Rev.*, 98:915–922, 1955.
- [4] E. H. Lieb. Bound on the maximum negative ionization of atoms and molecules. *Phys. Rev. A*, 29:3018–3028, 1984.
- [5] E. F. Schubert. *Doping III-V Semiconductors*. Cambridge, UK.
- [6] G. A. Steele. *Imaging Transport Resonances in the Quantum Hall Effect*. PhD thesis, MIT, 2006.
- [7] E. F. Schubert. *Delta-doping of Semiconductors*. Cambridge, UK.
- [8] T. Mimura. *HEMT and LSI application in Semiconductor and Semimetals, Chapter 4*, volume 30.
- [9] M. A. Erickson et al. Cryogenic scanning probe characterization of semiconductor nanostructures. *Appl. Phys. Lett.*, 69:671–673, 1996.
- [10] I. J. Maasilta S.H. Tessmer I. Kuljanishvili, S. Chakraborty. Modeling electric field sensitive scanning probe measurements for a tip of arbitrary shape. *Ultra-microscopy*, 102:7–12, 2004.
- [11] I. Kuljanishvili. *Scanning Probe Study Of A Two-Dimensional Electron System And Donor Layer Charging In Heterostructured Semiconductors*. PhD thesis, Michigan State University, 2005.
- [12] A. K. Geim et al. Resonant tunneling through donor molecules. *Phys. Rev. B*, 50:8074–8077, 1994.
- [13] H. Lüth H. Ibach. *Solid-State Physics*. Springer, Berlin, 2003.
- [14] R. Gomer. *Field Emission and Field Ionization*.
- [15] K. Namboori K. I. Ramachandran, G. Deepa. *Computational Chemistry and Molecular Modeling*. Springer, Berlin, 2008.
- [16] N. S. Ostlund A. Zsabo. *Modern Quantum Chemistry-Introduction to Advanced Electronic Structure Theory*. McGraw-Hill, Inc., New York, 1989.
- [17] H. Sellier et al. Transport spectroscopy of a single dopant in a gated silicon nanowire. *Phys. Rev. Lett.*, 97:206805, 2006.

- [18] G. P. Lansbergen. Quantum confinement and symmetry transition of a single gated donor electron in silicon. *Nature Physics*, 4:656 – 661, 2008.
- [19] B. E. Kane. A silicon-based nuclear spin quantum computer. *Nature*, 393:133, 1998.
- [20] M.I. Dykman B. Golding. Acceptor-based silicon quantum computing. *cond-mat*, cond-mat/0309147, 2003.
- [21] M. A. Reed R. G. Wheeler R. J. Matyi M. R. Deshpande, J.W. Sleight. Spin splitting of single 0d impurity states in semiconductor heterostructure quantum wells. *Phys. Rev. Lett.*, 76:13281331, 1996.
- [22] A. V. Kuznetsov F. T. Vas'ko. *Electronic States and Optical Transitions in Semiconductor Heterostructures*. Berlin.
- [23] John H. Davies. *The physics of low-dimensional semiconductors: an introduction*. Cambridge, UK.
- [24] Zh. I. Alferov. *Semiconductor Heterostructures: Physical Processes and Applications*. Moscow, Russia.
- [25] G. Biasiol et. al. Deep levels in mbe grown algaas/gaas heterostructures. *Microelectronic Engineering*, 73-74:954959, 2004.
- [26] K. Ploog L. L. Chang. *Molecular Beam Epitaxy and Heterostructures*. Dordrecht, Netherlands.
- [27] B. A. Lombos. Deep levels in semiconductors. *Can. J. Chem.*, 63:1666, 1985.
- [28] J. R. Arthur A. Y. Cho. Molecular beam epitaxy. *Prog. Solid State. Chem.*, 10:157–191, 1975.
- [29] F. Rinaldi. Basics of molecular beam epitaxy (mbe). Annual, Optoelectronics Department, University of Ulm, 2002.
- [30] L. C. L. Hollenberg et al. Charge-based quantum computing using single donors in semiconductors. *Phys. Rev. B*, 69:113301, 2004.
- [31] R. Vrijen et al. Electron-spin-resonance transistors for quantum computing in silicon-germanium heterostructures. *Phys. Rev A.*, 62:012306, 2000.
- [32] A. Kingon P. M. Vilarinho, Y. Rosenwaks. *Scanning Probe Microscopy: Characterization, Nanofabrication and Device Applications of Funtional Materials*. Berlin.
- [33] T. A. Fulton L. N. Pfeiffer K. W. West A. Yakoby, H. F. Hess. Electrical imaging of the quantum hall state. *Solid State Commun.*, 111:1–13, 1999.

- [34] M. J. Yoo et al. Scanning single-electron transistor microscopy: Imaging individual charges. *Science*, 276:579, 1997.
- [35] T. Kramer. E. J. Heller R. M. Westervelt M. P. Hanson A. C. Gossard K. E. Aidala, R. E. Parrot. Imaging magnetic focusing of coherent electron waves. *Nature Physics*, 3:464, 2007.
- [36] M. A. Topinka et al. Coherent branched flow in a two-dimensional electron gas. *Nature*, 410:183, 2001.
- [37] R.C. Ashoori L. S. Levitov M. R. Melloch S. H. Tessmer, P. I. Glicofridis. Sub-surface charge accumulation imaging of a quantum hall liquid. *Nature*, 392:51, 1998.
- [38] R. C. Ashoori M. Shayegan G. Finkelstein, P. I. Glicofridis. Quantum hall liquid using a few-electron bubble. *Science*, 289:90, 2000.
- [39] G. Binnig et al. Tunneling through a controllable vacuum gap. *Appl. Phys. Lett.*, 40:178, 1982.
- [40] G. Binnig et al. In touch with atoms. *Rev. Mod. Phys.*, 71:S234, 1999.
- [41] D. M. Eigler H. C. Manoharan, C. P. Lutz. Quantum mirages formed by coherent projection of electronic structure. *Nature*, 403:512–515, 2000.
- [42] K. Besocke. An easily operable scanning tunneling microscope. *Surf. Sci.*, 181:145, 1987.
- [43] S. Chakraborty I. Moraru S. H. Tessmer S. Urazhdin, I. J. Maasilta. High scan area cryogenic scanning probe microscope. *Rev. Sci. Instrum.*, 71:4170, 2000.
- [44] K. Besocke J. Frohn, J. F. Wolf and M. Teske. Coarse tip distance adjustment and positioner for a scanning tunneling microscope. *Rev. Sci. Instrum.*, 60:1200, 1989.
- [45] R. Mosvovich. *Experimental techniques in condensed matter physics at low temperature*, chapter 3.3. Addison-Wesley, New York, 1988.
- [46] S. Chakraborty. *Charge Accumulation Imaging of a Two-dimensional Electron System*. PhD thesis, Michigan State University, 2003.
- [47] R. C. Ashoori. *The Density of States in the Two-Dimensional Electron Gas and Quantum Dots*. PhD thesis, Cornell University, 1991.
- [48] M. Brodsky. *Charging of Small Two-Dimensional Electron Puddles*. PhD thesis, MIT, 2000.
- [49] P. I. Glicofridis. *Subsurface Charge Accumulation Imaging of the Quantum Hall Liquid*. PhD thesis, MIT, 2001.



- [50] R. C. Ashoori S. Urazhdin, S. H. Tessmer. A simple low-dissipation amplifier for cryogenic scanning tunneling microscopy. *Rev. Sci. Instrum.*, 73:310, 2002.
- [51] J.F. Harrison C. Piermarocchi T. A. Kaplan S. H. Tessmer L.N. Pfeiffer I. Kuljanishvili, C. Kayis and K.W. West. Scanning-probe spectroscopy of semiconductor donor molecules. *Nature Physics*, 4:227, 2008.
- [52] W. Kohn J. M. Luttinger. Motion of electrons and holes in perturbed periodic fields. *Phys. Rev.*, 98:869–883, 1954.
- [53] T. A. Kaplan. The chemical potential. *J. Stat. Phys.*, 122:1237, 2006.
- [54] R. C. Ashoori. Electrons in artificial atoms. *Nature*, 379:413–419, 1996.
- [55] I. Kuljanishvili S. H. Tessmer. Preprint. *arXiv:0806.1899*, 2008.
- [56] L.N. Pfeiffer K.W. West J. Hampton, J.P. Eisenstein. Capacitance of two-dimensional electron systems subject to an in-plane magnetic field. *Solid State Commun.*, 94:559–562, 1996.
- [57] D. R. Lide. *CRC Handbook of Chemistry and Physics, 86th ed.* Taylor and Francis, Boca Raton, 2006.
- [58] R. C. Ashoori et al. Single-electron capacitance spectroscopy of discrete quantum levels. *Phys. Rev. Lett.*, 68:3088–3091, 1992.
- [59] K.H. Gulden C. Metzner G.H. Dohler T. Schmidt, St.G. Muller. In-plane transport properties of heavily d-doped GaAs n-i-p-i superlattices: Metal-insulator transition, weak and strong localization. *Phys. Rev. B*, 54:13980, 1996.
- [60] R. F. Wallis M. Balkansky. *Semiconductor Physics and Applications.* Oxford University Press, 2000.
- [61] N. H. March W. Jones. *Theoretical Solid State Physics*, volume 2. Dover Publishing, 1985.
- [62] M. Shur M. Levinstein, S. Rumyantsev. *Handbook Series on Semiconductor Parameters, vol. 2.* World Scientific, London, 1999.
- [63] G. Gowan S. Brandt. *Data Analysis: Statistical and Computational Methods for Scientists and Engineers.* Springer, New York, 1999.
- [64] R.H. Good E.L. Murphy. Thermionic emission, field emission, and the transition region. *Phys. Rev.*, 102:1464–1473, 1956.
- [65] R. L. Park. *Solid State Physics: Surfaces (Experimental Methods in the Physical Sciences).* Academic Press, Burlington, MA, 1985.
- [66] J. R. Janesick. *Scientific Charge-coupled Devices.* SPIE Publications, Bellingham WA, 2001.

- [67] E. Wigner. On the constant  $a$  in richardson's equation. *Phys. Rev.*, 49:696, 1936.
- [68] R. Baierlein. *Thermal Physics*.
- [69] L. W. Nordheim R. H. Fowler. The effect of the image force on the emission and reflection of electrons by metals. *Proc. Roy. Soc. (London)*, A119:173, 1928.
- [70] L. W. Nordheim. *Proc. Roy. Soc. (London)*, A121:626, 1928.
- [71] L. Roubi R. Maimouni Y. Khlifi, K. Kassmi. Modeling of fowler-nordheim current of metal/ ultra-thin oxide/ semiconductor structures. *M.J. Condensed Matter*, 3:53, 2000.
- [72] E. L. Wolf. *Principles of Electron Tunneling Spectroscopy*. New York.
- [73] L. N. Pfeiffer K. W. West G. A. Steele, R. C. Ashoori. Imaging transport resonances in the quantum hall effect. *Phys. Rev. Lett.*, 95:136804, 2005.
- [74] L. I. Glazman D. B. Chklovskii, B. I. Shklovskii. Electrostatics of edge channels. *Phys. Rev. B*, 46:4026.
- [75] H. F. Shaeffer. *The Electronic Structure of Atoms and Molecules*. Massachusetts, USA.
- [76] E. Scrdinger. *Ann. Physik*, 79:361 489, 1926.
- [77] F. L. Pilar. *Elementary Quantum Chemistry*. New York, USA.
- [78] J. R. Oppenheimer M. Born. *Ann. Physik*, 84:457, 1927.
- [79] D. Rapp. *Quantum Mechanics*. New York.
- [80] L. Pauling L. C. Pauling. *The nature of the Chemical Bond*. Cornell University Press, New York, 1989.
- [81] T. Shida. *The Chemical Bond: A Fundamental Quantum Mechanical Picture*. Springer, Berlin, 2004.
- [82] F. London W. Heitler. *Z. Phys.*, 44:455, 1927.
- [83] T. C. Lubensky P. M. Chaikin. *Principles of Condensed Matter Physics*. Cambridge University Press, 2000.
- [84] F. Hund. *Z. Phys.*, 51:759, 1928.
- [85] R. S. Mulliken. *Phys. Rev.*, 32:186, 1928.
- [86] <http://www.sparknotes.com/chemistry/bonding/molecularorbital/section1.html>.
- [87] P. Fulde. *Electron Correlations in Molecules and Solids*. Berlin, Germany.
- [88] D. R. Hartree. *Proc. Cambridge Philos. Soc.*, 24:89, 1928.

- [89] V. Fock. *Z. Phys.*, 61:126, 1930.
- [90] J. C. Slater. *Phys. Rev.*, 35:210, 1930.
- [91] J. C. Slater. *The Self-consistent Field of Molecules and Solids*, volume 4. McGraw-Hill, Inc., New York, 1974.
- [92] D. R. Hartree. *The Calculation of Atomic Structures*. New York.
- [93] F. A. Cotton. *Chemical Applications of Group Theory*. New York.
- [94] W. M. Huo P. E. Cade. *J. Chem. Phys.*, 47:614–649, 1967.
- [95] E. J. Baerends E. van Lenthe. Optimized slater-type basis sets for the elements 1118. *Journal of Computational Chemistry*, 24:1142–1156, 2002.
- [96] D. Peeters M. Sana R. Daudel, G. Leroy. *Quantum Chemistry*. New York, USA.